X-RAY SPECTROSCOPIES IN THE TIME DOMAIN: IMPLEMENTATION FOR ULTRAFAST STUDIES

Dissertation
zur Erlangung des Doktorgrades
an der Fakultät für Mathematik, Informatik und Naturwissenschaften
Fachbereich Physik
der Universität Hamburg

vorgelegt von
Manuel Harder

Hamburg
2023

Gutachter der Dissertation:	Prof. Dr. Christian Bressler Prof. Dr. Nils Huse
Zusammensetzung der Prüfungskommission:	Prof. Dr. Christian Bressler Prof. Dr. Nils Huse Prof. Dr. Michael Potthoff PD Dr. Michael Martins Dr. Georg Spiekermann
Vorsitzender der Prüfungskommission:	Prof. Dr. Michael Potthoff
Datum der Disputation:	19.01.2024
Vorsitzender Fach-Promotionsausschuss PHYSIK:	Prof. Dr. Günter H. W. Sigl
Leiter des Fachbereichs PHYSIK:	Prof. Dr. Wolfgang J. Parak
Dekan der Fakultät MIN:	Prof. Dr.-Ing. Norbert Ritter

Abstract

A dispersive multi-crystal hard X-ray spectrometer operated in the von Hámos geometry was designed for the hard X-ray spectroscopy end station (FXE[1]) at the European XFEL[2]. Encountering challenges like the varying pulse intensity, beam position and photon energy of each shot at X-ray free electron lasers highly increased the interest in energy-dispersive secondary X-ray spectrometers. In this thesis, we present the theory behind the von Hámos geometry for single and multiple crystals. The commissioning and first experiments, during which we tested the spectrometer's capabilities for a broad set of X-ray spectroscopy techniques at different synchrotron radiation facilities are presented. In particular, we present a study in which we utilized the spectrometer to track the coordination and bond lengths in amorphous GeO_2. This was achieved by recording the Germanium valence-to-core (vtc) emission lines, during a transition from four- to six-fold coordination, thus establishing vtc-spectroscopy as a probe for coordination number and bond length. This novel approach is highly desired for time-resolved measurements on dilute samples running in liquid jet systems, where other methods like X-ray diffuse scattering and extended X-ray absorption fine structure (EXAFS) are more challenging to perform. Moreover, this method extends the limited capabilities of X-ray diffraction for multi-compound systems. Furthermore, we implemented a high repetition rate multi-photon data acquisition system at beamline P01 to track the photoinduced changes via X-ray absorption near-edge structure (XANES), enabling us to track the picosecond time-resolved dynamics of two weakly absorbing cobalt complexes, $[Co(III)(CN)_6]^{3-}$ and $[Co(III)(en)_3]^{3+}$. As a result, we were able to confirm the $^5T_2$ state as lowest-lying excited state of $[Co(III)(en)_3]^{3+}$ following optical excitation. With the calculated excited state fraction, we reconstructed the XANES spectra for the lowest-lying excited state of both compounds.

[1] Femtosecond X-ray Experiment
[2] European X-Ray Free-Electron Laser Facility GmbH

Zusammenfassung

Für die Endstation für harte Röntgenspektroskopie (FXE) am European XFEL wurde ein in der von Hámos-Geometrie betriebenes dispersives Multikristall-Spektrometer für harte Röntgenstrahlung entwickelt. Durch Herausforderungen wie die unterschiedlichen Pulsintensität, Strahlposition und Photonenenergie jedes Schusses, wie sie bei Röntgen-Freie-Elektronen-Lasern auftreten, haben die Notwendigkeit für energiedispersive, sekundäre Röntgenspektrometer stark erhöht. In dieser Arbeit stellen wir die Theorie hinter der von Hámos-Geometrie für Ein- und Mehrfachkristallspektrometer vor. Wir präsentieren die Ergebnisse der Inbetriebnahme und die ersten Experimente, bei denen wir die Fähigkeiten des Spektrometers für eine Vielzahl von Röntgenspektroskopietechniken an verschiedenen Synchrotronstrahlungsanlagen getestet haben. Hervorheben möhten wir dabei wir eine Studie, in der wir das Spektrometer zur Messung der Koordinations- und Bindungslängen in amorphem GeO_2 eingesetzt haben. Dies wurde durch die Aufzeichnung der Germanium Valenz-zu-Kern-Emissionslinien (vtc) während eines Übergangs von vier- zu sechsfacher Koordination erreicht, wodurch die vtc-Spektroskopie als Messmethode für Koordinationszahl und Bindungslänge etabliert wurde. Dieser neuartige Ansatz ist vielversprechend für zeitaufgelöste Messungen an verdünnten Proben in Flüssigkeitsstrahlsystemen, da die Standardmethoden wie z.B. diffuse Röntgenstreuung und EXAFS (erweiterte Röntgenabsorptionsfeinstruktur) an diesen Proben schwierig durchzuführen sind. Darüber hinaus erweitert diese Methode die begrenzten Möglichkeiten der Röntgenbeugung für amorphe Mehrkomponentensysteme.

Zusätzlich haben wir am Messplatz P01 ein Multi-Photonen-Datenerfassungssystem mit hoher Messrate implementiert, um photoinduzierte Veränderungen in Komplexen mittels XANES (Nahkanten-Röntgenabsorptionsspetroskopie) zu messen. Dies ermöglichte uns die zeitaufgelöste Dynamik von zwei schwach absorbierenden Kobaltkomplexen ($[Co(III)(CN)_6]^{3-}$ und $[Co(III)(en)_3]^{3+}$) im Pikosekundenbereich verfolgen. Dadurch konnten wir den $^5T_2$-Zustand als den am niedrigsten liegenden angeregten Zustand nach optischer Anregung von $[Co(III)(en)_3]^{3+}$ bestätigen. Mit der berechneten Anteil der angeregten Zustände war es uns möglich, die XANES-Spektren für die am niedrigsten liegenden angeregten Zustände beider Verbindungen zu rekonstruieren.

Contents

1 Introduction

Since their discovery in 1895 by Wilhelm Conrad Röntgen, X-rays played an important role enabling and improving our modern life[90]. The Nobel prize for physics, chemistry and physiology or medicine in each category has been awarded more than ten times for research based on X-radiation. This demonstrates how important and versatile X-rays are in science. Over the time, X-ray sources evolved from simple X-ray tubes to large research facilities dedicated to produce X-radiation with high brilliance, coherence and short pulse durations. For example, PETRA III[3] is a third generation storage ring, located in Hamburg, Germany, that started its operation in 2009. Yet, to take on the challenges of modern science, there is a growing demand for even better X-ray sources with higher photon flux as well as temporal resolution. For this purpose the European XFEL was built and started operation in 2017. The European XFEL is a fourth generation X-ray source, with a photon flux of up to 10^{16} photons and potentially sub-femtosecond time resolution[98].

As the sources get more and more sophisticated, the quantity of X-ray measurement techniques and their capabilities increase and we still find new physical properties that can be measured with X-rays. X-ray spectroscopies are a set of techniques that measure the amount of photons interacting with a sample in dependence of the photon energy. As each element has its own characteristic electron binding energies, most X-ray spectroscopic techniques are element-specific. E.g. in contrast to techniques like common X-ray diffraction, the local environment around selected elements can be measured. In chapter 2 we describe the theoretical basics of the X-ray spectroscopies used in the scope of this thesis. To record an X-ray spectrum, the energies of the photons in an experiment have to be measured at least once. A device that measures the energy of photons emitted or scattered by the sample is called X-ray spectrometer. A typical hard X-ray spectrometer consists of analyzer crystals to measure the photon energy and a detector to record the number of photons. Science at XFELs is relatively young and fast developing field, many researchers work on implementing and improving the known X-ray techniques at these synchrotron radiation sources. The highly intense photon bunches at XFELs come with the challenge of unstable photon beam characteristics, like energetic and spatial shifts as well as radiation damage induced by the high fluence. Therefore, for the FXE scientific instrument, an endstation dedicated to hard X-ray spectroscopy and scattering at European XFEL, a multi crystal energy-dispersive spectrometer in von Hámos geometry has been designed and manufactured by JJ X-ray[4]. A Beckhoff[5] control for the motors has been assembled to operate the spectrometer, which was commissioned at different syn-

[3] Positron-Elektron-Tandem-Ring-Anlage, an upgrade of PETRA II, a collider used for particle physics
[4] https://www.jjxray.dk/
[5] https://www.beckhoff.com/

chrotron beamlines, namely P01 at PETRA III, BL09 at DELTA[6] and 7ID-D at APS[7], which are described in chapter 3. As part of the commissioning we tested the setup for a broad range of different X-ray spectroscopy techniques, such as HERFD or PFY XAS, XES XRS and RXES (see chapter 2 for an explanation of each acronym). In addition we recorded time-resolved XES spectra, for example the first picosecond time-resolved valence-to-core emission spectrum of an iron compound. A detailed introduction to von Hámos spectrometers in general, and the commissioning of FXE's von Hámos spectrometer in particular is given in chapter 4. During the first experiments using the von Hámos spectrometer, we could show that XES vtc spectra are sensitive to changes in coordination and bond length, these findings are presented in chapter 5. While the von Hámos can be employed to perform different spectroscopic techniques, its general purpose is mainly to conduct X-ray emission measurements.
To complement this technique, a digitizer has been installed at P01 to increase the efficiency of time resolved X-ray absorption measurements up to three orders of magnitude compared to single photon counting setups and enabling shot-to-shot normalization[29]. By doing so, we were able to record the spectra of weakly absorbing cobalt complexes, which are of interest in catalysis, yet still need a better understanding to simultaneously act as catalyst and photosensitizer. These measurements are presented in chapter 6. We will summarize our results and discuss possible applications for future research in chapter 7.

[6] Dortmunder ELekTronenspeicherring-Anlage
[7] Advanced Photon Source

2 X-ray Spectroscopy

There are several kinds of interactions of X-rays with matter, specifically X-ray absorption, elastic scattering and inelastic scattering[112]. An absorption process takes place when an incident photon gives up all its energy promoting a bound electron into a higher atomic level or into the continuum. The energies required for these absorption processes typically lie in the 0.2 - 20 keV range. X-ray radiation with energies in the 0.2 - 3 keV range is also called soft X-rays, from 2 - 5 keV they are sometimes referred to as "tender" X-rays, while the energy range from 5 to 30 keV refers to hard X-rays. However, there is no standard definition for these values and the transitions are fluid. While soft X-rays are readily absorbed in air (requiring experiments with vacuum chambers), hard X-ray experiments may be undertaken in air (or a protective gas). Hard X-rays offer the advantage to investigate matter with their wavelengths being on the order of the inter-atomic spacing of condensed matter and their energy covering plenty of atomic transitions. In addition, the interaction of X-rays with matter is used in X-ray optics to modify the parameters of X-ray beams, e.g. to change their direction, focus them or define their energy bandwidth. Understanding the interaction of X-rays with matter is the key to understanding the basics of science with synchrotron radiation. In this chapter, we give an introduction to the different interaction mechanisms. Based on these, different X-ray spectroscopy techniques which are relevant to this thesis will be explained, pointing out their differences and similarities.

2.1 Basic Interactions with Matter

Four basic interactions occur when X-rays strike matter: Reflection, absorption, scattering and transmission[50]. Figure 2.1 shows an illustration of the four processes. In the case of hard X-rays, reflection plays a role at very shallow angles, when total external reflection is possible. In this thesis, scattering and absorption are the most relevant effects to be discussed. There are several scattering and absorption effects. Being the carrier of the electromagnetic force, photons interact strongly with the electrons and - at higher energies - also with the nuclei in matter. As an example, Figure 2.2 shows the energy-dependent cross-section of different interaction mechanisms with iron[8]. Up to several tens of keV, the photo-electric effect dominates the total cross-section. At higher energies, incoherent scattering prevails, until pair production (simultaneous creation of a positron and an electron) becomes energetically possible. In this thesis the photon energies are in the energy regime well below 100 keV, therefor pair production can be neglected and we only describe the photons interacting with bound electrons. Derived from the photon-electron

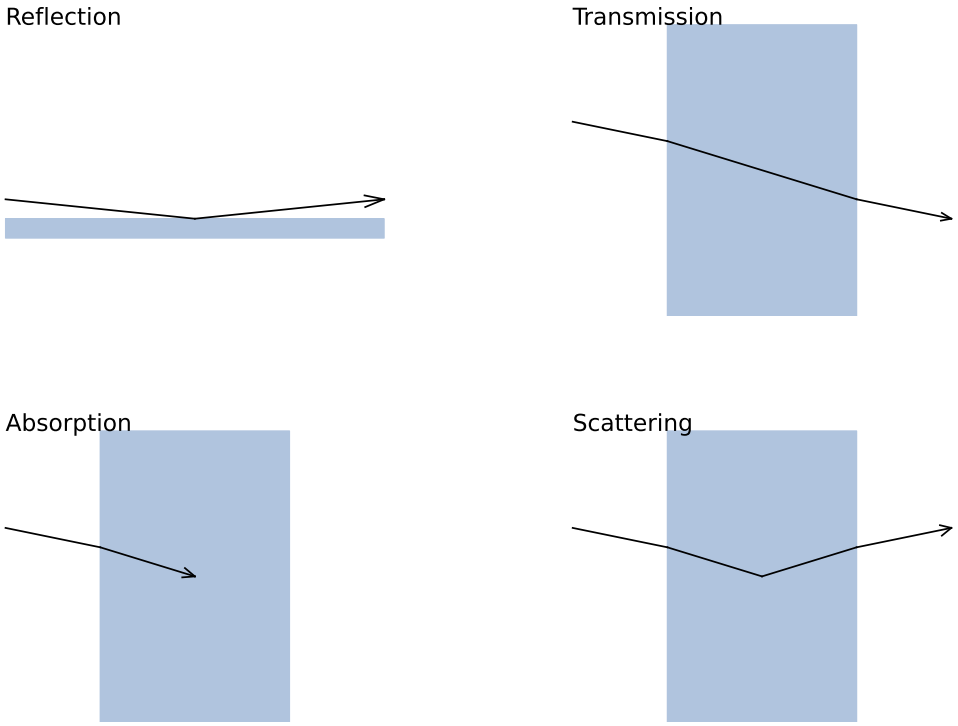

Figure 2.1: The four basic interactions of X-rays with matter. For X-rays with energies above several keV total reflection only occurs under very shallow angles (top left). For transmitted X-rays most materials exhibit a refractive index which real part is smaller than 1, leading to an increased angle of refraction when propagating from continuum into matter (top right). Absorption and scattering (lower left and lower right) of X-rays depend a lot on the electron density in the material, as we will discuss in this chapter.

interaction Hamiltonian, the double differential scattering cross-section of a photon with incoming wave vector $\mathbf{k}_1$, energy $\hbar\omega_1$ and polarization $\boldsymbol{\epsilon}_1$ and outgoing wave vector $\mathbf{k}_2$, energy $\hbar\omega_2$ and polarization $\boldsymbol{\epsilon}_2$ by an electron bound in an atom described as a second-order process is given by the Kramers-Heisenberg formula[68]. In general, we follow the notation of [91] as it gives a compact, yet detailed, description of most X-ray spectroscopy techniques relevant to this thesis and connects them accordingly. In addition, we use [32] and [97]. In the quantum mechanical representation, Kramers-Heisenberg-formula can

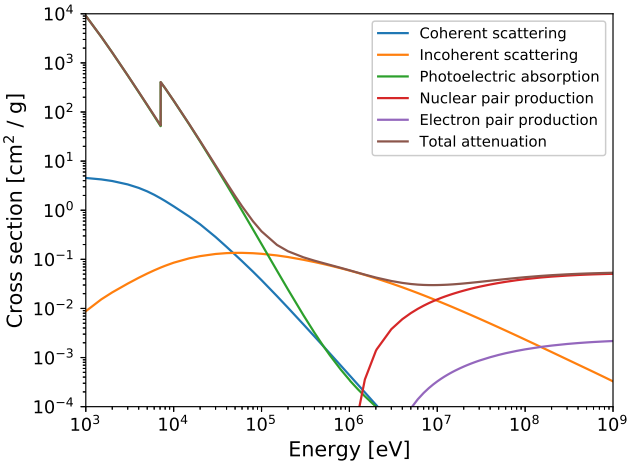

Figure 2.2: Cross-sections of the different interaction mechanisms of X-rays with atomic iron and their sum[8].

be written as:

$$\begin{aligned}\frac{\mathrm{d}^2\sigma}{\mathrm{d}\Omega \mathrm{d}\hbar\omega_2} = r_0^2\left(\frac{\omega_2}{\omega_1}\right)\sum_f \Bigg| \langle \mathrm{f}| \sum_j e^{i\mathbf{q}\cdot\mathbf{r}_j}|\mathrm{i}\rangle(\boldsymbol{\epsilon}_1\cdot\boldsymbol{\epsilon}_2^*) \\ + \frac{\hbar^2}{m}\sum_n\sum_{jj'}\Bigg(\frac{\langle \mathrm{f}|\frac{\boldsymbol{\epsilon}_2^*\cdot\mathbf{p}_j}{\hbar}e^{-i\mathbf{k}_2\cdot\mathbf{r}_j}|\mathrm{n}\rangle\langle \mathrm{n}|\frac{\boldsymbol{\epsilon}_1\cdot\mathbf{p}_{j'}}{\hbar}e^{i\mathbf{k}_1\cdot\mathbf{r}_{j'}}|\mathrm{i}\rangle}{E_i - E_n + \hbar\omega_1 - i\frac{\Gamma_n}{2}} \\ + \frac{\langle \mathrm{f}|\frac{\boldsymbol{\epsilon}_1\cdot\mathbf{p}_j}{\hbar}e^{i\mathbf{k}_1\cdot\mathbf{r}_j}|\mathrm{n}\rangle\langle \mathrm{n}|\frac{\boldsymbol{\epsilon}_2^*\cdot\mathbf{p}_{j'}}{\hbar}e^{-i\mathbf{k}_2\cdot\mathbf{r}_{j'}}|\mathrm{i}\rangle}{E_i - E_n + \hbar\omega_2}\Bigg)\Bigg|^2 \\ * \delta(E_i - E_f + \hbar\omega)\end{aligned} \tag{2.1}$$

with $\hbar$ the reduced Planck constant, r_0 the classical electron radius and m the electron mass. p and r represent the electron momentum and position. In Fermi's golden rule the term $\langle b|\mathbf{T}|a\rangle$ describes the transition from the initial state |a> to final state |b> with the transition probability defined by the matrix element T. In our case the states are |i> (inital), |f> (final) and |n> (intermediate). Γ_n represents the finite life time of the intermediate state and eliminates divergences. The momentum transfer $\mathbf{q}$ = $\mathbf{k}_1$ - $\mathbf{k}_2$ can be approximated by[91]:

$$\mathbf{q} \approx 4\pi\frac{\sin(\frac{2\theta}{2})}{\lambda}, \tag{2.2}$$

where the scattering angle (2θ) is defined as the angle of the outgoing photon with regards to the incoming photon and λ is the wavelength of the incoming photon.
Figure 2.3 shows a scattering process without intermediate state |n>. Depending on which of the photons (incoming and/or outgoing) we focus on, we can discuss the different ideas behind the X-ray spectroscopies used in this thesis. As shown here, it can be used to represent the process of X-ray Raman scattering (XRS), which is described later

in this chapter.

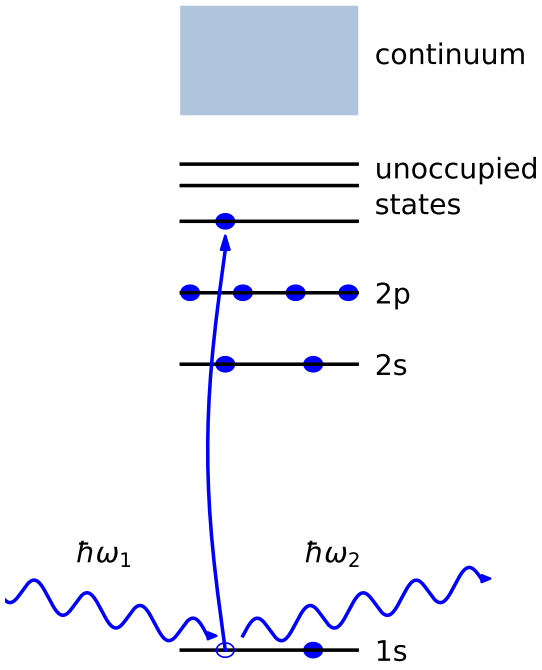

Figure 2.3: Photon scattering of a bound electron, promoting the electron to an unoccupied state and resulting in a core hole. In this two photon scattering process, the incoming photon can transfers momentum and energy to the sample, resulting in a deflection and energy loss of the outgoing photon.

2.2 X-ray Spectroscopies

Various tools to study the local atomic and electronic structure of matter are based on the absorption and subsequent emission process of the incident X-ray photon. Resulting from the very characteristic properties of X-rays interacting with different materials, one receives a diverse set of techniques to investigate matter. In this thesis, we exploit spectroscopic, i.e. energy-dependent, techniques. They can be used to study the electronic structure and other properties of the material. There are X-ray absorption and

(non-resonant) X-ray emission spectroscopy, which are based on the photo-electric interaction. Incoherent X-ray scattering offers different kinds of spectroscopic methods. In the non-resonant case, we will focus on X-ray Raman scattering to study core electron excitations, which is considered a two-photon process[91]. These spectroscopic techniques will be explained in the following.

2.2.1 X-ray Absorption Spectroscopy

While propagating through an absorbing medium, the number of photons being transmitted I(E,x), is given by:

$$I(E,x) = I_0\, e^{\frac{-x}{\lambda(E)}}, \tag{2.3}$$

where I_0 is the initial intensity, x is the thickness of the medium, and $\lambda(E)$ the energy-dependent attenuation length. For hard X-rays, $\lambda(E)$ depends strongly on the electron density in the material and is typically on the order of several microns up to a few millimeters. As an example, Figure 2.4 shows the energy dependence of the attenuation

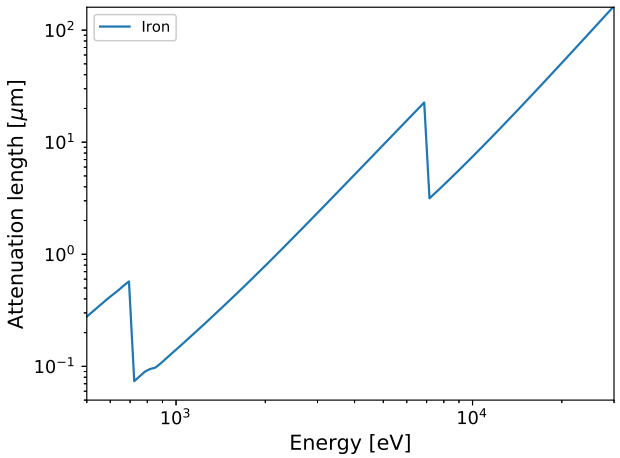

Figure 2.4: Attenuation length of solid iron as a function of the photon energy[4]. The attenuation length decreases around 700 and 7000 eV due to the ionization energies of the iron L- and the K-shell electrons.

length of pure iron[4]. The two drops at around 700 and 7000 eV are due to the ionization energies of the iron L- and the K-shell electrons. Equivalent to the absorption length, one can define the attenuation coefficient $\mu(E)$ as the inverse attenuation length $\mu(E) = 1/\lambda(E)$, which yields Beer-Lambert's law[20]:

$$I(E,x) = I_0\, e^{-x\,\mu(E)}.$$

The attenuation coefficient is the physical quantity measured by X-ray absorption spectroscopy (XAS)[37][86]. It is a technique that measures the attenuation usually in the vicinity of an element-specific ionization energy of core electrons. As a result, one receives information about the unoccupied electronic states of the specified element, directly related to the oxidation state. It is sensitive to the coordination, spin-state, symmetry (orbital), local structure and bond types. To record a XAS spectrum, one needs to tune the energy of the incoming photons and measure the flux of the incident photon beam, while simultaneously detecting either the photons transmitted through the sample or the sample's emitted fluorescence photons. Figure 2.5 shows the principle of X-ray Absorption in a single-particle picture. If the energy of the photons is sufficient, the photons can excite core electrons to unoccupied valence orbitals. Due to these additional excitation channels, the attenuation coefficient increases accordingly. In the general case, these transitions follow the dipole selection rule for the orbital quantum number l, $\Delta l = \pm 1$. This means, by exciting electrons from a different core-shell, one can obtain information of different unoccupied orbitals. Following the notation of Equation 2.1, the cross-section of the XAS process is proportional to

$$\sigma_{\mathrm{XAS}}(\omega_1) \propto \sum_n | < f|\boldsymbol{\epsilon}_1 \cdot \mathbf{r}|i > |^2 \delta(E_i - E_f - \hbar\omega_1). \tag{2.4}$$

The XAS spectrum above the absorption edge can be split up into two different regions[64]. The energy range close to this main edge yields the so called X-ray absorption near edge structure (XANES) while the subsequent extended X-ray absorption fine structure (EXAFS) measures subtle changes far above the absorption edge[88][37][49]. Figure 2.6 shows an EXAFS-spectrum of 20 mM $[\mathrm{Fe(II)(bpy)_3}]^{2+}$ in aqueous solution. The transition between the XANES and the EXAFS region is not well-defined, and the data analysis of both regions often overlap. Roughly, this transition can be seen as where the photoelectron wavelength $\lambda = \frac{h}{\sqrt{2m_e(\hbar\omega_1 - E_{ion})}}$ becomes shorter than the interatomic distances in the material, which for 3d metals and their molecular compounds typically occurs 20-50 eV above the ionization energy E_{ion} of the excited core electron. In the case of 3d-metals, the XANES region of the K-edge spectrum also exhibits pre-edge transitions emerging from dipole-forbidden excitations from 1s to 3d, yielding information about the orbitals directly above the Fermi level. The XANES region also contains information about the valency of the system which exhibits for example energy shifts of the main edge as a function of oxidation state. The EXAFS region yields information about the distance of the atoms surrounding the excited atom and its coordination. X-ray Raman scattering (XRS) represents an indirect alternative method to measuring soft X-ray absorption edges, utilizing the inelastic scattering of hard X-rays. XRS will be explained later in subsection 2.2.4. For XAS there are different detection schemes, which we will explain in the following.

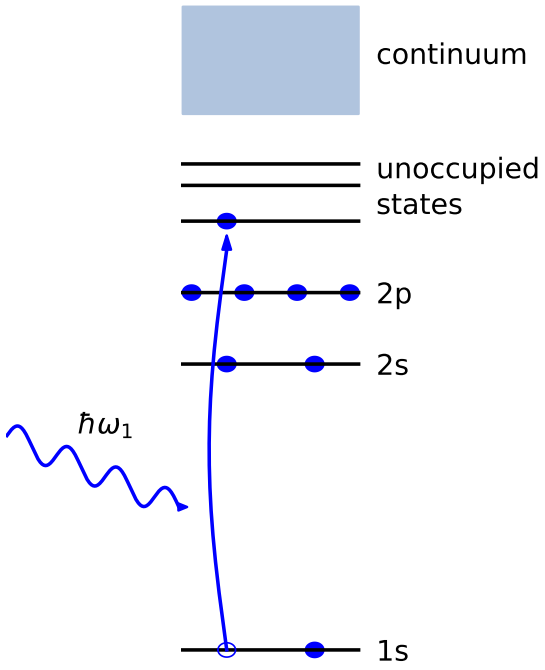

Figure 2.5: Principle of X-ray absorption in a single-particle picture. An X-ray photon with certain energy excites a core electron to an unoccupied valence state.

Transmission Mode Detection

The most intuitive detection setup of XAS is the transmission measurement. To record an XAS spectrum in transmission mode, one measures the intensity of photons in front of and behind the sample. By comparing the flux before and after the sample, one receives the attenuation coefficient via Beer-Lambert's law by:

$$\mu(E) = \frac{1}{x} ln(\frac{I(E)}{I_0(E)}),$$

where x is the sample thickness, $I_0(E)$ is the initial X-ray flux and $I(E)$ is the flux behind the sample. The sample thickness ideally needs to be around the attenuation length, to achieve a good ratio between $I_0(E)$ and $I(E)$. A spectrum recorded by this method is broadened by the lifetime of the excited state, usually governed by the core-hole lifetime, which lies around roughly 1 fs for the K-edge of 3d-metals, corresponding to 1 eV

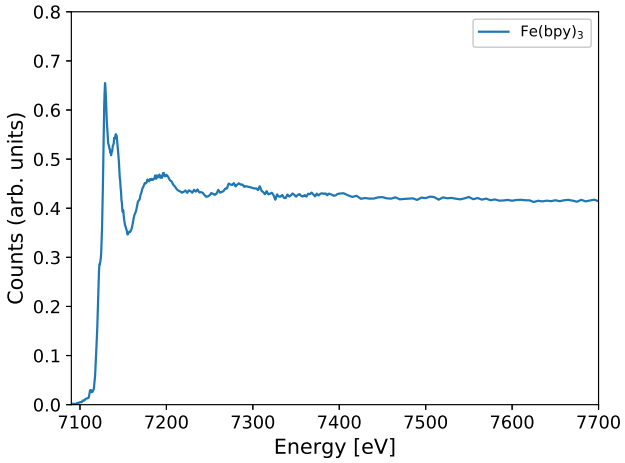

Figure 2.6: Normalized EXAFS spectrum of 20 mM $[Fe(II)(bpy)_3]^{2+}$ in aqueous solution, recorded at beamline P01, PETRA III, during a pump-probe experiment (the fluctuations stem from instabilities in the jet, which, due to the shot-to-shot normalization, did not hamper the signal quality of the transient).

broadening[41]. The broadening increases with the atomic number of the element.

Total and Partial Fluorescence Yield Detection

If the sample is too thick or contains heavier (i.e. more absorbing) atoms, it may occur that too few photons transmit through the sample. But also if the sample is too thin, the contrast between incoming and outgoing photon beam can be low. To overcome the requirement of the sample being able to transmit or absorb enough X-rays, one often measures the attenuation coefficient via the total or partial fluorescence yield (TFY / PFY) of the sample. However there can be deviations in the X-ray absorption spectra detected via fluorescence yield[70]. To measure the TFY, one collects the X-ray photons emitted by the sample usually by placing a detector next to the sample. In case of linearly polarized X-rays, one can place it at $90°$ to the incident beam, in order to minimize the contribution of scattered photons (related to the Thomson-scattering cross-section, explained later). Then the detector mainly measures all the emitted fluorescence photons within the solid opening angle determined by the detector surface and its distance to the sample. The lifetime broadening of the short-lived excited state leads to the same broadening of the X-ray absorption spectrum as in transmission mode. The cross-section of the TFY method is proportional to:

$$\sigma_{\text{XAS, TFY}}(\omega_1) \propto \sum_n | < n|T|i > |^2 \frac{\frac{\Gamma_n}{2\pi}}{(E_n - E_i - \hbar\omega_1)^2 + \frac{\Gamma_n^2}{4}}. \tag{2.5}$$

A problem that can occur during TFY (and transmission) measurements are other sources of emission (scattering and absorption), which can add undesired background signals to the desired emission[42]. This occurs for example when cobalt is abundant in a sample, where one wants to measure the iron EXAFS spectrum. In order to overcome this difficulty in TFY, one discriminates the emitted photons by their emission energy, which leads to PFY. This can be done to some extent by using an absorbing foil (usually Z - 1 with respect to the element under study) to block a part of the higher energetic Kβ emission, which lies energetically just above the Z-1 absorption edge. Another way to collect PFY signal is to use a detector able to discriminate the photons by their energy. This is usually done by evaluating the photocurrent generated by single fluorescence photons. The energy resolution of semiconductor detectors usually lies on the order of a few hundred eV, enough to distinguish between Kα and Kβ radiation of 3d-metals. The extracted cross-section of the PFY method is proportional to:

$$\sigma_{\text{XAS, PFY}}(\omega_1) \propto \sum_n |<n|T|i>|^2 \frac{1}{(E_i - E_n + \hbar\omega_1)^2 + \frac{\Gamma_n^2}{4}} \frac{\frac{\Gamma_f}{\pi}}{(E_n - E_i - \hbar\omega_1)^2 + \frac{\Gamma_f^2}{4}}. \quad (2.6)$$

Γ_f represents the finite lifetime of the final state.

High Energy Resolution Fluorescence Detection

There is a third technique to measure the X-ray absorption spectrum, called high energy resolution fluorescence detection (HERFD) XAS[72]. For this technique, one uses analyzer crystals to precisely measure the spectrum of the emitted photons. While the setup is much more elaborate compared to the previously introduced XAS techniques, which only require single photon counting detectors, collimators and Z-1 filters, it comes with certain benefits. The advantage of HERFD lies in the very low background signal, which can become very important in crystalline samples, where Bragg peaks occur thus adding undesired background to the signal. It can also be used to reduce the effect of lifetime broadening.

2.2.2 X-ray Emission Spectroscopy

X-ray emission spectroscopy (XES) probes the occupied orbitals of certain atoms or molecules[25][115]. Like XAS, XES is also element specific[22]. Figure 2.7 shows the principle of non-resonant XES. Before the emission process, following the absorption of an X-ray photon with sufficient energy, a core electron is ejected. The created core-hole has a limited lifetime and decays due to an electron from a higher shell relaxing into the

hole. As a consequence, an X-ray photon is emitted with the energy corresponding to the transition. The short lifetime of the core-hole (again in the femtosecond regime) leads to a finite width of the emission line. For 3d-metals this broadening is typically a few eV[41]. To measure XES spectra in non-resonant mode, one needs to measure the energy

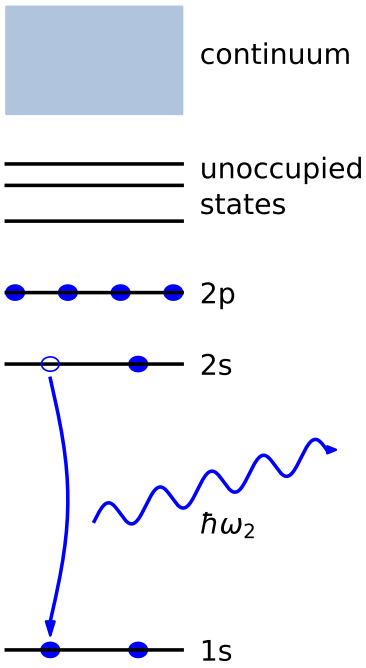

Figure 2.7: Principle of X-ray emission spectroscopy in a single-particle picture. An X-ray photon well above the ionization energy excites the system and creates a core-hole. Subsequently, the core-hole decays and emits an X-ray photon with characteristic energy

of the photons being emitted by the sample. If the energy of the emitted photons is above a few keV, this is typically done by using a setup consisting of analyzer crystals and a detector[33]. Some examples of setups in Johann and von Hámos geometry are given in chapter 4. To create the emission signal, one needs X-ray photons with energy well above the ionization energy of the desired edge. The incident energy does not need to be well defined, as the energy distribution of the emitted photons purely depends on the

electronic transitions within the sample. The cross-section of XES is proportional to:

$$\sigma_{XES}(\omega_2) \propto |\frac{< f|\boldsymbol{\epsilon}_2 \cdot \mathbf{r}|n >< n|a_\epsilon|i >}{E_f - E_n + \hbar\omega_2 - i\frac{\Gamma_n}{2}}|^2, \tag{2.7}$$

with a_ϵ being the electron annihilation operator. The emission lines of the sample are broadened by up to several eV, due to the very short lifetime of the core-hole excited state. Independent of the direction or polarization of the incoming beam, the emission photons are emitted isotropically.

For 3d-elements, the K shell emission spectrum can be separated into three regions, the Kα, Kβ and valence-to-core (vtc) region.

Kα Emission

The Kα are the strongest emission lines. Its origin is the transition of 2p electrons to the 1s core-hole. It is a doublet due to the energetic splitting of the $2p_{1/2}$ and $2p_{3/2}$ orbitals. It contains information on the spin states of the 3d electrons[41].

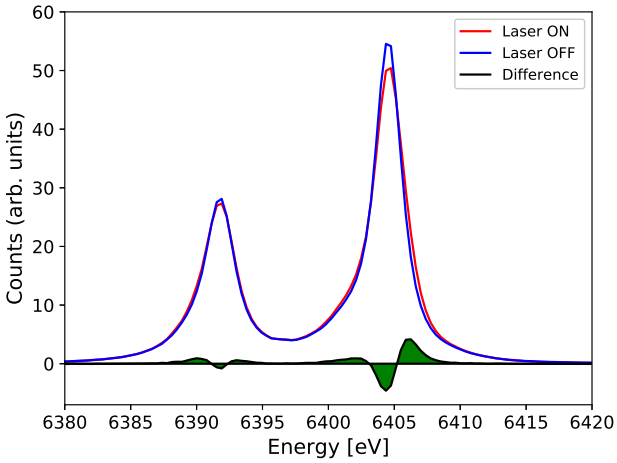

Figure 2.8: Non-resonant Kα emission signals of iron (II) complexes ($[Fe(terpy)_2]^{2+}$) in aqueous solution in the ground state low-spin configuration (S=0) and after photoexcitation (with high (S=2) spin contributions) of the 3d orbitals. Recorded at beamline 7ID-D, APS and published[73].

Figure 2.8 shows an iron-based complex in different spin configurations and the different signal this induces in the Kα spectrum.

Kβ Emission

The Kβ emission lines, also known as K$\beta_{1,3}$ are about a factor ten weaker than the Kα spectrum and originate from the 3p to 1s transition[41]. It is more sensitive to changes in the spin, as can be seen in Figure 2.9. The spin state has a strong influence on the Kβ' feature, which stems from a direct consequence of the occupation of 3d-levels. It changes the monotonic decaying shoulder into a new peak, whose intensity grows with the spin state. This feature is often used for spin state studies. One can also exploit this spin-up and spin-down sensitivity for HERFD.

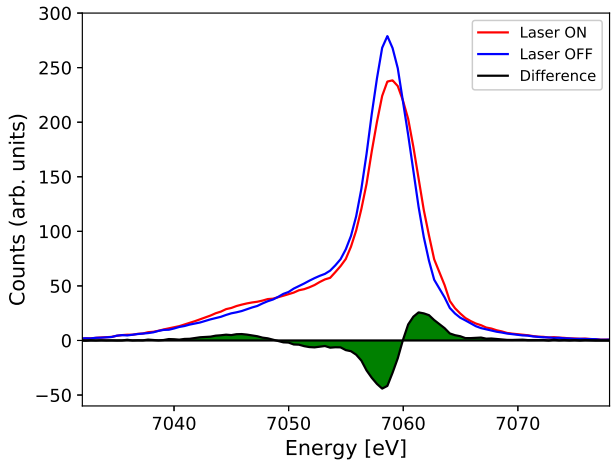

Figure 2.9: Non-resonant Kβ emission signals of iron (II) complexes ($[Fe(terpy)_2]^{2+}$) with low and partial high-spin configuration ((S=2) and (S=0)). The estimated excitation yield is ca 1/6, as shown in subsection 4.5.1. Spectra recorded at beamline 7ID-D, APS and published[73].

Valence-to-Core Emission of 3d Metals

Finally, higher emission energies - albeit with low yield - from the valence electrons right below the Fermi level, are possible. Valence-to-core (vtc)-emission, for 3d metals the peaks above the K$\beta_{1,3}$ emission line, is roughly a factor 100 smaller than their K$\beta_{1,3}$ line[39]. This is also caused by the dipole-forbidden transition of valence orbitals, mainly 3d to 1s. As the spin configuration is defined by the 3d valence electrons, the vtc spectrum has the potential to reveal a much more pronounced signature for different spin states. Figure 2.10 shows the same iron (II) samples in high and low-spin configuration.

As the valence electrons reach out to valence orbitals of neighboring atoms, they are

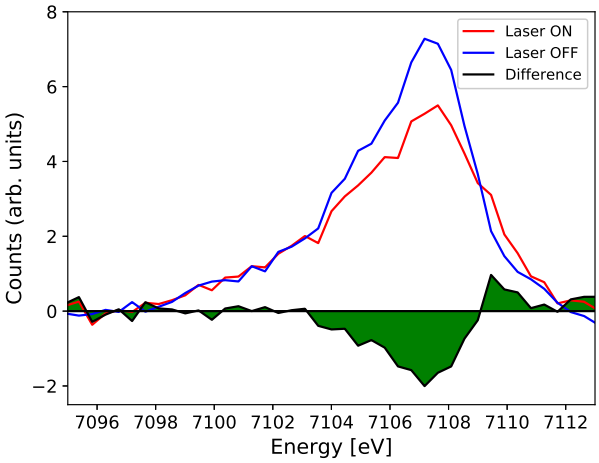

Figure 2.10: Non-resonant VtC or K$\beta_{2,5}$ emission signals of iron (II) complexes ($[Fe(terpy)_2]^{2+}$) before and after photoexcitation, thus in its low-spin state and with high-spin contributions. Recorded at beamline 7ID-D, APS and published[73].

much more sensitive to the chemical environment, hence vtc emission yields sensitive information about these neighboring atoms, including charge and bond distances, this is presented in chapter 5[41][103].

2.2.3 Resonant X-ray Emission Spectroscopy

Resonant X-ray emission spectroscopy (RXES) is a special type of XES, where the energy of the incoming X-ray photons, which create the core-hole, is chosen in such a way, that it exactly matches certain transition energies to selectable unoccupied states (represented in Figure 2.11)[66]. In that sense, RXES combines the requirements of XAS (defined energy of incoming photons) with XES (measure the energy of the emitted photons). As it involves different excitation mechanisms, it can be used to suppress the lifetime broadening of common XES lines[41][44]. Following the notation of Equation 2.1, the cross-section is proportional to:

$$\sigma_{\mathrm{RXES}}(\omega_1,\omega_2) \propto |\frac{< f|\boldsymbol{\epsilon}_2\cdot\mathbf{r}|n >< n|\boldsymbol{\epsilon}_1\cdot\mathbf{r}|i >}{E_i - E_n + \hbar\omega_1 - i\frac{\Gamma_n}{2}}|^2\delta(E_i - E_f + \hbar\omega_1 - \hbar\omega_2). \tag{2.8}$$

In addition, RXES can be used to study the influence of certain transitions by resonantly enhancing the transition cross-section. Depending on the polarization of the incoming photons, the emission is no longer isotropic[67]. RXES is also often referred to as (direct) resonant inelastic X-ray scattering (RIXS). As one of the specialties of P01 is the (indirect) RIXS technique, we would like to emphasize the difference and use the term RXES for processes where first a core electron is excited to an unoccupied state and subsequently

another electron decays back into the core hole. In (indirect) RIXS an electron is first excited to an unoccupied state and the same electron decays into the core hole, while certain valence excitations are enabled by the resulting Coulomb interaction.

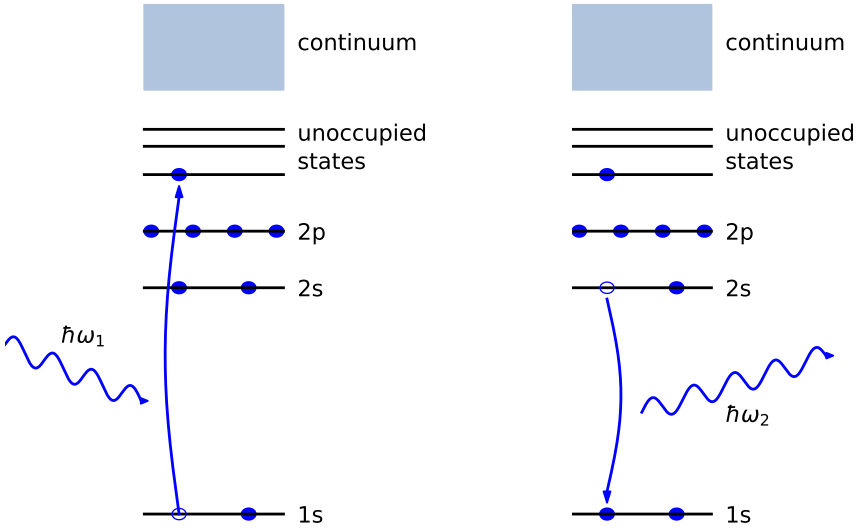

Figure 2.11: The RXES or direct RIXS process. An X-ray photon with a defined energy excites a core electron to an unoccupied orbital. Subsequently, the system relaxes into the core-hole, and an X-ray corresponding to the energy level of the decaying state is emitted, here for the case of Kα emission.

2.2.4 Non-Resonant Inelastic X-ray Scattering

Inelastic X-ray Scattering (IXS) can be resonant (RIXS) and non-resonant (NIXS)[47]. In basic NIXS, a photon with a well-defined energy strikes the sample and transfers a part of its energy and momentum to the sample. The energy and momentum of the outgoing photon are then measured and collected by a detector[93]. Inelastic scattering experiments with X-rays can cover momentum transfers of several Brillouin zones while resolving the energy down to sub-meV scale. The energy of the scattered photons is measured typically with an analyzer (or a grating in the case of soft X-ray) and detector setup. This process can be used to probe several material properties not accessible with common emission or absorption techniques. Figure 2.12 from and Table 2.1 give an overview of the variety of observables accessible via IXS[18][100].

Table 2.1: Different IXS techniques and the information they can reveal. Adapted from [18]

	Technique	**Incident Photon Energy**	**Energy**	**Information Content**
1	Compton	100 keV	keV	Electron Momentum Density Fermi Surface Shape
2	Magnetic Compton	100 keV	keV	Density of Unpaired Spins
3	RIXS Resonant IXS	4-20 keV	0.1-50 eV	Electronic Structure Excitations
4	SIXS Soft X-ray IXS	0.1 - 2 keV	0.01 - 5 eV	Electronic + Magnetic Structure + Excitations
5	NIS (NRVS) Nuclear IXS	10 - 30 keV	1-100 meV	Element Specific Phonon Density of States (DOS)
6	X-ray Raman	10 keV	50 -1000 eV	Edge Structure, Bonding, Valence
7	NRIXS Non-Resonant IXS	10 keV	0.01 - 10 eV	Electronic Structure + Excitations
8	IXS High Resolution IXS	10-25 keV	1-100 meV	Atomic Dynamics Phonon Dispersion

The double differential cross-section for NIXS is given by:

$$\frac{\mathrm{d}^2\sigma}{\mathrm{d}\Omega_2 \mathrm{d}\hbar\omega_2} = (\frac{\mathrm{d}\sigma}{\mathrm{d}\Omega_2})_{Th} S(\mathbf{q},\omega) \tag{2.9}$$

where

$$(\frac{\mathrm{d}\sigma}{\mathrm{d}\Omega_2})_{Th} = r_0^2 (\frac{\omega_1}{\omega_2}) |\boldsymbol{\epsilon}_1 \cdot \boldsymbol{\epsilon}_2^*|^2 \tag{2.10}$$

represents the scattering by free electrons and is referred to as Thomson scattering. And

$$S(\mathbf{q},\omega) = \sum_f \left| < f| \sum_f e^{i\mathbf{q}\cdot\mathbf{r}_j} |i> \right|^2 \delta(E_i - E_f + \hbar\omega) \tag{2.11}$$

represents the dynamic structure factor yielding the main information about the system.

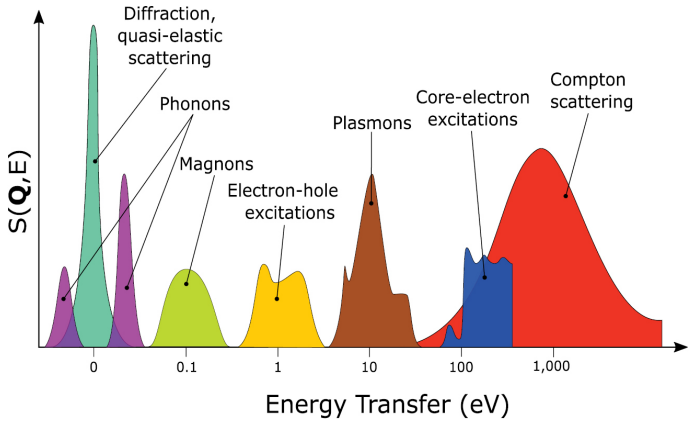

Figure 2.12: Excitations and effects that can be observed via X-ray scattering at different energy transfers[100].

Thomson Scattering

Thomson scattering describes the effect of electromagnetic radiation being elastically scattered by free charged particles. In our case, X-ray photons are scattered by electrons contained in matter. Considering the X-ray energy is well above the binding energy, one can assume the electrons as quasi-free. The most important feature of the elastic scattering at synchrotron sources is the polarization dependence of the cross-section, expressed as:

$$\frac{d\sigma_{el}}{d\Omega} \propto \frac{d\sigma_T}{d\Omega} * \cos^2(\theta).$$

with $\frac{d\sigma_T}{d\Omega}$ being the Thomson scattering cross-section of an electron and θ the scattering angle along the electric field vector of the incident beam. As a consequence, at $\theta = 90$ the contribution of elastic scattering vanishes. This angular dependence also applies to inelastic X-ray scattering. The X-ray radiation coming from undulators is linear polarized. Considering this during the design of an experimental setup can help to reduce the background caused by scattering or maximize the scattering signal.

Compton Scattering

Compton scattering describes the inelastic scattering of a photon by a free charged particle, where the photon transfers part of its energy to the charged particle. In the case of this thesis, these charged particles are electrons. In a usual IXS experiment, the energy of the incoming photons lies much higher than most of the ionization energies of the atoms in the sample, so the excited electrons can be treated as quasi-free. In the case of inverse Compton scattering, photons gaining energy by scattering from higher energetic electrons, can be neglected in the case of X-rays. Figure 2.13 shows the Compton signal

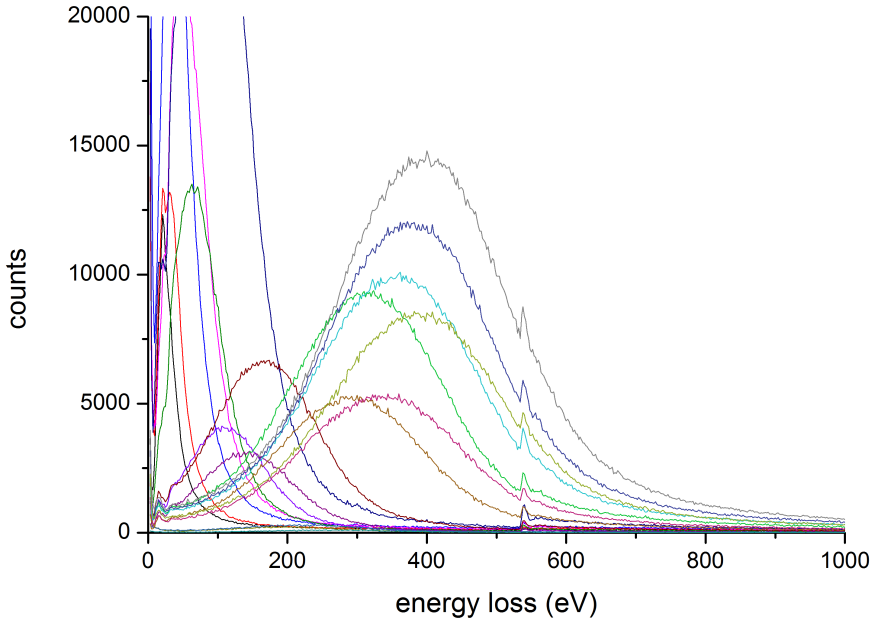

Figure 2.13: Inelastic X-ray scattering spectra of water, each spectrum was collected simultaneously, but at different scattering angles. The peak at zero energy transfer region originates from Thomson scattering and is usually referred to as the (quasi-) elastic line. The large shifting peaks are caused by Compton scattering. The peak at 540 eV originates from the oxygen K-edge. The spectra were recorded with the LERIX setup of 20ID beamline at the APS. 19 Analyzers at different scattering angles simultaneously recorded XRS spectra with momentum transfers varying from about 1 $Å^{-1}$ up to 10 $Å^{-1}$. The different intensities of the spectra are due to a combination of different cross-sections at different scattering angles as well as shielding effects from the sample geometry, where we installed a horizontally mounted liquid jet to measure water under ambient conditions.

of water, measured simultaneously at different scattering angles, i.e. different momentum transfers. With higher momentum transfer, the Compton peak shifts towards higher energy transfers. The peak at 0 eV energy transfer was identified as the Thomson peak and used to calibrate the energy. The smaller peak around 540 eV originates from the Oxygen K absorption edge. Using inelastic scattering of hard X-rays to measure the X-ray absorption spectrum of such low energetic transitions is referred to as X-ray Raman spectroscopy[23].

X-ray Raman Scattering

Utilizing hard X-ray photons, XRS can be used to measure soft X-ray absorption edges[79]. As mentioned before, Figure 2.3 shows the principle of XRS. Compared to soft X-ray absorption spectroscopy and electron energy loss spectroscopy, XRS offers the advantage of bulk sensitivity and the possibility to measure under ambient condition, while EELS and soft XAS require (ultra-)high vacuum conditions and probe only the surface of the material or few tens of nanometers, due to their low penetration depths. This makes XRS the only suitable technique to measure soft X-ray edges in complex sample environments, for example flow cells or diamond anvil cells[61][87]. Another benefit of XRS is the possibility to vary the momentum transferred to the system. This can be used to alter the dipole selection rule Δl +/- 1 in order to investigate higher-order (quadrupole and octupole) transitions. On the other hand, XRS has a low cross-section which usually forces the experiment to be done with an energy resolution between 0.5 and 2 eV. In the low q range, the cross-section of XRS is proportional to

$$\sigma_{XRS}(\mathbf{q},\omega) \propto | < f|\mathbf{q}\cdot\mathbf{r}|i > |^2 \delta(E_i - E_f + \hbar\omega). \tag{2.12}$$

and in dipole approximation can directly be compared to the XAS cross-section given in Equation 2.4[79]. The XRS cross-section is usually about a factor 10^{-5} weaker than the cross-section in XAS[26]. The understanding and interpretation of XRS spectra require the understanding of Compton scattering, as it is one of the main sources for the background, as can be seen in Figure 2.13[105][93].

3 Sources of Synchrotron Radiation

Since their discovery in 1895, X-rays became increasingly important as a diagnostic tool to study the microscopic properties of matter. The techniques to generate X-rays have advanced a lot. At the very beginning, simple electron accelerator tubes generated X-rays by the decelerating electrons via interaction with matter, an effect called Bremsstrahlung. Modern X-ray tubes still use this effect, with a moderately increased intensity over the past 100 years. While Bremsstrahlung, which X-ray tubes are based on, exploits deceleration of non-relativistic charged particles, synchrotron radiation is created by the centripetal acceleration of relativistically moving particles without changing their kinetic energy significantly[112]. The most basic source of synchrotron radiation are so-called bending magnets, where single magnets are used to change the direction of relativistically moving charged particles along a curved path(Figure 3.1). Bending magnets were already present in the early accelerators used for particle physics experiments. These particle experiments aimed to use the highest possible kinetic energy and synchrotron radiation was seen as performance-disturbing, as it led to a constant loss of particle energy. Second-generation synchrotron radiation sources were soon used as dedicated X-ray sources with an improved directionality of radiation and broader accessible energy range than X-ray tubes[15]. To further increase the performance, third-generation synchrotron radiation sources were equipped with long periodic structures of magnets, so-called insertion devices. This led to a boost in brilliance (see below) and coherence of synchrotron X-ray radiation sources. There are two types of insertion devices, called wiggler and undulator. The currently most advanced type of synchrotron radiation source is the X-ray free electron laser, which uses even longer periodic magnetic structures (arrays of many undulators) to induce self-ordering effects in the electron bunches created by self-amplified spontaneous emission of synchrotron radiation[55].

3.1 Synchrotrons and Storage Rings

A synchrotron is a circular shaped particle accelerator. The name synchrotron ("synchronous cyclotron") originates from the necessity to synchronize the magnet field strength according to the increasing kinetic energy and mass of the charged particles. By ramping the field strength, the particles can be kept in the same orbit. Meanwhile these synchrotrons are found as so-called boosters in modern synchrotron radiation storage rings. These boosters create the final energy of particles (typically in the few GeV range), which are then fed into the circular structure, which only replenishes the energy lost to radiation during one round trip with radio frequency accelerator modules and

store them for several hours. The synchrotron radiation storage rings used in this thesis operate with electrons. These move within the storage ring in bunches of up to 10^{10-11} electrons (or up to 1-10 nC total charge). While dipole magnets are used to change the direction of the electron bunches, quadrupole magnets focus them onto the beam path. Due to Coulomb repulsion, these electron bunches have a finite size and need to be constantly refocused. Due to Liouville's theorem, the focussing just improves the beam properties in single directions, while the four-dimensional phase-space of the bunch (also referred to as its emittance) remains constant. After focussing, sextupole magnets are used to correct for chromatic distortion induced by the quadrupole magnets. The X-ray beam quality of a synchrotron is usually described by its brilliance B, which is defined as

$$B = \frac{N_\gamma}{t\,\delta\theta\,\delta\sigma\,BW},$$

with N_γ the number of photons, t the time, $\delta\theta$ the beam size, $\delta\sigma$ the beam divergence and BW the energetic bandwidth. It describes the photon flux in dependence of the source size and beam divergence within a certain energy bandwidth. Modern synchrotrons (e.g. PETRA III) have an average brilliance of up to 10^{21} $\frac{N_\gamma}{s\,mrad^2\,mm^2\,0.1\%BW}$ and diffraction-limited synchrotrons are expected to deliver brilliance values up to 10^{23} $\frac{N_\gamma}{s\,mrad^2\,mm^2\,0.1\%BW}$[9].

3.1.1 Insertion Devices - Wiggler and Undulator

As mentioned above, synchrotron radiation is already generated by a single bending magnet, but special magnetic structures have been developed to improve its brilliance. An array of periodically arranged magnets is referred to as undulator or wiggler. These are distinguished by the amount of deflection of the electrons by the magnetic field B, which is summarized in the so-called deflection parameter[112]

$$K = \frac{qB\lambda_u}{2\pi\beta mc}.$$

With q the charge, $\beta = \frac{v_e}{c}$ the speed and m_e the mass of the accelerated electrons, c the speed of light and λ_u, the period length of the magnets. With β being almost 1 for the case of electrons with GeV kinetic energies, K can be approximated as

$$K = \frac{eB\lambda_u}{2\pi m_e c} \approx 0.0934\lambda_u[cm]B_{peak}[T],$$

with e and m_e the charge and the mass of the electron. For K-values > 3 we speak of wigglers, while undulators typically have K < 3 values[85]. The smaller deflection of the beam yields an increased interference and thus increased on-axis intensity, and also coherence.

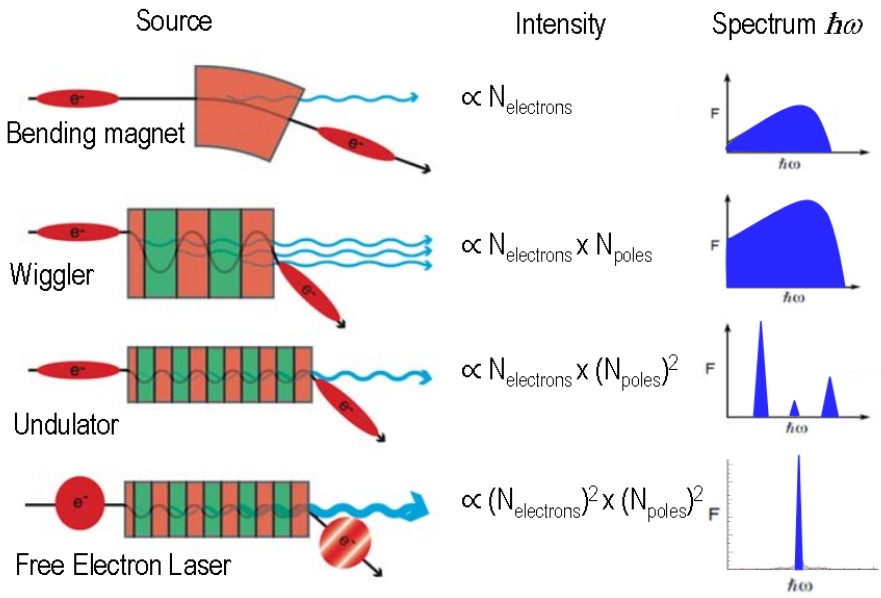

Figure 3.1: Different sources of synchrotron radiation and their intensities, roughly showing the development from first- and second-generation (bending magnets), over third-generation (wiggler and undulator) synchrotrons to the most intense free electron lasers with orders of magnitude larger peak brilliance[99].

Figure 3.1 shows typical energy spectra and intensities for different magnetic structures. For a bending magnet, the number of photons generated is proportional to the number of electrons in the bunch. For a wiggler, the intensity is proportional to the number of electrons multiplied by the number of poles. In an undulator, the energy bandwidth is proportional to the inverse number of magnetic poles. Due to this reduced bandwidth, the intensity in the remaining spectrum is proportional to the number of electrons multiplied by the square of the number of poles. In an FEL the intensity rises even more, as the electron charge contributes with the power of two to it. The central wavelength λ of the photons created by a wiggler or undulator can be calculated via:

$$\lambda(\theta, \gamma) = \frac{\lambda_u}{2\gamma^2}(1 + \frac{K^2}{2} + (\theta\gamma)^2),$$

with λ_u the period length of the magnets, $\gamma = (1 - \beta^2)^{-1}$ the Lorentz factor and θ the angle of the cone of the emitted photons (observation angle)[11][75]. For GeV electrons with γ^2 around 10^8, the creation of X-rays with Ångstrom wavelength requires magnets with a period length in the cm range.

3.1.2 Temporal Structure of Synchrotron Radiation

The electron bunches in the storage ring define the time structure or repetition rate of the emitted photon pulses via the circumference of the storage ring and the number of stored electron bunches. With the electrons moving close to the speed of light c, the overall pulse repetition rate, i.e., the number of photon pulses created per second f is given by:

$$f = N_e \frac{c}{2\pi r},$$

with N_e, the number of stored electron bunches, c the speed of light and r the radius. The inter-bunch spacing, i.e. the time between two photon bunches is then the reciprocal value of the repetition rate. Most synchrotrons can operate with different amount of electron bunches. To keep the average photon flux constant, the stored charge per bunch is changed accordingly.

3.2 PETRA III, APS, DELTA

The experiments in this thesis have been conducted at three different synchrotrons, PETRA III in Hamburg, Germany, DELTA in Dortmund, Germany as well as at the APS in Argonne, USA. Details about the experimental beamline Bl9 at DELTA can be found in [1]. Details about the endstation 7ID-D at the advanced photon source (APS) can be found in [6].

The important technical details of these synchrotrons are shown in Table 3.1. At PETRA

Table 3.1: Synchrotron radiation facilities with their important characteristics in their configuration 2015-2017.

Synchrotron	PETRA III [16]	APS [5]	DELTA [3]
Electron energy (GeV)	6.08	7	0.3 - 1.5
Beam Current (mA)	100 (120)	100	130
Circumference (m)	2304	1104	115
Emittance (nmrad)	1	3	100 [21]
Radiofrequency (MHz)	500	500	500
Endstation	P01 [2]	7ID-D [6]	BL9 [1]
Photon Source	Undulator	Undulator	Wiggler
Monochromator	Si(111), (311)	C(111)	Si(311)
Resolution ΔE/E	0.3 - 1*10^{-48}	5*10^{-5}	10^{-4}
Photon Energy(keV)	2.5 - 80	5-32	4-30
Photon Flux (photons/s)	5*10^{13}	1*10^{12}	up to 2.5*10^{9}
Focus Size (μm x μm)	10x10	10x10	500x100

III, each electron bunch is 13.2 mm long corresponding to a bunch length of 44 ps. The operation modes are generally separated into two categories, timing modes with 40 and 60 stored bunches as well as multi-bunch modes with 240, 480 or 960 bunches. The corresponding values for the repetition rate and inter-bunch spacing are shown in Table 3.2. Figure 3.2 shows the pulse sequence in a pump-probe experiment using 40 bunch mode. An insertion device creates photon pulses for the beamline, these X-ray pulses are guided to the sample, where a synchronized laser excites the sample right before the X-ray pulse strikes it, also shown in Figure 3.3. The laser excites the sample before every second X-ray pulse, to allow the quasi-simultaneous collection of reference data (laser-off) together with the data from the laser from the laser-excited sample (laser-on).

As the total beam current is set to either 100 mA or 120 mA for all operation modes, the individual electron bunch charge depends on the bunch mode, with more charges stored

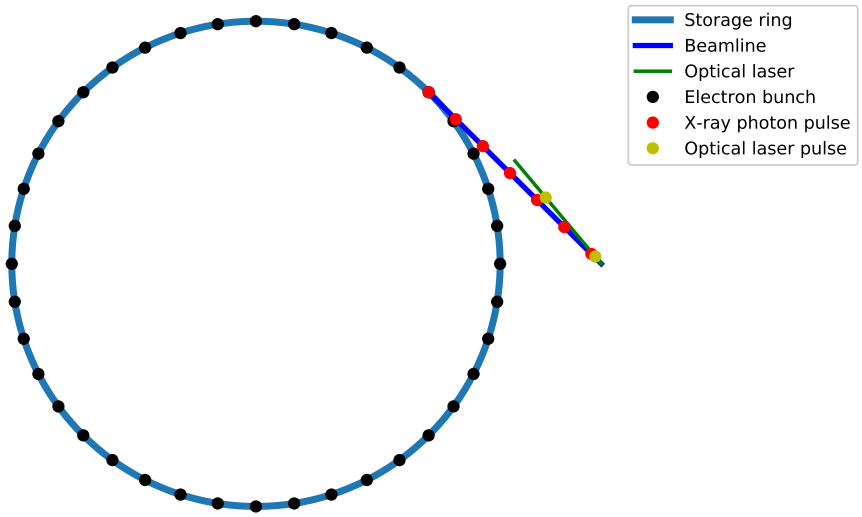

Figure 3.2: Scheme of electron and photon pulses for an optical pump X-ray probe setup at PETRA III in 40 bunch mode.

Table 3.2: PETRA III Bunch Filling Modes

Bunch Mode	Number of Bunches	Repetition Rate / MHz	Inter-Bunch Spacing /ns
Timing Mode	40	5.2	192
Timing Mode	60	7.8	128
Multi Bunch	240	31.3	32
Multi Bunch	480	62.5	16
Multi Bunch	960	125	8

per bunch in timing mode. Optical pump, X-ray probe measurements, as described in this thesis are usually performed in timing mode, since the optical can match these (lower) repetition rates. Also, most of the detectors and subsequent electronics used to detect photons allow pulse-separated recording only at somewhat lower repetition rates, due to their finite intrinsic (electronic) response times.

3.3 The High Resolution Dynamics Beamline - P01

To give an idea about the typical beamline setup used at an X-ray spectroscopy beamline, we describe Beamline P01 of PETRA III. P01 contributed to all studies presented in this thesis. The technical details for 7ID-D at APS and BL9 at DELTA and the setup varia-

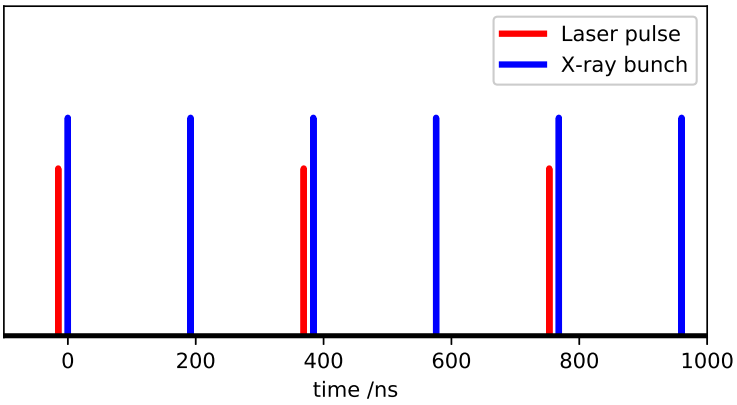

Figure 3.3: Time pattern of synchronized X-ray bunches and optical laser bunches. PETRA III is operated in 40 bunch mode, creating photon bunches with an inter-bunch spacing of 192 ns (i.e. 5.2MHz repetition rate). The optical laser is running with 2.6MHz to excite the sample just before the arrival of every second X-ray bunch.

tions at P01 are described later in this thesis for each measurement. The high Resolution Dynamics Beamline P01 is a beamline dedicated to nuclear inelastic scattering (NIS) and inelastic X-ray scattering(IXS). The first user run using NIS was in 2012 and the first user run for IXS in 2015. In 2016 a partnership between P01 and the Max-Planck Institutes in Dresden and Stuttgart started. As part of the MPI partnership, several fundamental details of the beamline setup changed. As the measurements within this thesis were performed with the old P01 setup, we will describe mainly the old setup.

3.3.1 Beamline Scheme

Beamline P01 consists of eight hutches in total, shown in Figure 3.4. The X-rays enter 5 of these hutches, two optical (OH1, OH2) and three experimental hutches (EH1-3). Next to each experimental hutch are in total three control hutches (CH1-3), where experimenters operate their experiments safely during operation. During operation (i.e. when X-rays are active) it is prohibited to be in the experimental hutches. P01 starts downstream of two 5 m long undulators in the storage ring, where the X-rays are created. The X-ray beam is guided through a 45 m long vacuum tube, directly connecting the storage ring and OH1. OH1 hosts the double crystal monochromator, which selects the desired photon energy and defines the energy resolution of the X-ray beam. In OH2 the direct connection to the storage ring vacuum ends with a diamond window and the beamline vacuum tubes start. There were mounts for high resolution monochromators (HRM), to further improve the energy resolution up to $\Delta E \approx 1\,meV$[111]. Beryllium lenses allow to collimate and/or focus the beam. Both, lense and HRM were operated in normal

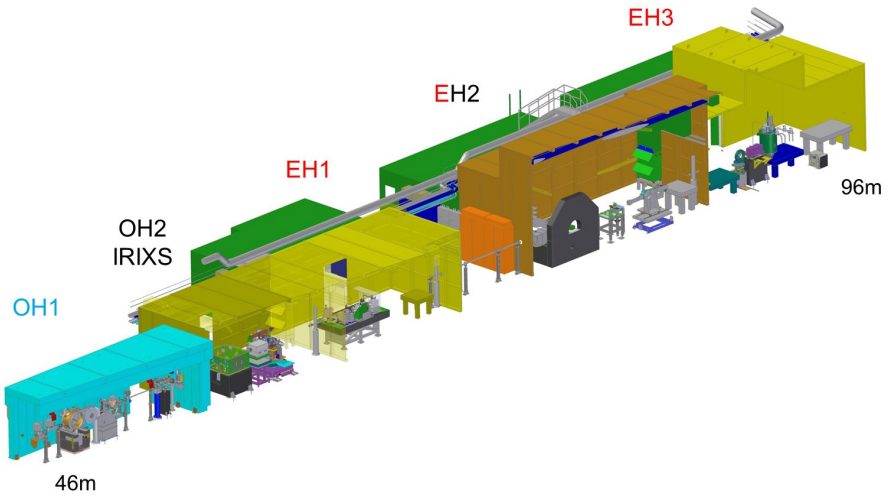

Figure 3.4: Scheme of Beamline P01[2].

atmosphere or in a helium environment. In EH1 a theta - two theta setup was installed for X-ray scattering experiments. EH2 hosted two inelastic X-ray scattering setups. The X-ray Raman setup and a resonant inelastic X-ray scattering setup. EH3 is currently used for nuclear inelastic scattering experiments.

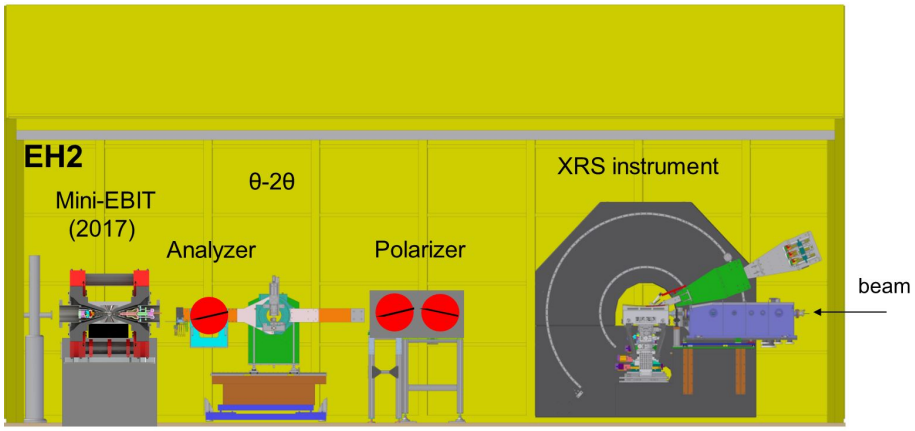

Figure 3.5: Scheme of the setups in EH2. XES, XANES/EXAFS and XRS experiments were performed at the XRS instrument location, using the XRS KB mirror system[2].

3.3.2 Undulators

The P01 undulator section is capable of hosting undulators with a total length of up to 20 m. During the operations, there were constantly two 5 m undulators installed. The undulators were optimized to provide a high photon flux near the Fe^{57} resonance line at 14.4 keV. Figure 3.6 shows the tuning curves of the old P01 undulators with the funda-

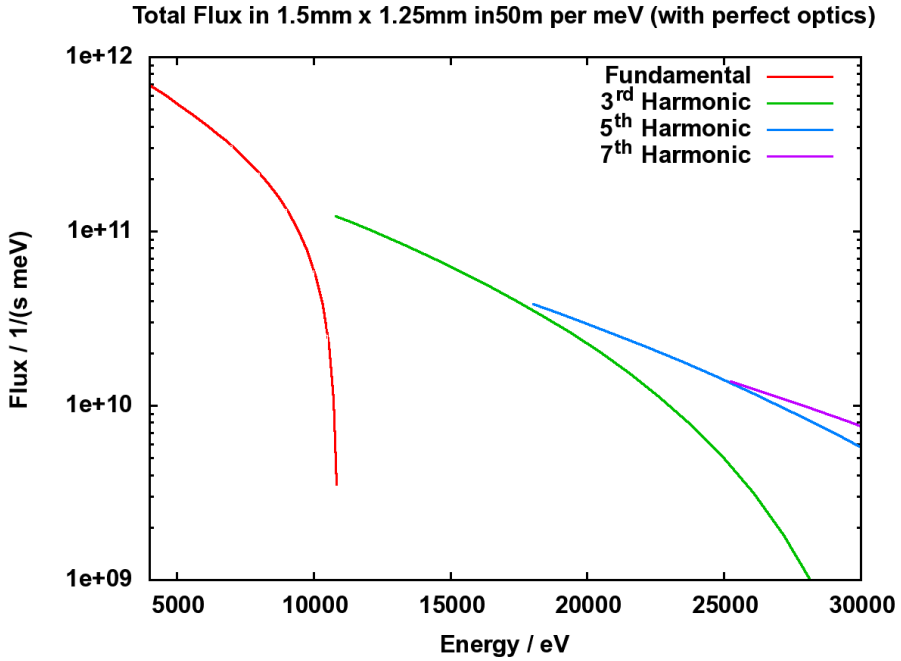

Figure 3.6: Theoretical undulator tuning curve of the old P01 undulators. Showing a gap between the first and third harmonic in the 11-12.5 keV range[2].

mental harmonic reaching energies up to 11 keV. Due to the minimum undulator gap of 12.7 mm, the minimal energy of the third harmonic started at 12.5 keV. As part of the P01 MPI partnership two new undulators were installed in 2017, allowing X-ray energies of down to 2.5 keV and closing the previous radiation gap in the 11-12.5 keV range[45].

3.3.3 Double Crystal Monochromator

The P01 monochromator is a nitrogen cooled double crystal monochromator (DCM) which can switch between two sets of Si(311) and Si(111) crystals. The maximum Bragg angle is 45°, while the minimum angle is close to 0°. The DCM is a so-called fixed exit monochromator. This means it keeps the outgoing X-ray beam at the same height, independent of the selected Bragg angle. This is achieved by two motors that move the second crystal parallel and perpendicular with regard to the surface of the first crystal. The recent beamline setup contains an additional asymmetrically cut Si(111) crystal, which allows steeper deflection angles, to also cover energies down to 2.8 keV (Ru L-edge).

3.3.4 X-ray Raman Setup

For non-resonant inelastic X-ray scattering (NIXS) experiments, a conically shaped analyzer vessel with twelve spherically bent Si(220) analyzer crystals, each with 4 inch diameter is used Figure 3.7. The inelastically scattered and monochromatized X-rays exit the vessel via a Kapton window and are collected near normal incidence with a 2D Medipix detector just in front of the vessel. The vessel can be rotated around the sample position to cover scattering angles 2θ from 0° up to 150°, allowing changes from nearly backscattering conditions to fully forward conditions[106]. An upstream KB-mirror system allows focussing of the photon beam down to 5x10 micron (VxH) on the sample. The setup is able to distinguish energy shifts within few meV[61].

Figure 3.7: XRS setup at P01. The conically shaped aluminum tank hosts 12 Si(220) analyzers for XRS experiments. Courtesy of Kai Schlage.

3.3.5 Resonant Inelastic X-ray Scattering

The original RIXS setup for solid samples at P01 consisted of a six-circle Huber[9]-diffractometer with a two meter long analyzer arm in the horizontal direction. For the optimal energy resolution, the vertical direction was chosen as the energy dispersive direction. The photons coming from the sample were again monochromatized by a diced analyzer and then collected in near backscattering geometry with a strip-detector (MYTHEN) with 50 μm x 8 mm pixel size. The setup utilized a specially developed diced

[9] https://www.xhuber.com/de/

quartz analyzer combined with a primary 4 bounce Si(553) high resolution monochromator (HRM), which was installed in OH2, to allow measurements at the copper K-Edge with an energy resolution of 25 meV[60].

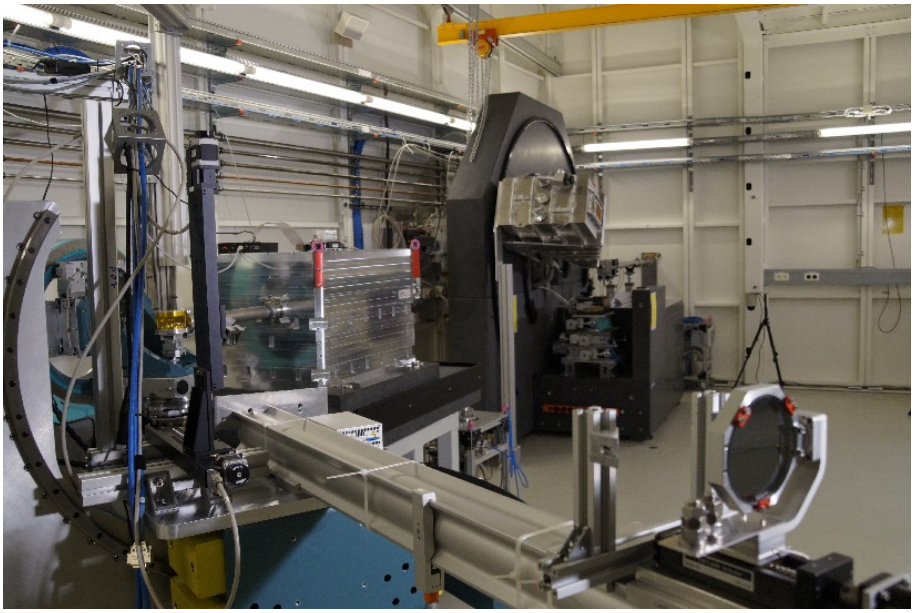

Figure 3.8: Six-circle RIXS-diffractometer at P01, with a Quartz analyzer and Mythen detector. Courtesy of Kai Schlage.

3.3.6 Beam Position Feedback

Due to instabilities in the vertical beam position at the sample position, a beam stability feedback, consisting of a beam position monitor and a piezo motor attached to the second DCM crystal was installed. The feedback automatically corrects undesired movements of the beam position on the sample in real-time. The beam drifts are caused mainly by two processes. First, the beam drifts during the stabilization of the DCM cooling temperature. Secondly, even though the DCM was fully calibrated, significant movements of the beam at the sample position (about 20 m downstream from the DCM), occurred during angular (energy) change, due to imperfect corrections of the perpendicular and parallel movements of the second DCM crystal. However, pump-probe experiments require an accuracy between the laser and X-ray spots on the sample of better than 10 μm, which was not possible before the installation of the feedback loop. The beam stabilization feedback uses a beam position monitor (BPM), installed in EH1, consisting of a 100 μm thin diamond plate, which is separated into four quadrants. The X-rays strike the diamond plate and generate a current on each quadrant, which are read out via four pico-amplifiers. The BPM is aligned in such a way, that the X-ray beam (aligned onto the sample) generates an equal current on each of the four quadrants, thus ensuring a

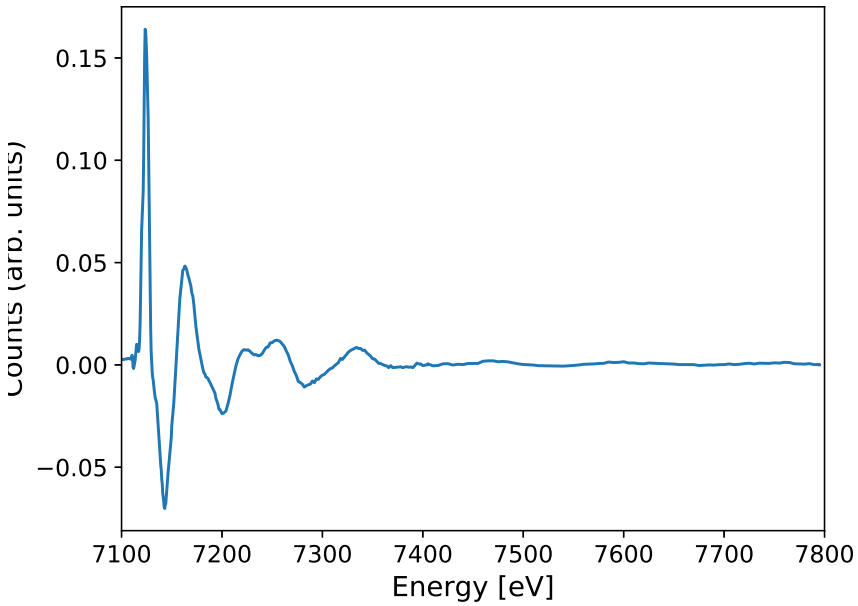

Figure 3.9: Transient EXAFS spectrum of 20 mM $[Fe(II)(bpy)_3]^{2+}$ in aqueous solution, after photoexcitation at 515 nm. Recorded at beamline P01, PETRA III. Its simultaneously measured ground state spectrum is shown in Figure 2.6.

central beam position. Any beam position change leads to a change in the ratio of currents on the quadrants. This information is used to tune the voltage of a piezo motor connected to the pitch of the second DCM crystal, to move the beam back to the center of the BPM. The piezo voltage can be operated with readout and corrections applied at more than 100 Hz (usually 40-60 Hz) and secures a correction of the beam path within much less than one second. Including this feedback greatly improved the stability. In combination with an optical laser setup to pump the sample, it allowed to record a full transient EXAFS spectrum of 20 mM $[Fe(II)(bpy)_3]^{2+}$ in aqueous solution in less than one hour (Figure 3.9).

3.3.7 Beamline Operation Software

Most devices, like detectors, motors etc. of the beamline are individually connected to a controller. These controllers are for example ZMX[10] servers or Beckhoff controls for motors or the operating PCs for detectors. The controllers and their communication protocols, hard- and software configurations are implemented as Tango[11] servers. Tango servers provide a standardized interface, which can be operated by a single user interface, thus facilitating the overall beamline control. In case of DESY the Tango servers are

[10] https://www.phytron.de/produkte/endstufen-controller/zmx/
[11] https://www.tango-controls.org/

organized via Sardana[12]. Finally, the user can operate the devices via Spock[13], which is a command-line user interface for iPython[14]. Spock offers a suite of predefined macros, for example, to move motors, to check their positions and limits, and to administer exposures with detectors synchronized to the motor movements. But also more complex macros, to conduct the measurements in a fully automated fashion are possible. This allows e.g. to set up measurement programs lasting several hours, while the user can monitor the experiment status and signal quality at any time during this sequence. During the measurements with Spock, the collected data is usually visualized via Spectra or Taurus[15]. The collected data is directly saved to the beamline file system, and synchronized to the core file system within a few minutes. Data stored to the core file system can be remotely accessed by the user after the beamtime is finished.

[12]https://www.sardana-controls.org/
[13]http://hasyweb.desy.de/services/computing/Spock/Spock.html
[14]https://ipython.org/
[15]https://www.taurus-scada.org/

4 A Multi-Crystal Von Hámos Spectrometer

Advanced X-ray spectroscopy experiments can require a high amount of photons or equivalent measurement time. This arises from low-concentration samples or detection of processes with low scattering cross section using for example X-ray Raman scattering or valence-to-core emission spectroscopy. Even at dedicated synchrotron radiation end stations like beamline P01 at PETRA III a complete measurement of a single sample can take up to days. The next-best option to reduce the required measurement time is - if the setup allows - to increase the number of collected photons coming from the sample by increasing the solid angle. A faster recording of spectra can also prevent the measurement on a degraded sample due to exposure to incident radiation and/or damaging ambient conditions. These reasons motivate using multi-crystal X-ray spectrometers. For this purpose, a 16-element von Hámos type spectrometer was constructed for the FXE end station. It was commissioned at PETRA III (P01), DELTA (BL9) as well as at the APS (07-IDD) where it was also used for several Experiments. In this chapter, we will first discuss the design strategy of the von Hámos geometry compared to the Johann geometry. A set of formulas that describe the energy distribution in the von Hámos geometry will be introduced. Next, the commissioning results are presented. The first experiment, where we used the von Hámos to track the bond distance and coordination changes of Ge-O as a function of pressure via valence-to-core X-ray emission spectroscopy, will also be shown in chapter 5.

4.1 Principle of X-ray Spectrometers

X-ray spectrometers are devices that can measure the energy of X-ray photons and record their intensity. For our applications these spectrometers consist of motorized crystals, using the Bragg condition to filter photons at certain energies followed by a position-sensitive detector. For a crystal, the photon energy E that is reflected towards the detector is given by Bragg's law via

$$E(\theta_B) = \frac{hc}{2d\sin(\theta_B)}, \tag{4.1}$$

with h as Planck's constant, c as the speed of light, d as the lattice spacing of the crystal's orientation and θ_B as the Bragg angle. Due to its wide use in the semiconductor industry, silicon is the most used analyzer material. Large crystals with high purity and quality are commercially available at a low cost. Figure 4.1 shows the Bragg angle for different crystal orientations of silicon as a function of the corresponding reflected energy. Other materials used as analyzer materials are for example germanium, quartz and sapphire.

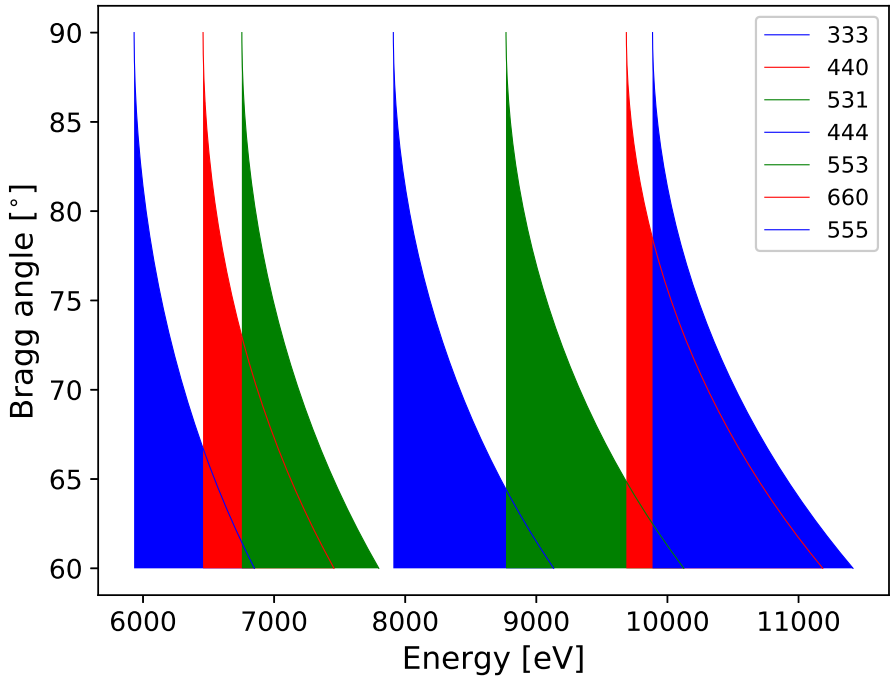

Figure 4.1: Energies available for silicon single crystal of given orientation.

Bragg's law applies to both spectrometer types, the basic von Hámos and the Johann spectrometer. Both are based on the principle that the photons are emitted from a small sample volume, also called source.
To focus the emitted X-rays of a certain energy onto the detector, a bending is applied to the crystals. For a spherically bent analyzer crystal all three components, source, analyzer and detector are to be aligned on the Rowland circle (Figure 4.2) with the source and the detector lying in the focal points of the crystal[32]. The diameter of the Rowland circle for this geometry describing the Johann spectrometer is equal to the curvature of the crystal. Figure 4.2 shows the principle of the Rowland circle for a crystal in Johann geometry.
The solid angle for X-ray photon collection is an important measure for comparing different spectrometer types (next to the energy resolution and the X-ray energy range coverage). The solid angle is given by the number of crystals n, the crystal surface area A and the distance to the source l. In addition, the X-rays see only a projection of the crystal, as it is tilted away from the source by 90° minus the Bragg angle. This results in the solid angle being

$$S = \frac{nA\,sin\theta_B}{l^2}. \tag{4.2}$$

The basic difference between von Hámos and Johann geometries is the bending of the crystals related to the axis that defines the Bragg angle. Resulting from these different curvature types, the procedure of recording the spectra differs. This will be described in

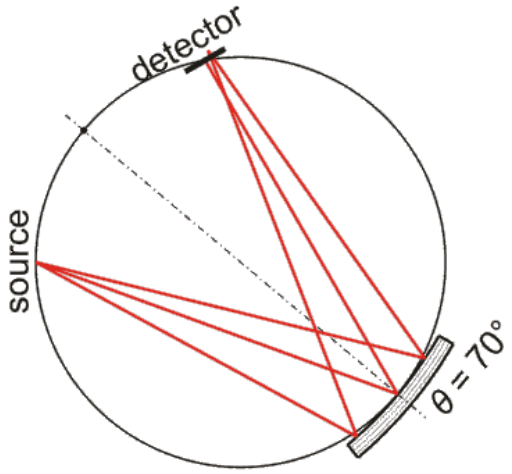

Figure 4.2: Cylindrically bent crystal in the Johann geometry, with the crystal being on the Rowland circle, focusing the X-rays coming from the source on the detector[62].

the following subsections.

4.1.1 Von Hámos Geometry

The von Hámos geometry has been proposed and described by L. von Hámos in 1933[108][109]. Multi-crystal von Hámos spectrometers are installed for example at SSRL & LCLS[10], PETRA III[57], ESRF[92] and European XFEL[38]. In this spectrometer geometry, the crystals are not bent along the axis that defines the Bragg angle. Figure 4.3 shows an analyzer crystal used in a von Hámos spectrometer, Figure 4.4 shows the principle of a von Hámos spectrometer. The photons emitted from the source

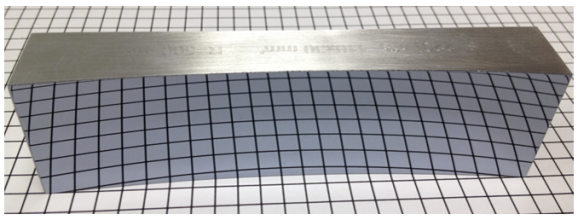

Figure 4.3: Cylindrically bent analyzer crystal with 50 cm bending radius used for a von Hámos spectrometer. The bending was achieved by gluing a Si(220) wafer on a 110 mm x 30 mm aluminum substrate.

strike the analyzer crystal and are reflected towards the detector if they fulfill the Bragg

condition. As the photons are emitted from a point source and the crystal is flat in one direction, the X-rays impinge on different regions of the crystal at different angles. Resulting in different Bragg conditions. Thus, the crystal becomes energy-dispersive. Using a position-sensitive detector, one can record an entire spectrum without moving

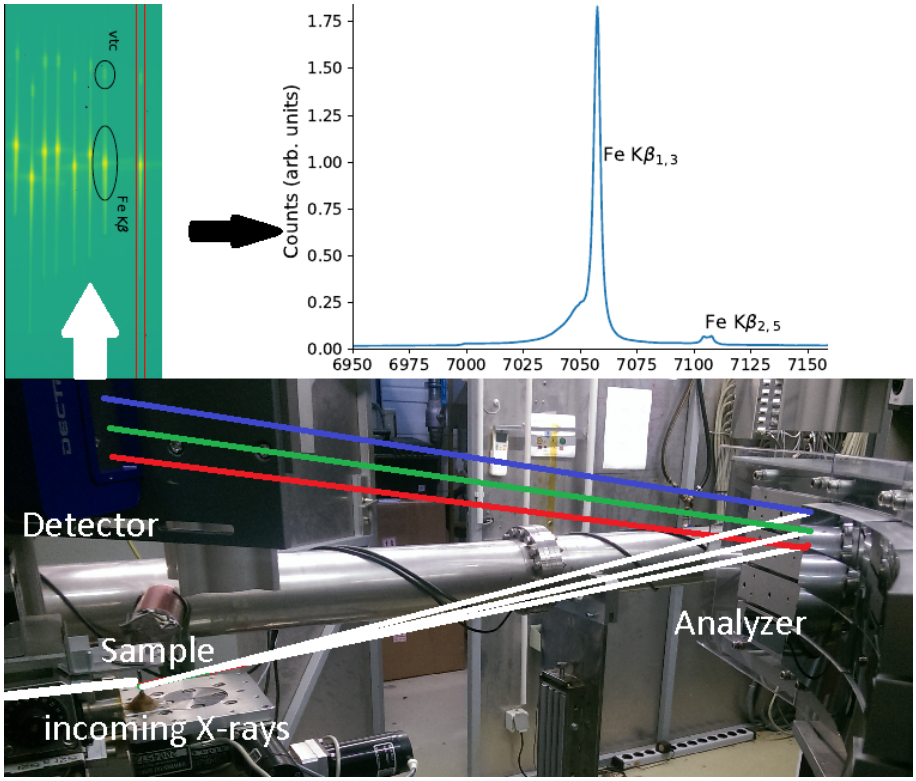

Figure 4.4: Principle of a von Hámos spectrometer. Photons with different energies emitted from the sample are filtered by the analyzer crystal under their corresponding Bragg angle before they hit the detector. The position where the photons hit the detector is determined by their energy. Applying an energy calibration one can extract the detector data to receive the final spectrum (here the Fe Kβ emission of $K_4Fe(CN)_6$).

the crystal. The solid angle of the spectrometer is distributed over the entire energy range defined by the Bragg condition (Figure 4.4), so it is more convenient to define the value solid angle per electron volt, in order to compare it to other spectrometers. The formula for the solid angle and the solid angle per eV is given in Equation 4.8 and Equation 4.9. Depending on the Bragg angle, only a small part of the energy range is relevant, leading to a smaller efficient solid angle. As the spectrum is collected without moving the setup, fluctuations in the X-ray flux affect every part of the spectrum equally, thus keeping the spectra shapes self-normalized to the incoming flux. This is one of the major advantages of the von Hámos geometry.

The one-dimensional bending of the crystals focuses the X-rays in the non-dispersive direction onto the detector. The bending of the crystal acts like a lens and the imaging property is preserved in this direction.

A von Hámos spectrometer can be used in two different geometries, the fixed exit (Figure 4.5) and the classic one (Figure 4.6). The von Hámos can be set up with the dispersive

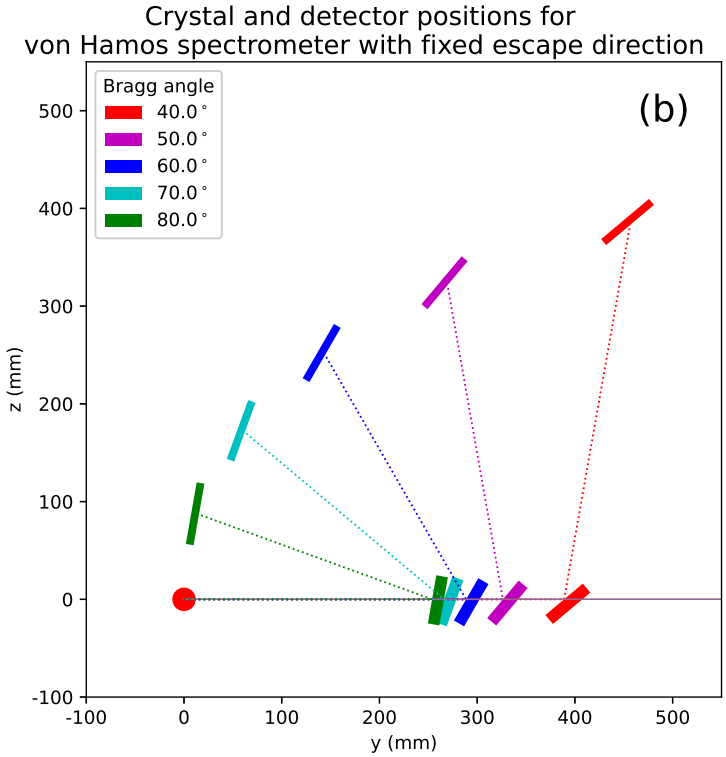

Figure 4.5: Translation of analyzer crystal and detector in a von Hámos spectrometer in fixed exit geometry at different Bragg-angles[63].

axis in the vertical or horizontal direction. In the vertical case, if the spectrometer sits at 90° to the incoming beam, the source size contribution to the energy resolution depends mainly on the focus of the X-ray beam. While if when going away from 90°, the X-ray beam path inside the sample can play a role. In the horizontal case and at 90° to the incoming beam, the source size contribution to the energy resolution is related to the beam path in the sample, not the X-ray focus. Each comes with certain advantages. The classic setup is easier to align due to both, spectrometer crystals and detector, being perpendicular to the ground. In order to change the energy only two linear motors are required. This makes the setup more favorable for mobile setups. The fixed exit geometry requires additional rotation stages to change the Bragg angle and the detector movement is no longer a linear motion. This geometry is more suitable for a permanent setup at a dedicated beamline. The fixed exit makes it easier to apply and optimize shielding for scattered X-rays and it can also decrease the source size, which can lead to an improved energy resolution (given that the source size has a notable effect on the energy resolution). The fixed exit is quite ideal to suppress undesired contribution from elastic scattering efficiently.

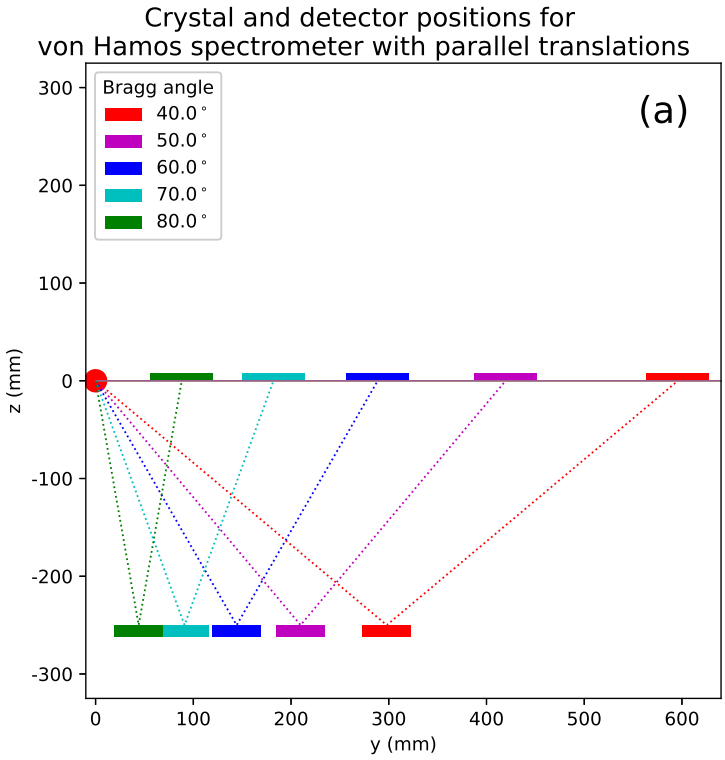

Figure 4.6: Translation of analyzer crystal and detector in a von Hámos spectrometer in classic geometry at different Bragg-angles[63].

4.1.2 Johann Geometry

The Johann geometry has been proposed and described by H.H. Johann in 1931[56]. To give a few examples, multi-crystal Johann spectrometers can be found at SSRL[101], PETRA III[106], ESRF[54][43] and European XFEL[38]. It is based on bent crystals, which preserve the same incident angle on the crystal from a point source. As such it acts as a monochromator with an energy bandwidth that is mainly determined by the chosen Bragg reflection and the Bragg angle of the spherically bent crystal. The bending is spherical and can be one- or two-dimensional. Figure 4.7 shows a typical spherical 2D bent analyzer crystal used in a Johann spectrometer. To focus the photons on the detector, the crystal needs to be placed on the Rowland circle (Figure 4.2). For photons emitted from a point source, the Bragg angle is approximately the same over the entire crystal. However, this approximation is only valid for angles close to 90°. For angles away from back reflection, there are deviations from the Bragg angle, depending on the position the X-rays impinge on the crystal. This leads to a deteriorated energy resolution[16]. In order to record an emission spectrum in Johann geometry, one has to move the analyzer crystals and the detector accordingly. For energy loss measurements, as is done e.g. in X-ray

[16]This is corrected in the Johansson geometry, where the crystal surface is additionally shaped to exactly match the surface of the Rowland circle.

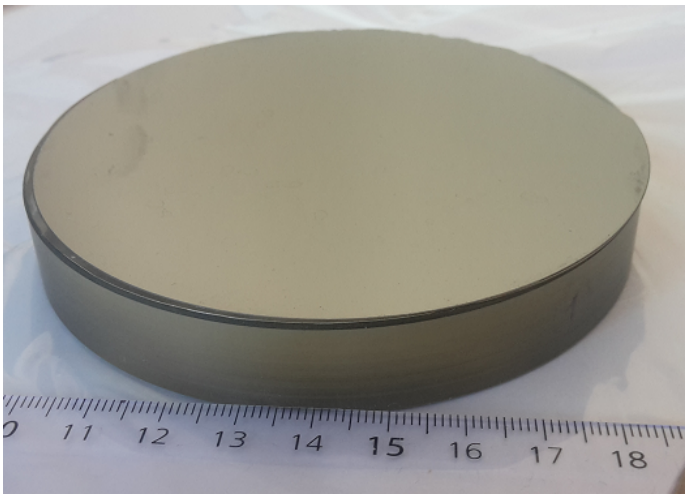

Figure 4.7: Spherical 2D bent Si(220) crystal with 1 m bending radius, made from a 4 inch silicon wafer.

Raman scattering, one can either move the crystals and detector or scan the incoming energy. Figure 4.8 shows the analyzers of the P01 multi-analyzer Johann spectrometer used

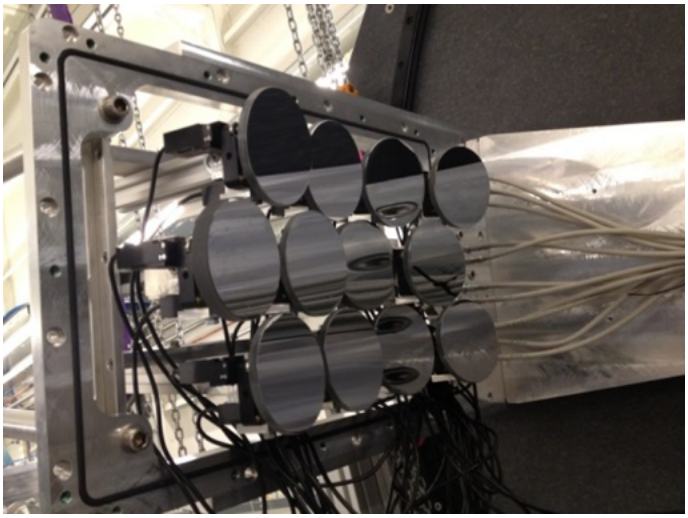

Figure 4.8: Johann spectrometer at beamline P01, PETRA III, used for X-ray Raman spectroscopy.

for X-ray Raman scattering. For RXES experiments both the incoming energy and the analyzer detector have to be scanned. As for each step of data taking the spectrometer has the same Bragg angle over all crystals, the combined solid angle of all crystals contributes to the recorded spectrum. Being aligned on the Rowland circle and the distance of a crystal to the source is $l = R\sin(\theta_B)$, the solid angle then becomes

$$S = \frac{nA}{R^2 \sin(\theta_B)}. \tag{4.3}$$

Due to the spectrum being taken point by point, one also needs to record the incoming photon flux to normalize the recorded spectra.

4.2 Von Hámos Theory

In this section, we will present a set of formulas that explain the von Hámos geometry and were used in the analysis of the collected data. First, we will explain the case of a perfectly aligned single crystal and then extend the formulas for a setup with multiple crystals at different angles. Finally, we will introduce the resulting total energy resolution of a von Hámos spectrometer and explain its contributions.

4.2.1 Single-Crystal Spectrometer

When using a single crystal, the crystal surface is ideally parallel to the detector surface. Our coordinate system is defined by the source being the origin and the detector surface placed on the y-axis, while the analyzer lies on the coordinates (R,y) with R being the crystal's bending radius of curvature and constant (Figure 4.9). In that case, the Bragg angle θ_B is defined by R and the distance between the source and the position of the signal on the detector y, by

$$\theta_B(R, y) = \arctan(\frac{2R}{y}). \tag{4.4}$$

The photon energy E, which is Bragg-reflected to the detector, depends on the vertical signal position on the detector y and the lattice spacing d of the crystal via

$$E(R, y, d) = \frac{hc}{2d \sin(\arctan(\frac{2R}{y}))}. \tag{4.5}$$

This formula can be used to determine the energy of the X-ray photons measured on the detector. With the derivative of E(R,y,d) with respect to y, we can display how the energy dispersion on each pixel of a position-sensitive detector changes (Figure 4.10). The energy interval (per pixel) has a significant influence on the final energy resolution of a von Hámos spectrometer, as described in subsection 4.2.3.
If the detector size is sufficiently large, the maximum and minimum energy covered by the crystal can be expressed by the crystal size along s the dispersive direction by either

$$E_{min}^{max}(R, y, d, s) = \frac{hc}{2d \sin(\arctan(\frac{2R}{y \pm s}))}, \tag{4.6}$$

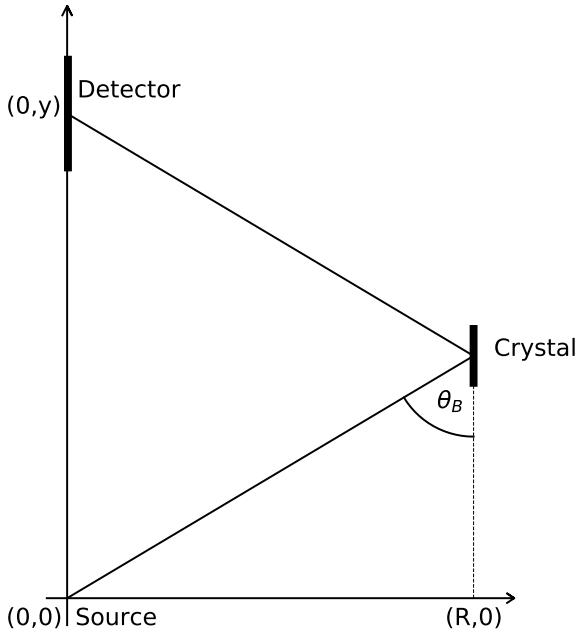

Figure 4.9: Sketch of a single-crystal von Hámos spectrometer, with the crystal parallel to the detector surface. The source lies in the center of our coordinate system. The detector surface is represented by the y-axis.

or

$$E_{min}^{max}(R, \theta_B, s) = \frac{hc}{2d \sin(\arctan(\frac{2R}{2R\,cotan(\theta_B) \pm s}))}. \tag{4.7}$$

The range between the maximum and minimum energy detected by the crystal can then be used to calculate an approximation for the detected solid angle per electron volt. First we calculate the solid angle of the crystal. In the von Hámos geometry, the distance of the crystal to the source is given by $l = \frac{R}{\sin(\theta_B)}$. This results in the solid angle for an n-element spectrometer

$$S(R, \theta_B, A) = \frac{nA\, sin^3(\theta_B)}{R^2}, \tag{4.8}$$

with A being the surface area of the analyzer crystal. In a first approximation, the solid angle per energy is then given by dividing the solid angle by the energy range covered by the crystal:

$$S_{1\,eV} = \frac{S(R, \theta_B, A)}{E_{min}^{max}(R, \theta_B, s)}. \tag{4.9}$$

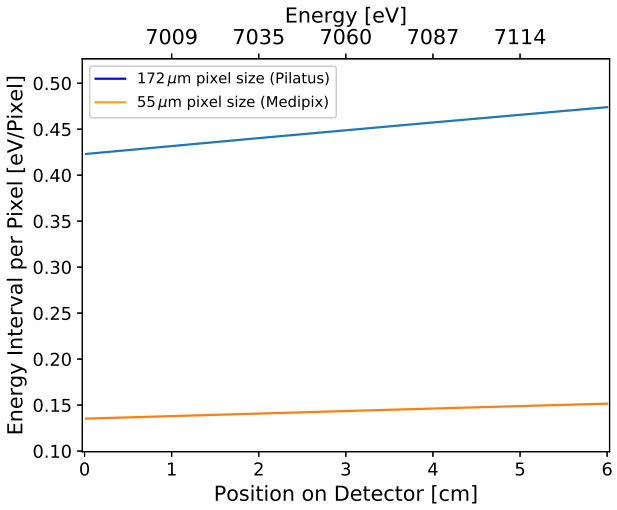

Figure 4.10: Calculated energy interval per pixel on a position-sensitive detector with 172 μm (blue) and 55 μm (yellow) pixel size, similar to the detectors used in our experiments. For the calculation, we used a Si(220) crystal with 50 cm curvature and 3 cm height, aligned around the iron Kβ emission, using the (440) reflection.

As a result, the solid angle per energy is maximized close to backscattering and decreases significantly at small Bragg angles.
The position where a photon with a certain energy strikes the detector is given by

$$y(E, R, d) = \frac{2R}{\tan(\arcsin(\frac{hc}{2Ed}))}. \tag{4.10}$$

Using this relationship we show the nonlinear dispersion of reflected photon energies onto different regions of the detector in Figure 4.11, where we calculated the energy related to position on the detector for the Si(440) reflection as an example. The crystal has a curvature of R = 50 cm. In addition, we show the energy range that is covered by a Si(440) crystal similar to the ones used in our setup to measure iron Kβ emission. In addition, by using Equation 4.5 for various energy ranges of the Si(440) reflex, we show that even in a small range on the detector a linear fit is not sufficient to fit the dispersion (Figure 4.12). As the root function-like shape of the dispersion already suggested, a second-order polynomial fit works well. For this example the second-order fit is always within 10 meV difference over the whole analyzer crystals energy window.

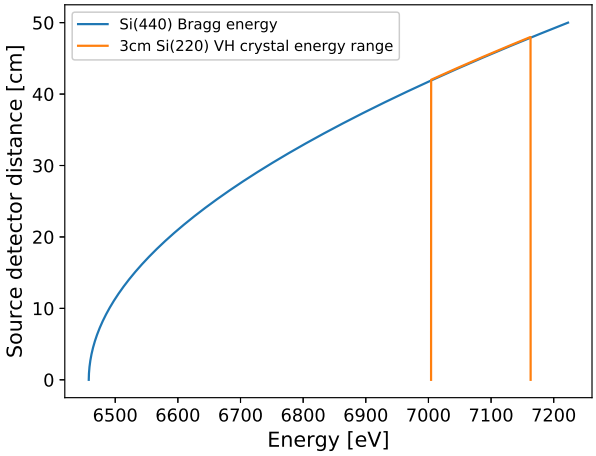

Figure 4.11: Relationship between photon energy and the vertical distance to the source (where it is recorded by the detector, see Figure 4.9 for the utilized setup geometry). This is shown for a Si(440) crystal (with 50 cm curvature). The orange line indicates the range accessible by such a crystal with 3 cm height and aligned around the iron Kβ emission energy.

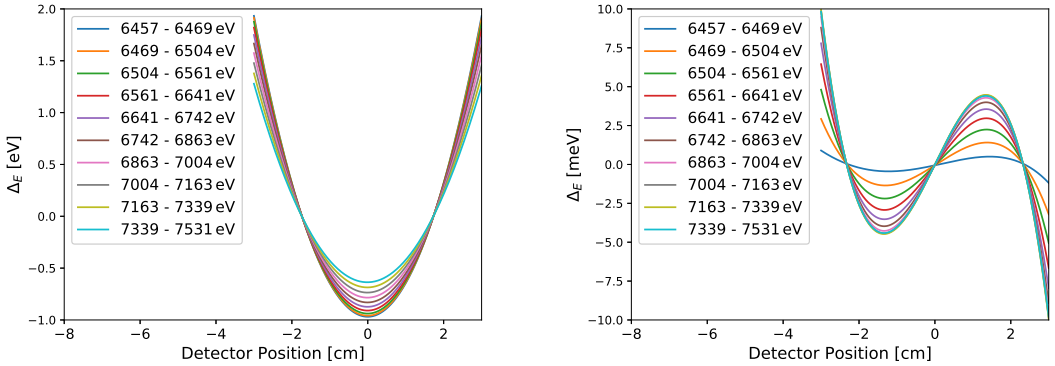

Figure 4.12: For the example of Si(220), we calculated the dispersion curves for different energy ranges that are achieved by using 3 cm high analyzer crystals, using Equation 4.5. We show the difference after subtracting a linear fit (left figure) and a second-order polynomial fit (right figure).

4.2.2 Multi-Crystal Spectrometer

When using a setup that employs more than one crystal in the dispersive direction, one has to tilt each crystal by a certain angle in order to access the same energy range with all crystals. When tilting these crystals, their surfaces are not parallel to the detector surface anymore, as shown in Figure 4.13. We keep the detector surface on the y-axis in our coordinate system, so we have to redefine the crystal surface. Therefore, we introduce the tilting angle α, which indicates how much the crystal has been tilted from the parallel case, and a new distance from the crystal to the source R', that defines the crystal surface.

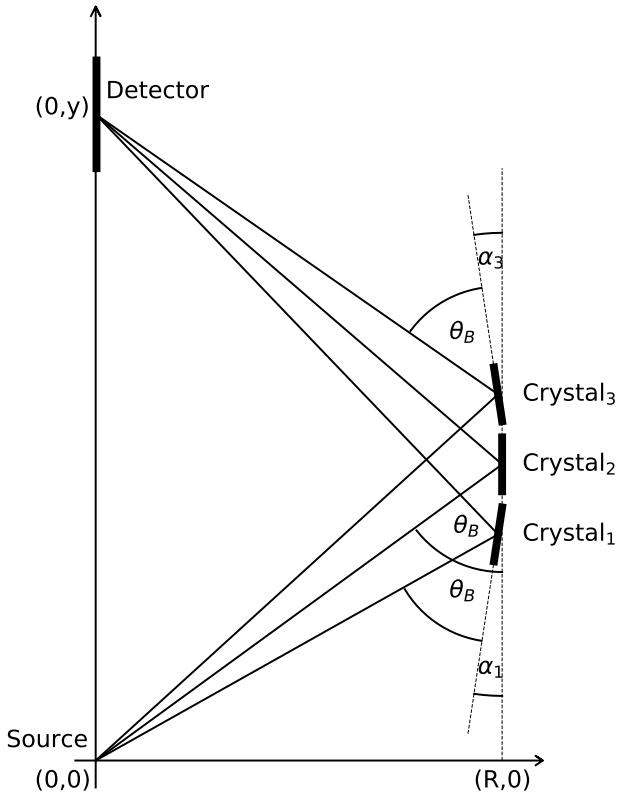

Figure 4.13: Several von Hámos crystals aligned to the detector with the same Bragg angle, resulting in a tilted alignment for each of them.

Figure 4.14 illustrates how R' and α are defined. As we want R' to be independent of which spot we hit on the crystal, we chose the shortest distance between the straight line that defines the crystal surface and the origin for R'. One can approximate the angle α with the equation

$$\alpha = \arctan(\frac{2R}{y}) - \arctan(\frac{2R}{y+2u}), \tag{4.11}$$

where y is the detector height calculated for a specific energy with the single-crystal formula and u indicates how much the center of the crystal has been shifted compared to a parallel aligned crystal, which center is exactly half the detector height. This approximation is accurate within 0.1° for a spectrometer with parameters like the one presented in this thesis.

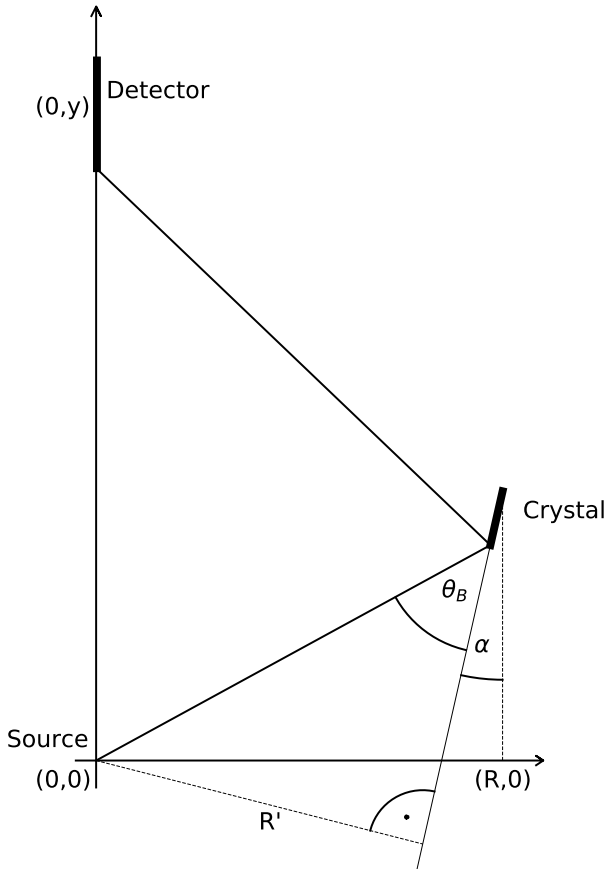

Figure 4.14: Sketch to illustrate the definition of R' and α, we need these variables, since the crystal surface is no longer defined by (R,y/2). By definition they are constant for each single crystal and thus can be used as fitting parameters.

R' can now be calculated via

$$R' = \frac{(\tan(\theta_B) - \tan(\alpha))\, y \cos(\alpha)}{2}. \tag{4.12}$$

For the position of the signal on our detector y, we then obtain the equation

$$y(R', \theta_B, \alpha) = \frac{2R' \cos(\theta_B)}{\sin(\theta_B - \alpha)}, \tag{4.13}$$

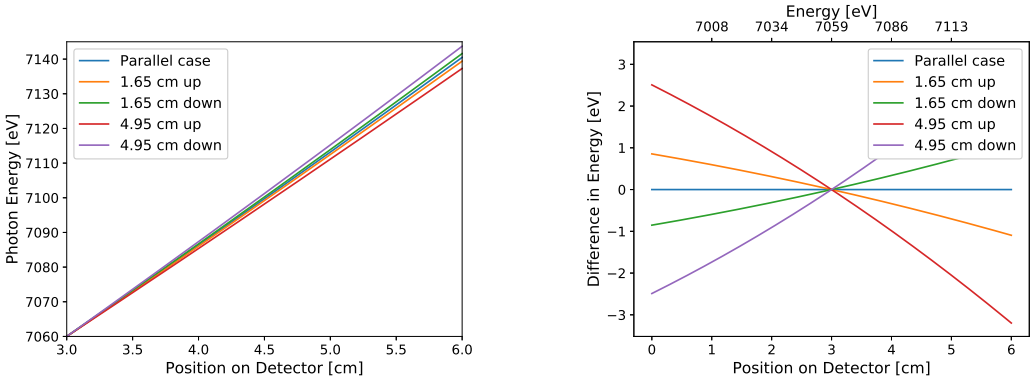

Figure 4.15: Calculated relation of the photon signal position on the detector and the photon energy for five Si(440) crystals with 3 cm size in dispersive direction. One crystal is calculated without tilt. The other four crystals are aligned as in our von Hámos setup. The crystals are overlapped at 7060 eV. The left figure shows the absolute energy dispersion, the right figure the difference with respect to the parallel aligned crystal.

after introducing R' and α.
This equation can be rearranged to a formula for the Bragg angle.

$$\theta_B(R', y, \alpha) = \arctan\left(\frac{2R'}{y\cos(\alpha)} + \tan(\alpha)\right). \tag{4.14}$$

With the Bragg angle, we obtain the recorded energy E on the detector

$$E(R', y, \alpha, d) = \frac{hc}{2d\sin\left(\arctan\left(\frac{2R'}{y\cos(\alpha)} + \tan(\alpha)\right)\right)}. \tag{4.15}$$

As d is usually defined by the crystal plane, we have now expressed the photon energy in dependence on the signal position on the detector, and both values, R' and α which are constant for each analyzer crystal. This is required for the energy calibration, in order to determine the signal positions on the detector for different energies and use these values to find the optimized values for R' and α via least squares approximation procedure. With these optimized values we then obtain the function E(y). In the case of α = 0 (the crystal surface being parallel to the detector surface), we yield the single-crystal case solution. As each crystal has a different tilt, each crystal has its individual relation between the photon energy and its recorded position on the detector. Still, for each crystal, one can find the conditions for α and R' yielding the same single energy imaged onto the same signal position on the detector. Yet, when moving away from this position, the photons coming from each crystal to the same single spot on the detector start to have different energies. For our calculated examples we chose the iron K$\beta_{1,3}$ peak (7060 eV) as the energy, to which all crystals image these photons onto the same spot on the detector. From the calculations, we see that crystals can be overlapped within a certain energy range. However, this has to be evaluated for each experiment, or better: for each chosen central

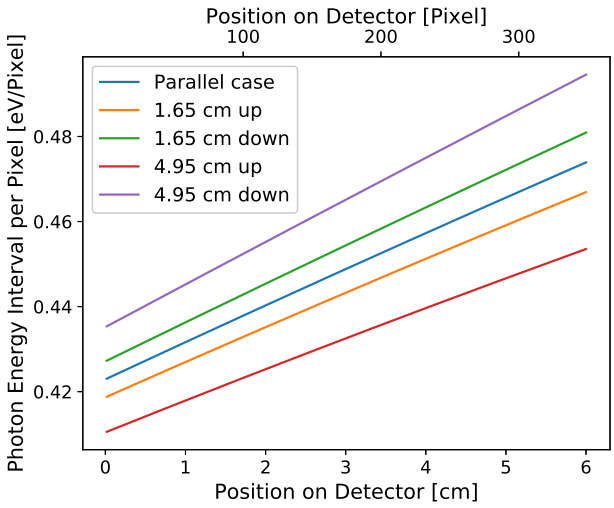

Figure 4.16: Calculated energy per pixel on a position-sensitive detector with 172 μm pixel size for four Si(440) crystals as in our setup and the parallel case.

energy x, as it affects the convoluted energy resolution.
In Figure 4.15 we calculated the photon energy dispersion on the detector for five Si(440) crystals. One of the crystals is set to the parallel case without tilt, the other four are arranged to image the K$\beta_{1,3}$ peak onto the same detector position. For this arrangement, we now plot the energy interval per pixel on the position-sensitive detector (Figure 4.16). As we introduced in the previous subsection for the parallel case and Equation 4.5, we show that Equation 4.15 can be approximated by a second-order polynomial fit. This is done for the four different crystal heights in the von Hámos spectrometer and for the example of iron Kβ emission recorded with (440) reflex of Si(220) crystals overlapped at 7060 eV (Figure 4.17). While the deviation is larger for some of the crystals compared to the parallel case, it is still below 15 eV when fitting the whole 3 cm range of an analyzer crystal and therefore suggests that a second-order polynomial is sufficient to fit dispersion curves during our measurements.

4.2.3 Energy Resolution

The energy resolution is defined by several factors. The geometric part of the energy resolution ΔE_G sums up the contributions that arise from deviations from the Bragg angle. The contributions to $\Delta E_{G,y}$ are the effective source size parallel to the sample-detector direction S_y and the detector pixel size D as well as the distance between analyzer and source is given for the single-crystal case by:

$$\Delta E_{G,y} = -\frac{ERS_y}{\tan(\theta_B)(R^2 + (\frac{y}{2})^2)}, \tag{4.16}$$

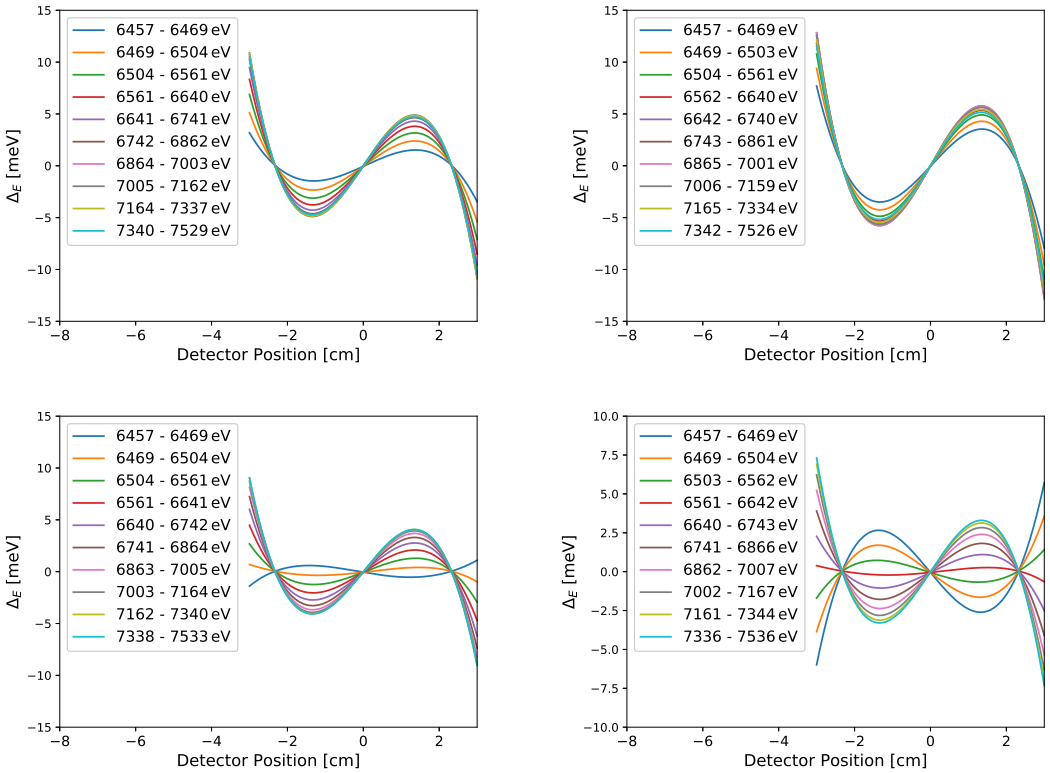

Figure 4.17: For the example of iron emission recorded with four Si(220) at different heights, overlapped to the same pixel at 7060 eV, we calculated the dispersion curves for different energy ranges that are achieved by using 3 cm high analyzer crystals, using Equation 4.15. We show the difference after subtracting a second-order polynomial fit for each crystal (left upper figure is the difference obtained for the top analyzer, right upper figure the next highest crystal, bottom left shows the third and bottom right the lowest crystal in our setup).

with R the crystal's bending radius, the crystal's vertical coordinate $\frac{y}{2}$ results from the crystal sitting at half the detector height y[92]. The contributions to $\Delta E_{G,x}$ are the effective source size perpendicular to the sample-detector direction S_x as well as the distance between analyzer and source, it is given by;

$$\Delta E_{G,x} = -\frac{E\frac{y}{2}S_x}{\tan(\theta_B)(R^2 + (\frac{y}{2})^2)}, \tag{4.17}$$

with c_y the vertical crystal coordinate, with regards to the source[92]. Then ΔE_G can be approximated by:

$$\Delta E_G = \sqrt[2]{\Delta E_{G,x}^2 + \Delta E_{G,y}^2}. \tag{4.18}$$

In addition, the contribution by the intrinsic energy resolution is defined by two contributions: The Darwin width ΔE_D, which can be calculated by the dynamical diffraction theory of perfect crystals and the deformed lattice spacing ΔE_B, which is caused by the bending of the crystal. As a last contribution, ΔE_C is the part of the energy resolution

which takes care of the deficiencies of the crystal alignment and manufacturing quality. As all contributions are assumed to not correlate with each other, the final energy resolution ΔE_{tot} is given by:

$$\Delta E_{tot} = \sqrt[2]{\Delta E_G^2 + \Delta E_D^2 + \Delta E_B^2 + \Delta E_C^2}. \tag{4.19}$$

4.3 Alignment, Calibration and Data Treatment

In this section, we describe all the procedures that are necessary to receive the final spectra measured with the von Hámos spectrometer. We do this for the example of a von Hámos spectrometer (shown in Figure 4.18) described later in section 4.4 in the classic geometry, with the dispersive axis perpendicular to the incoming beam using a Pilatus 2D detector. We describe the detector images to provide a basic understanding of the signals seen on the detector. To perform measurements using a von Hámos we start with the alignment of the whole spectrometer and continue with the alignment of the individual crystals for two different crystal arrangements, the overlapped signal and the separated signal setup. We proceed with elastic line measurements used for calibration, show the procedure of energy calibration in detail and carry on with the extraction of data for the case of iron Kβ emission of $K_4Fe(CN)_6$ measured with eight Si(440) crystals in separated signal setup. We apply the energy calibration to obtain the emission spectra as a function of energy and use these spectra to demonstrate methods for background subtraction and receive the final background corrected spectrum.

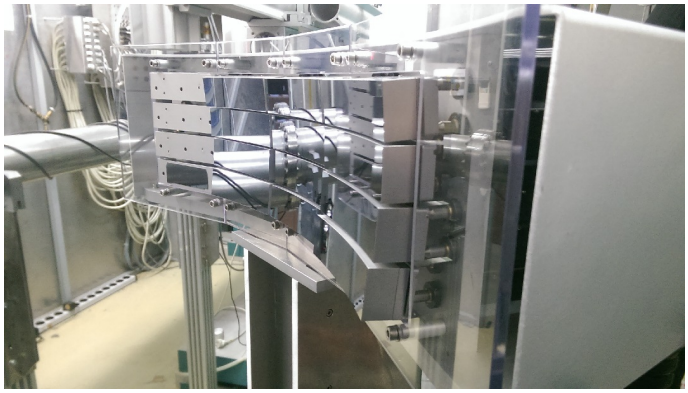

Figure 4.18: Von Hámos spectrometer of FXE set up during the first commissioning measurements using X-rays in March 2015 at the BL9 hutch at DELTA. Mounted with 12 analyzer crystals, 8xSi(220) attached to the magnetic mounts of the first two columns from the right, 4x Si(531) in the third column and no crystals attached in the leftmost column.

4.3.1 How to Interpret Detector Images

Understanding the signal displayed on the detector is vital to adjust the spectrometer and processing the collected data. Figure 4.19 shows an elastic line measurement from six Si(531) crystals, collected with the Pilatus 300k detector using an iron foil as scatterer, at 7060 eV incoming photon energy. There are different effects one can see on the detector image. In our setup, the energy dispersive direction is displayed on the horizontal axis of

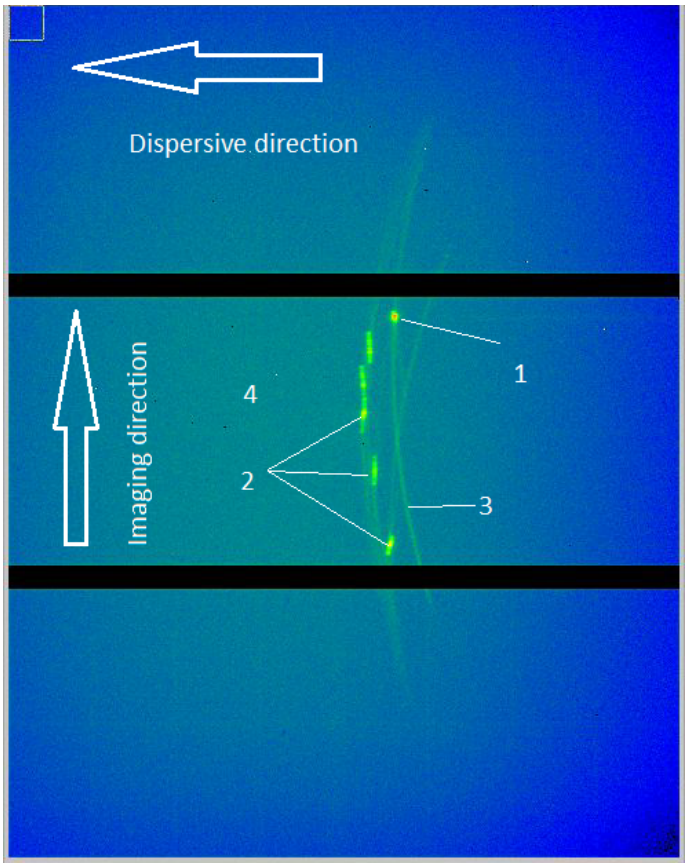

Figure 4.19: Single detector image produced by a Pilatus 300k with six Si(531) analyzer crystals collecting the signal of a thin iron foil, put in the beam to produce elastic scattering. The incoming photon energy was set to 7060 eV. The dispersive axis was in the vertical direction when measured. Signals 1-4 are discussed in the text.

the detector. The vertical direction is the imaging direction and the crystals function like a lens and give spatial information about the sample and sample environment. Signal 1 originates from elastically scattered photons by the sample that are reflected under Bragg condition by one analyzer crystal, already optimally focussed, thus delivering a narrow peak in the imaging direction. Signals 2 stem from misaligned analyzer crystals, they also originate from elastic scattering by the sample, but due to the crystals not yet optimized focussing they are broadened in the imaging direction. Signal 3 is elastic scatter by the direct beam in air, before and after the sample. In this case, it is collected via the crystal that also produced the sharp peak introduced as signal 1. Using the imaging property of the crystals, one observes that it is indeed spatially separated from the sample signal. One can observe several traces of air scattering in the image, each coming from a different analyzer crystal. Signal 4 shows a blurred region over the entire detector, originating from spuriously scattered X-rays arriving on the detector which do not pass over any analyzer crystal. This additional scattered signal can be suppressed significantly by reducing the number of scattered photons by using a helium balloon between spectrometer and the

sample and detector as well as good shielding. Good shielding usually blocks the direct path between the detector and the sample and other sources of scattering, e.g. windows of the beam pipe, the beam stopper and even the direct beam scattering in air. Lead tape, aluminum and thick plastic plates can be used to construct apertures that help to reduce the field of view of the detector.

4.3.2 Alignment Procedure

The first step of the alignment is to set the center of the detector chip to the height calculated for the energy of interest. The active area of the detector should be large enough to collect the whole spectrum dispersed by the crystal at once and the pixel size small enough to provide sufficient energy resolution. After, the spectrometer is put to a height so that the crystal analyzer array sits at about half the detector height. In addition, the spectrometer must maintain a distance that corresponds to the radius of curvature of the crystals from the sample-detector-axis. This step is crucial to be able to achieve a good focus with all crystals within their motor movement range. We use the optical reflectivity of silicon, which allows to image a bright optical laser spot focused on the sample position to the detector. With symmetrically cut X-ray crystals, the optical path is identical to the path of the X-ray photons. This way, we optically pre-align the spectrometer crystals, to assure that the crystals focus the emitted X-ray photons onto the detector surface. Af-

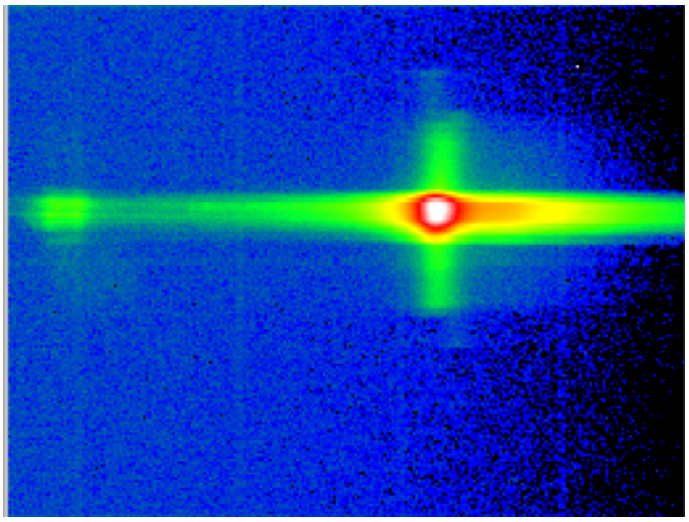

Figure 4.20: Overlapped signals of eight Si(440) analyzer crystals on a Pilatus 300k detector, used to record Kβ and vtc emission from 0.5 M $K_4Fe(CN)_6$ in aqueous solution with a Pilatus 300k detector. The crystals were aligned to reflect 7060 eV photons under Bragg condition to the same pixel.

ter this alignment step, we proceed with alignment by X-rays using an elastic scatterer or a sample providing an emission signal. In the ideal case, all reflexes of the crystals can

already be found on the detector. If not, either the crystal is tilted too much along the imaging direction, so the signal misses the detector active area, or it is tilted along the dispersive axis, resulting in the Bragg condition not being fulfilled for that energy. After finding all the reflexes, we continue to focus the crystals by moving them towards or away from the sample-detector-axis. Once all crystals are optimally focussed, we check the crystals' tilt along the dispersive axis to assure, that all energies we are interested in can match the Bragg condition on the crystal and get reflected towards the detector. The X-ray signals coming from each crystal can be either overlapped (Figure 4.20) to maximize the signal-to-noise ratio or separated to different detector stripes (Figure 4.21), which optimizes the overall energy resolution. The advantages and disadvantages of both setups are described in the next paragraph. For measurements with separated crystals, the reflexes are moved to different, well-separated areas along the imaging direction and the spectrometer is ready for measurements. For overlapped crystals, we choose a pixel on the detector where we want all the crystals to overlap with the same energy. We set the incoming X-ray energy accordingly and use elastic scattering for the overlapping. We proceed by moving the first crystal to the desired pixel position along the imaging direction. Then we move the crystal towards or away from the sample-detector-axis to move the signal along the dispersive direction. Once we positioned the elastic peak onto the pixel, we double-check that the crystal is still tilted correctly to be able to record the full energy range. We save the motor positions and move the signal slightly away to proceed with the next crystal. Once all crystals are aligned, we move the crystals to the saved motor position and finish the alignment. Overlapping signals is mandatory when

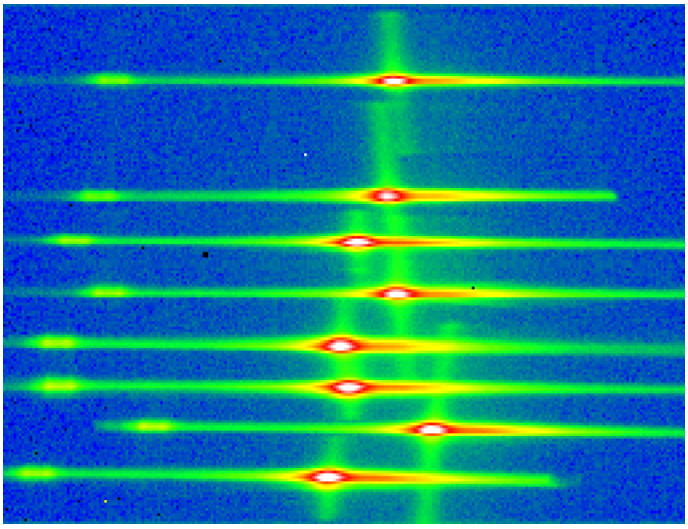

Figure 4.21: Eight separate Si(440) crystal signals, used to record iron Kβ and vtc emission from 0.5 M $K_4Fe(CN)_6$ in aqueous solution with a Pilatus 300k detector.

measuring with a 1D detector, but also on a 2D detector the overlapping can be useful: Overlapping the signal from different crystals onto one single stripe has the advantage of collecting the signal over a smaller area on the detector, thus optimizing the signal-to-

noise ratio of the collected signals. The overlapped signals can lead to a worse energy resolution because each crystal has a different dispersion, as described previously. When the signals are separated, there can be interferences between the signals coming from different analyzer crystals, as can be seen in Figure 4.21, for the example of Fe K$\beta_{1,3}$ and vtc emission from $K_4Fe(CN)_6$ in aqueous solution. We appoint the green lines in vertical direction to the imperfect bending of each crystal, especially at the edges of each crystal. Interferences that affect the ROI (region of interest) of another crystal should be avoided at all costs. Masking the edges of the crystals can help reduce these interferences. Once the alignment is done we can proceed with the energy calibration.

4.3.3 Energy Calibration

The energy calibration measurements are necessary in order to obtain a relation between the signal distributed on the detector and the energy of the collected photons. To do so, the incoming energy is set to several energies using the monochromator of the respective beamline within the Bragg acceptance range of the aligned crystals. The elastically scattered photons create a single peak at the detector position that corresponds to the selected incident energy. This yields the so called quasi-elastic line and its width already gives an indication about the energy resolution, if not deteriorated by the sample thickness. Figure 4.22 shows an elastic line measurement of a 5 μm thick iron foil using eight Si(440) crystals at 7060 eV incoming energy. The elastic lines are usually fitted by a Gaussian to estimate each peak position for each crystal along with its width. By measuring the quasi-elastic lines for different incident X-ray energies, one receives a set of data points connecting energies and detector positions, yielding the calibration curve for each crystal. This is shown in Figure 4.23, where the detector images of eight elastic lines, collected with eight Si(440) crystals have been overlayed. For each crystal, we define a ROI which is chosen as narrow as possible in the imaging direction (for us the y-axis of the detector) that just the entire signal of the crystal is contained. Using small ROIs helps reduce the background of the collected spectra. Also shown are the ROIs chosen for each of the eight analyzer crystals.

For each ROI we now look at the different images taken at different energies. For each image, we sum up the data along the y-axis of the ROI to find one peak at a certain position along the x-axis that can be fitted with the Gaussian function. By doing so, we receive a set of detector positions and corresponding energies for each crystal. The extracted signals for one crystal at eight different energies and the fit applied to it are displayed in Figure 4.23.

This set of detector positions connected to individual incoming energies is now used to

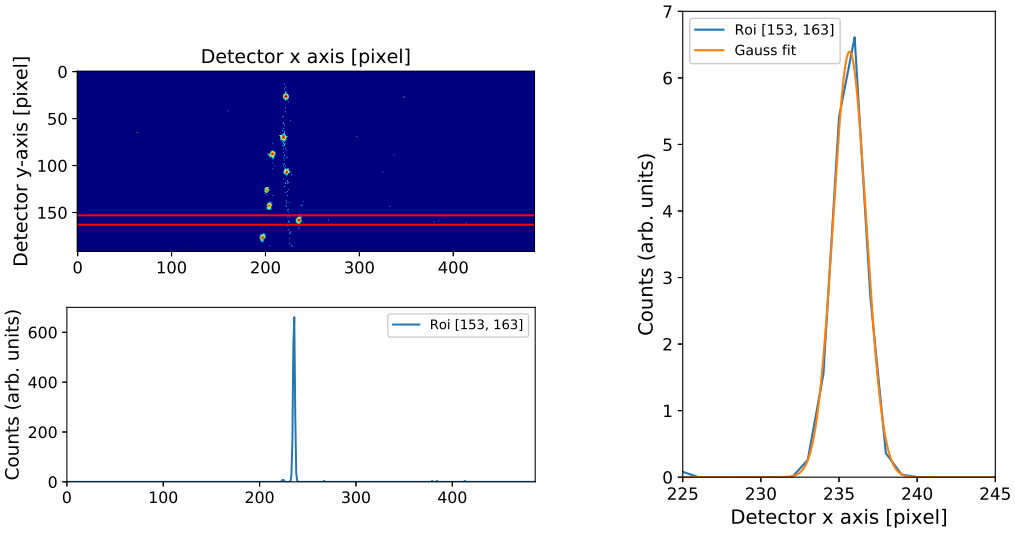

Figure 4.22: The left top figure shows an elastic line measurement of eight Si(440) crystals using an iron foil as scatterer. The incoming energy was set to 7060 eV and the data was collected with a Pilatus 300k detector (we just show part of the detector image), the red lines indicate the ROI set for the crystal we will use to demonstrate the elastic line extraction. Left bottom figure shows the collected signal summed up along the y-axis of the ROI. Right figure shows a zoom into the extracted elastic line and a Gaussian fit (orange) applied to it.

generate the calibration curve for each ROI via a second-order polynomial. It is a good practice to first check the elastic lines for aberrations that can influence the final energy resolution or spoil the energy calibration and unexpected intensity changes, which indicate that the crystals' field of view towards the sample or detector is partially blocked.

4.3.4 Data Extraction

For our measurements we used 2D detectors, the data treatment on a 1D detector is similar but involves usually fewer steps. As described before, we set up our experiment in such a way, that the dispersive axis is aligned along the y-axis of the detector.
To make sure we do not alter our experimental data, the detector images are constantly written to the data acquisition system. For evaluation, the files are read to the RAM and the output is saved in separate files. A set of python[17] scripts has been developed to automate the data extraction. We will demonstrate the procedure for data extraction for the example of 0.5 M $K_4Fe(CN)_6$ in aqueous solution running in a 300 μm flat liquid jet, using eight Si(440) analyzer crystals to record the nonresonant iron Kβ emission sig-

[17] https://www.python.org/

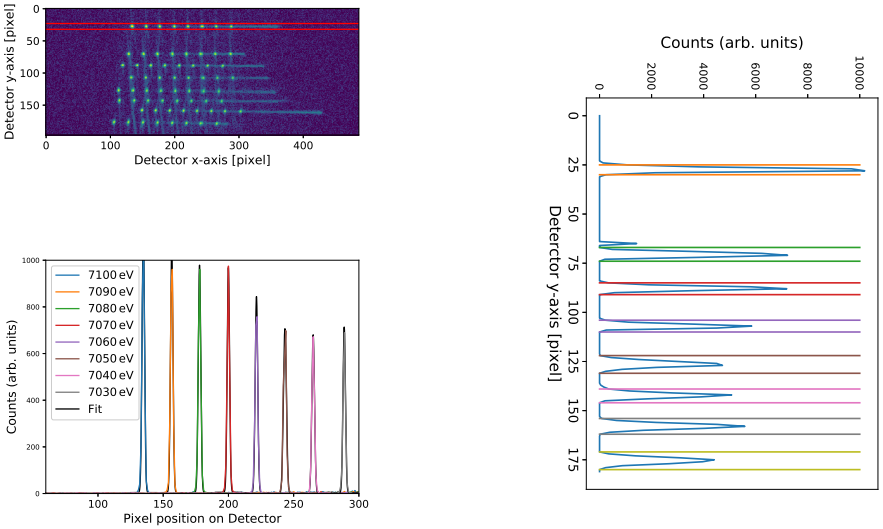

Figure 4.23: Upper left: Summed up measurement of eight elastic line measurements of eight Si(440) crystals using iron foil as scatterer. The energy was measured from 7030 to 7100 eV in 10 eV steps. Marked in red is a ROI we will use to demonstrate further extraction of the elastic lines and the spectrometer energy calibration. Upper right: Combined elastic image shown in Figure 4.23 has been summed up along the x-axis to identify the pixel rows that contain the elastic signal coming from the crystals. Areas with low counts have been set to zero, to allow a fitting algorithm to define a ROI for each crystal. The vertical lines have been added to indicate these ROIs. Lower left: Extracted elastic signal for one crystal, summed up along the y-axis of the ROI shown in Figure 4.23. The elastic lines were taken at eight different energies, 7030 to 7100 eV. At each energy one detector image was taken, the figure shows all eight elastic lines combined.

nal at 7500 eV incoming energy with a Pilatus 300k detector. The first step in the data analysis is to define the ROI for each analyzer crystal (or group of overlapped analyzer crystals) on the detector (Figure 4.25). For each ROI that has been defined, we sum up the data along the non-dispersive axis on the detector, in order to gather the signal, in this example the Fe Kβ emission. This generates spectra as a function of pixels along the dispersive axis. With the previously introduced energy calibration, we can generate the X-ray emission spectrum as a function of the energy. Figure 4.26 shows these steps toward energy-calibrated spectra. As a final step, we carry on with subtracting the background.

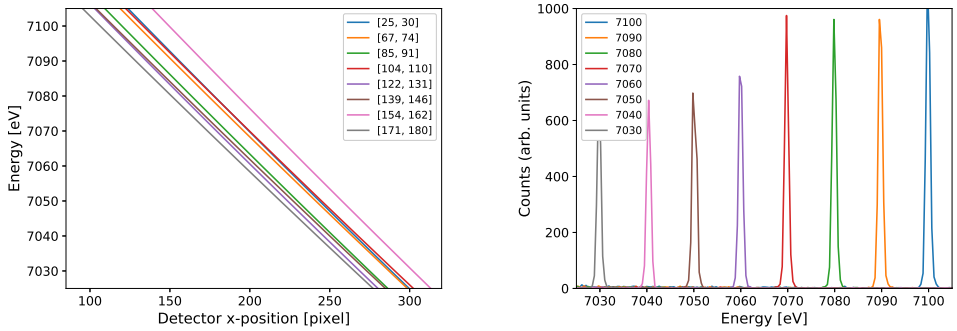

Figure 4.24: Left figure shows the calibration curves of each ROI, using the relation, we can convert the pixel position along the dispersive direction to an energy scale for each crystal individually. Right figure shows the eight elastic lines shown in Figure 4.23 with the applied energy calibration.

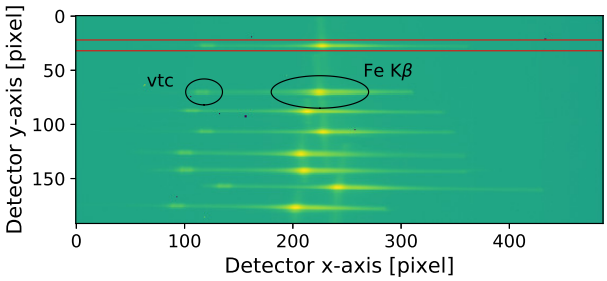

Figure 4.25: Example of how we set the ROIs on our detector images (marked with red lines) in order to extract the data required to create an emission spectrum. The iron Kβ emission signal of 0.5 M $K_4Fe(CN)_6$ in aqueous solution running in a 300 μm flat liquid jet was Bragg reflected with eight Si(440) crystals and focussed to a Pilatus 300k detector. The non-resonant emission was collected at 7500 eV incoming energy.

4.3.5 Methods for Background Subtraction

In most cases randomly scattered X-rays strike the detector (Figure 4.19). In order to remove this background, one can fit a polynomial or a Pearson function to several areas of the spectrum. Another way is to extract data from a detector area close to the signal ROI, that contains only background signal. The optimal procedure to remove the background has to be decided for each case individually.

Also interferences (so called analyzer crosstalk between the different analyzer crystals can occur as shown in Figure 4.21, which can not be removed with a standard proce-

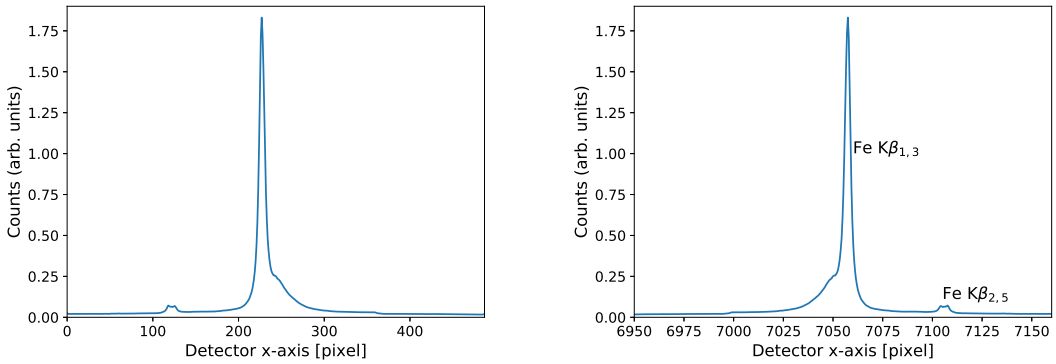

Figure 4.26: Left figure shows the summed up signal from one ROI, before the energy calibration has been applied. It is the same sample as presented in Figure 4.25. The right figure shows the spectrum after applying the energy calibration.

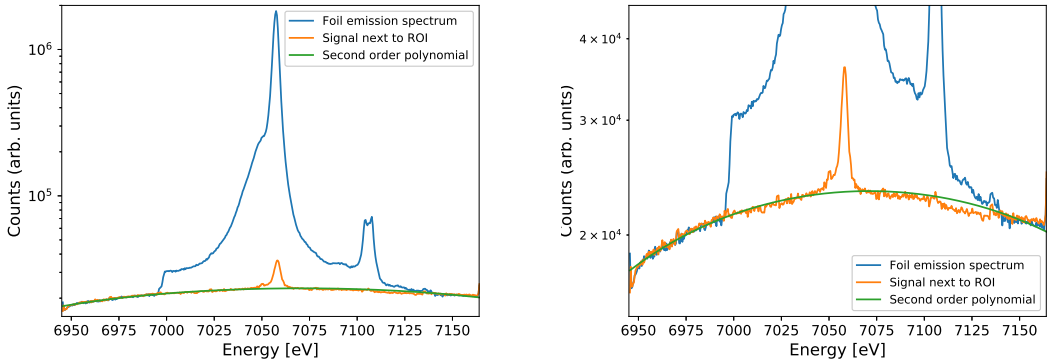

Figure 4.27: Left figure shows the integrated iron Kβ emission signal of 0.5 M $K_4Fe(CN)_6$ in aqueous solution collected by eight Si(440) crystals (blue) on a logarithmic scale. Additionally, an area of the detector lying next to the signals ROI has been integrated to obtain a distribution of the background with almost no emission signal in it (orange). We applied a second-order polynomial fit to the background (green). Right side shows the same but is zoomed into the background region. The slight drop in counts from about 7105-7130 eV are is related to the detector efficiency.

dure. So detector images always require visual inspection by the scientists before executing data extraction. For different spectroscopic setups there can be additional background, for example Compton scattering in X-ray Raman Scattering experiments, removal is achieved by dedicated software, for example XRStools[18]. After the separated signals have been compared to check for artifacts that may require discarding the spectra of certain analyzer crystals, the analyzed spectra of the single crystals can now be summed up in case of isotropic emission to receive the final spectrum(Figure 4.28).

[18]http://ftp.esrf.fr/scisoft/XRStools/

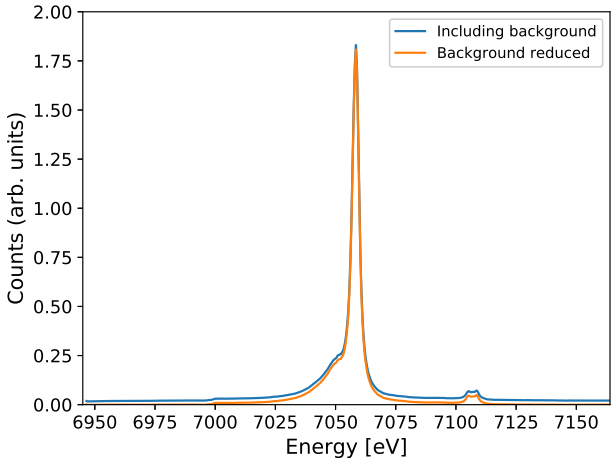

Figure 4.28: Spectrum of Kβ emission signal of 0.5 M $K_4Fe(CN)_6$ in aqueous solution collected by eight Si(440) crystals. Before (blue) and after (orange) background subtraction.

4.4 Commissioning of a 16-Element Von Hámos Spectrometer

In this section, we present the commissioning of a von Hámos spectrometer designed for the FXE scientific instrument of the European XFEL. We describe the technical specifications of the spectrometer before we present the results of the commissioning, which we conducted with elastic line measurements for Si(531) in the separated signal setup and for Si(220) crystals in the separated and overlapped signal setup. We test our data extraction and background subtraction by looking at the iron Kβ emission of 0.5 M $K_4Fe(CN)_6$ in aqueous solution, collected by eight Si(440) in separated and overlapped signal setup and compare the results of both setups.

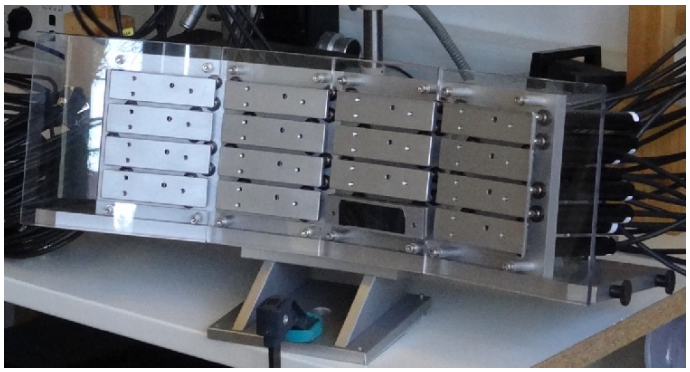

Figure 4.29: The von Hámos spectrometer at JJ X-ray, without crystals installed, one of the crystal mounts hosts a Si wafer, used to demonstrate the precision of the actuator movement.

4.4.1 Specifications

The von Hámos spectrometer (shown in Figure 4.29) was manufactured by JJ X-ray and designed to host up to 16 cylindrically bent analyzer crystals, arranged in four rows and four columns. The crystals are mounted on 16 aluminum plates, each driven by three actuators. The plates are attached to the actuators with a metal spring. Each aluminum plate hosts three magnets onto which the crystal with its metallic mount snaps on, thus allowing easy replacement of different crystals. The actuators move individually by up to 25 mm and thus can tilt the crystal up and down, left and right, or in combination, can move the crystal in linear direction towards the sample and detector. The actuators are driven by a Beckhoff control unit (Figure 4.30) connected to the von Hámos spectrometer via LEMO[19]-connectors.

[19] https://www.lemo.com

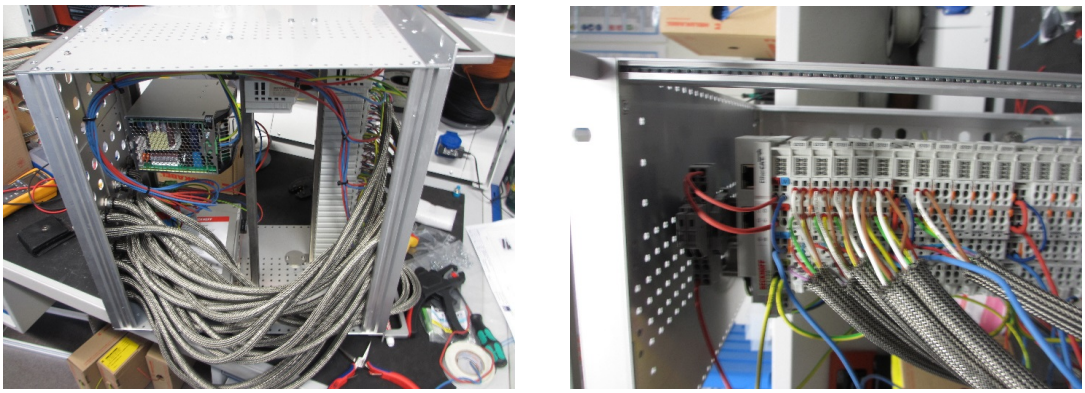

Figure 4.30: Beckhoff control unit to operate the 3x16 motors used to move the crystals mounted to the von Hámos spectrometer via LEMO-connectors.

The size of each crystal is 30 mm x 110 mm (VxH) with a bending radius of 500 mm, one of the crystals is shown in Figure 4.3. Close to backscattering, the surface of a single crystal is about 0.1% of 4π, thus the whole spectrometer covers about 1.7% of 4π with all 16 crystals. Table 4.1 lists the crystals that are currently available[20].

Table 4.1: Available crystals for the FXE von Hámos spectrometer.

Reflex	**Amount**	**Backscattering Energies < 15 keV (eV)**	**Surface**
Si(220)	12	6460, 9690, 13840	bent
Ge(220)	8	6200, 9300, 12420	bent
Ge(400)	3+2	4380, 8760, 13140	bent
Ge(111)	???	5700, 7600, 9500, 13300	bent
Si(531)	???	6760	bent

4.4.2 Commissioning

Commissioning experiments have been conducted at beamlines P01 of PETRA III, BL9 of DELTA and 7ID-D of APS. The spectrometer has been tested for several spectroscopic techniques: XES (which we used to demonstrate, time-resolved XES, HERFD XAS, RXES as well as XRS and IXS, the results will be shown in the next section. Here we present the results of measurements at P01, where elastically scattered light was used to test our calibration and investigate the energy resolution of the spectrometer as well as the properties of the crystals. After we used iron Kβ emission of $K_4Fe(CN)_6$ to verify our data extraction procedures.

[20] https://www.xfel.eu/facility/instruments/fxe/instrument_design/index_eng.html

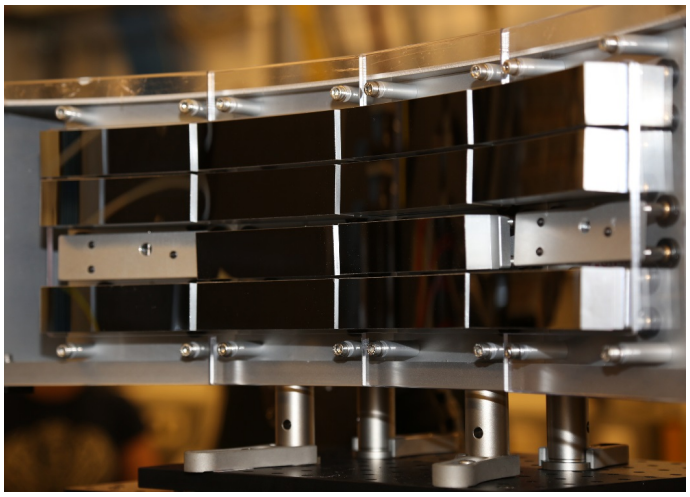

Figure 4.31: The von Hámos spectrometer set up at Beamline P01, PETRA III, equipped with 8xSi(220) in the two top rows and 6xSi(531) crystals in the two bottom rows.

We set up the von Hámos spectrometer for commissioning measurements in EH2 of P01 (Figure 4.31). The spectrometer was installed in the classic geometry, perpendicular to the incoming photon beam. The spectrometer was set to a height so that the center between rows 2 and 3 was 18.7 cm above the sample height. By doing so, we were just 2 mm off the optimal crystal height for measuring 7060 eV photons with Si(220) at 22.1 cm between rows 1 and 2 (from the top) of the spectrometer, while also being just 1 mm away from the optimal height of 15.3 cm to measure 7060 eV photons with Si(531) placed at rows 3 and 4. The exact crystal arrangement is described in table Table 4.2.

Orientation		**Col. 4**	**Col. 3**	**Col. 2**	**Col. 1**
Si(220)	Row 1	7	5	3	1
	Row 2	8	6	4	2
Si(531)	Row 3	-	4	2	-
	Row 4	6	5	3	1

Table 4.2: Crystal arrangement during the commissioning measurements, positions correspond to Figure 4.31

We used a Pilatus 300k detector, with an active area of 10.65 cm by 8.38 cm, its pixel size was 172 μm x 172 μm. The center of the active area had to be adjusted to either 30.6 cm or 44.2 cm, depending on if we wanted to detect the signals coming from Si(531) or Si(440) analyzer crystals. We used the Si(111) and Si(311) DCM of P01 with an energy resolution of about 1 eV and 200 meV and a flux of about 5*10^{13} and 1*10^{13} photons per second, respectively. With beryllium CRL we focussed the beam down to 80 μm by 200 μm (VxH) at the sample position with 7500 eV incoming energy. For our elastic line measurements

around 7100 eV, we achieved a focus of about 100 μm by 200 μm (vxh). The samples used for elastic line measurements were a 10 μm thin iron foil and a 300 μm liquid jet running aqueous solution of 0.5 M $K_4Fe(CN)_6$.

Elastic line measurements

We measured elastic lines with six Si(531) analyzer crystals focussed on separated spots on the Pilatus detector (Figure 4.32). We used a 5 μm thin iron foil as elastic scatterer and

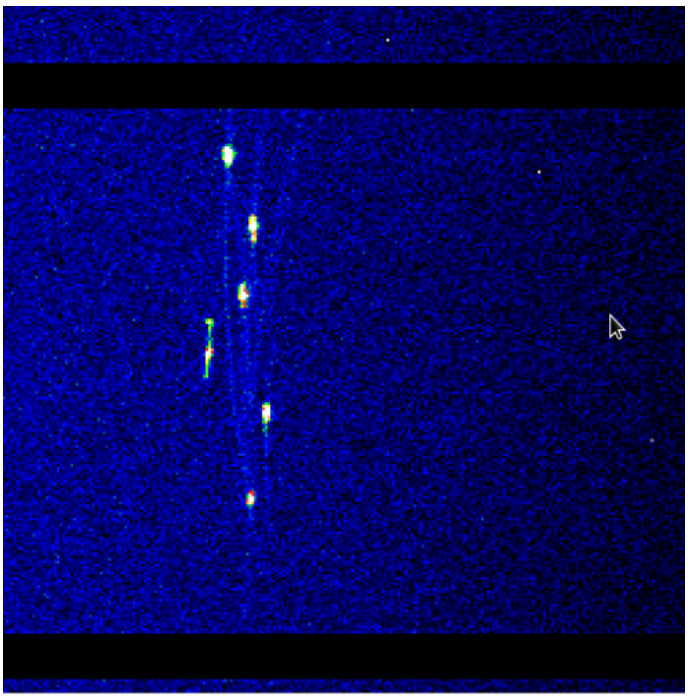

Figure 4.32: Elastic lines measured with Si(531) crystals using a 5 μm thin iron foil designed for EXAFS calibration measurements. The image has been recorded with a Pilatus 300k detector. The fourth crystal from top shows a line along the imaging direction, resulting from bad focussing properties.

recorded elastic signals with energies from 7030 up to 7080 eV in 10 eV steps using the Si(311) mono. The detector data has been extracted as described in the previous section. Using six crystals and six energies, we ended up with 36 elastic lines. Using Gauss fits, we determined the average elastic line width to be about 550 meV, in combination with the Si(311) DCM resolution of 200 meV, this results in about 500 meV resolution for each crystal in this scattering geometry. The signals average width being around 1.6 pixel in average indicates that the pixel size of 172 μm in combination with the 100 μm vertical beam size was already a limiting factor for the energy resolution in this setup.

We proceeded to measure elastic lines with eight Si(220) analyzer crystals, using the

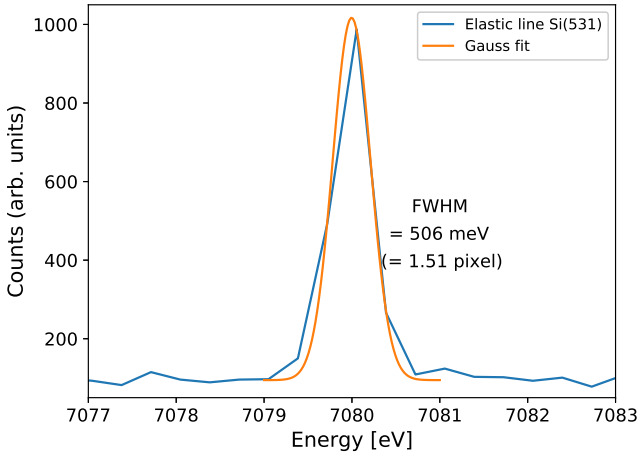

Figure 4.33: Elastic line recorded with a Si(531) analyzer crystal, extracted from the detector image shown in Figure 4.32. A fit has been applied to determine the line width corresponding to the total energy resolution.

Si(440) reflex and the Si(111) DCM. We used a 300 μm thick liquid jet running 0.5 M aqueous solution of $K_4Fe(CN)_6$ as scatterer. We started with the crystals being focussed on separated spots on the detector. We obtained the function between pixel position and energy for each crystal using a second-order polynomial fit, by recording the elastic line positions at different energies and applying a Gauss fit to retrieve the exact positions of the elastic lines of each crystal on the detector. These are the measurements we previously showed to introduce the energy calibration procedure in the previous section. Figure 4.34 shows one of the recorded elastic lines and the fit applied to it. In average

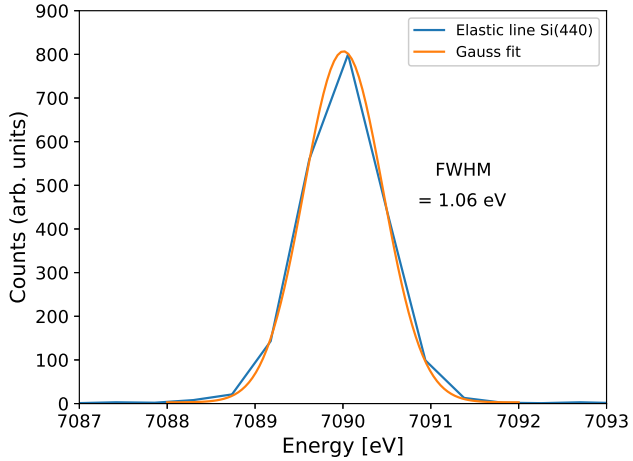

Figure 4.34: Elastic line recorded with a Si(220) analyzer crystal, extracted from one of the detector images shown in Figure 4.23. A fit has been applied to determine the line width corresponding total energy resolution.

the recorded elastic lines have a FWHM of 1.06 eV, (2.4 pixels). The main contribution

is the energy resolution of about 1 eV by the Si(111) DCM we used. From the elastic line measurement we determined the different energy per pixel functions of each crystal (Figure 4.35).

The function depends on the crystal height in the spectrometer. Table 4.3 gives info

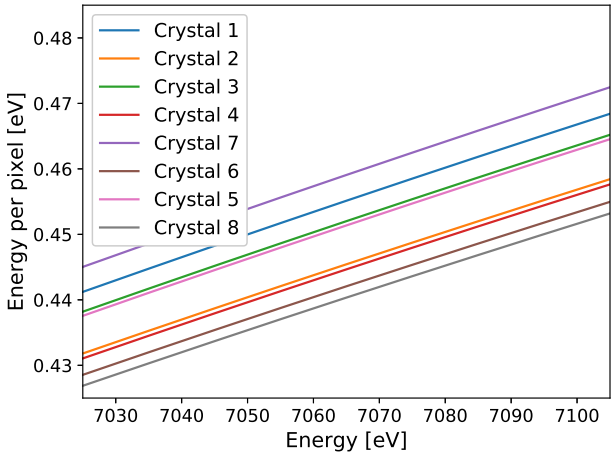

Figure 4.35: Energy per pixel curves for 8 Si(220) arranged in two neighboring rows on the von Hámos spectrometer. The curves can be grouped in two bands, the first group coming from crystals with odd numbers mounted in the top row and the second group from the even-numbered crystals mounted in the second row from top.

about each crystal position and the measured energy per pixel difference between the crystals of rows one and two. The expected difference of energy per pixel between crystals of row one and row two is about 10 meV according to Equation 4.15, as shown in Figure 4.16, which is in good agreement with this data.

With this separated crystal setup, we recorded the iron Kβ emission spectrum of our sample with 7500 eV incoming energy. This will be presented later when we compare it to the Kβ spectrum of the same sample collected with overlapped crystal setup. First, we will have a look at the elastic line measurements with overlapped crystals. To overlap the crystals, we adjusted the crystals to focus on the same region of the detector, aiming to match one selected energy (7050 eV) in one pixel located at (x=220, y=107), a detector image was previously shown in Figure 4.20. In this new arrangement, we repeated the elastic line measurement. A combined plot of the elastic lines at all energies is shown in Figure 4.36. One can see how the elastic lines width increases when going away from x=220 towards higher x-values (i.e. higher energies) and start to split into two peaks at x=112, presumably one peak coming from each row of analyzers. The elastic line widths have been extracted and a fit using a second-order polynomial has been applied to estimate the ideal focus position. The broadening we expect from crystals positioned in two neighboring rows of the spectrometer calculated via Equation 4.15 has been combined with the 1 eV resolution at the energy of ideal overlap for the crystals in order to obtain

Crystal Si(220)	**Row**	**Column**	**ROI** [y_{min}, y_{max}]	Δ_{Disp} [meV/pixel]
1	1	1	[23, 30]	∼10
2	2	1	[67, 74]	
3	1	2	[85, 91]	∼6
4	2	2	[104, 110]	
5	1	3	[122, 131]	∼8
6	2	3	[139, 146]	
7	1	4	[154, 162]	∼18
8	2	4	[171, 180]	

Table 4.3: Crystal setup used to demonstrate the calibration of the spectrometer. Rows and columns refer to how the crystals were mounted at the spectrometer, it is the same setup as shown in Figure 4.31, rows are counting from top to bottom and columns from right to left. Δ_{Disp} describes the difference between the energy per pixel derived from the calibration curves.

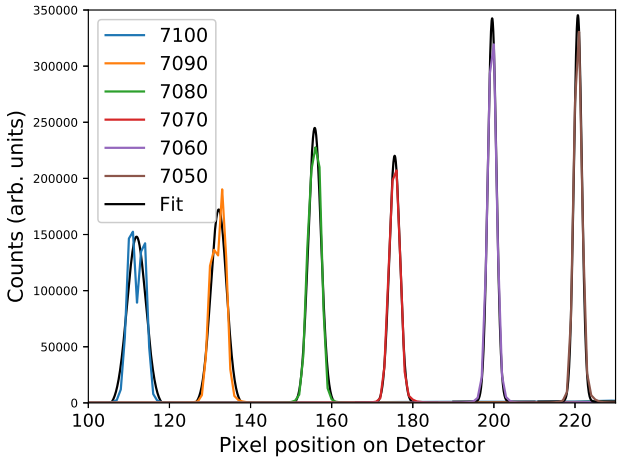

Figure 4.36: Elastic line measurements of eight overlapped Si(220) crystals, recorded from 7050 to 7100 eV in 10 eV steps. The crystals were previously aligned to give the best energy resolution (i.e. most narrow elastic line) at 7050 eV on x=220. A Gauss fit has been applied to each elastic line to extract the FWHM.

an estimate of the broadening (Figure 4.37).

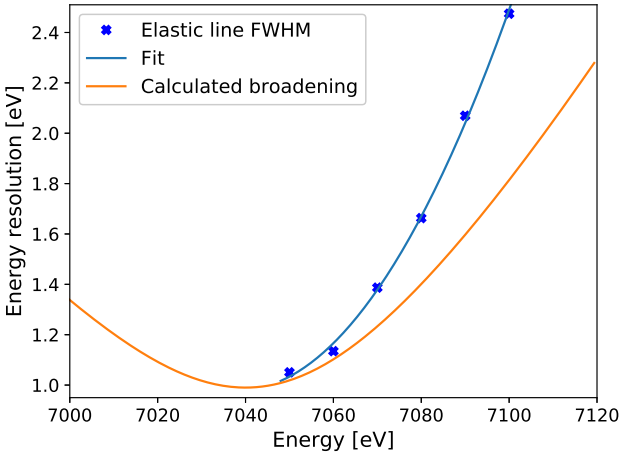

Figure 4.37: Elastic line widths obtained with a Gauss fit from eight overlapped Si(220) at six different energies (blue crosses) have been plotted and fitted with a second-order polynomial (blue line). The fit suggests that the smallest elastic line width (i.e. the ideal overlap) is about 1 eV at around 7040 eV. Based on these values, we show the theoretical broadening of crystals in neighboring rows according to Equation 4.15 (orange).

Emission tests

With the overlapped and the separated Si(220) crystal setup we measured the Fe Kβ spectrum of 0.5 M $K_4Fe(CN)_6$ in aqueous solution to demonstrate the advantages and disadvantages of both setups. When integrating the separated signals, the signals com-

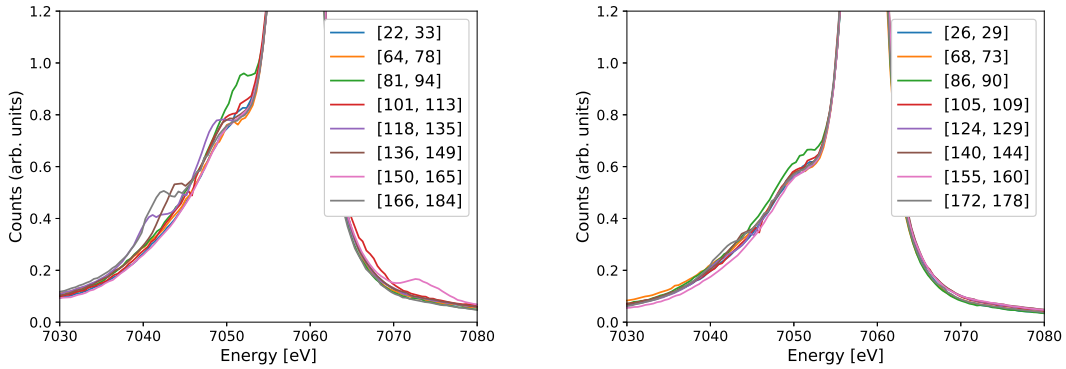

Figure 4.38: Zoom into the Fe Kβ spectra of 0.5 M $K_4Fe(CN)_6$ in aqueous solution extracted from separated crystals. Left figure shows the spectra collected from larger ROIs, exhibiting many artifacts, spoiling the pure Fe Kβ signal. Right figure shows spectra collected by using narrow ROIs, the green and gray spectra still show differences compared to the other spectra, but overall there are much fewer interfering features.

ing from different analyzers can interfere with each other. In Figure 4.21 one can see that all analyzers show additional signal along the imaging direction around the signal coming from the K$\beta_{1,3}$ peak. By carefully selecting the ROIs to extract the emission signal, one can reduce this effect to some extent. Still, it is critical when these additional signals overlap with an area designated to collect the emission signal of another crystal. For example, the second and fourth crystals from top give additional intensity in the detector area designated to collect the emission signal of crystal 3. Also, the signal coming from crystal 7 overlaps with the signals coming from crystals 5, 6 and 8. We extracted the emission signal of this measurement with two different ROI settings (Figure 4.38). As can be seen, larger ROIs can lead to additional interferences being integrated and adding to the spectra extracted. But even with narrow ROI some spectra exhibit artifacts. In the worst case, the signal from certain analyzers (for us crystals 2 and 8) has to be discarded and can not be used for further analysis. This is even more critical in experiments with anisotropic emitted radiation, where each crystal sees a different distribution of X-rays and the separated signals can not be compared as easily to double-check for artifacts.

With the applied energy calibration the spectra recorded with separated crystal setup can be summed up and compared to the signal coming from the overlapped crystal setup. Figure 4.39 shows the signals normalized to the K$\beta_{1,3}$ peak on a logarithmic scale. One can see that the background in the overlapped setup is about a factor 4 lower.

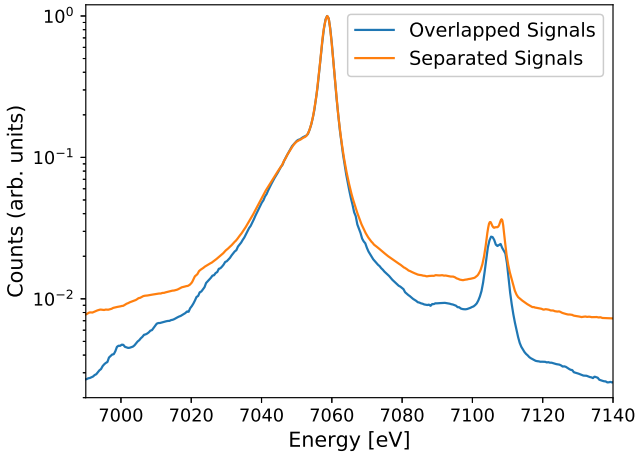

Figure 4.39: Emission spectra of 0.5 M $K_4Fe(CN)_6$ in aqueous solution, recorded with overlapped and separated signal setup. Spectra have been normalized to the K$\beta_{1,3}$ and are displayed on a logarithmic scale to illustrate the different backgrounds.

Subtracting the second-order polynomial fit (shown in Figure 4.27) from our spectra, we receive the background corrected emission spectra (Figure 4.40). One can see that the spectra are almost identical. They are in good agreement with the literature data[74]. This is to be expected, as we optimized the crystals to overlap their signals in this energy range and the elastic line measurements indicated an energy resolution below 1.2 eV here.

The valence-to-core region however is about 60 to 70 eV away from the optimal over-

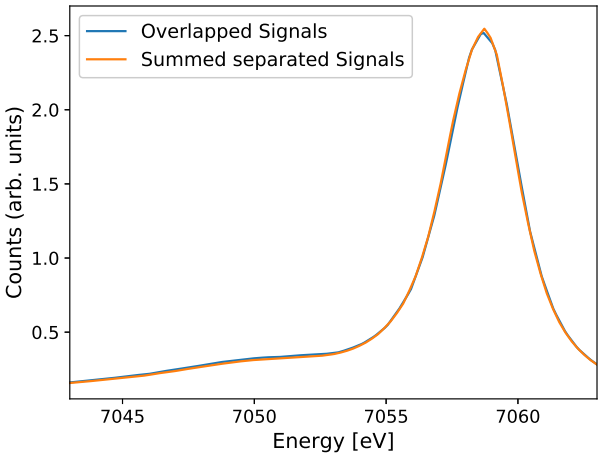

Figure 4.40: Background corrected Fe Kβ spectra of 0.5 M $K_4Fe(CN)_6$ in aqueous solution, recorded using overlapped and separated crystal signals. The spectra are almost identical.

lap energy. Here we can see significant differences in the spectra recorded with both setups (Figure 4.41). The spectrum recorded using separated signals resembles the liter-

ature $K_4Fe(CN)_6$ vtc spectrum very well, while the spectrum recorded using overlapped signals looks rather like $K_3Fe(CN)_6$ [12]. However $K_4Fe(CN)_6$ is not known to degrade into $K_3Fe(CN)_6$ and also the K$\beta_{1,3}$ spectrum of $K_3Fe(CN)_6$ looks different from the simultaneously recorded K$\beta_{1,3}$ spectrum in the overlapped signal setup. The vtc spectrum

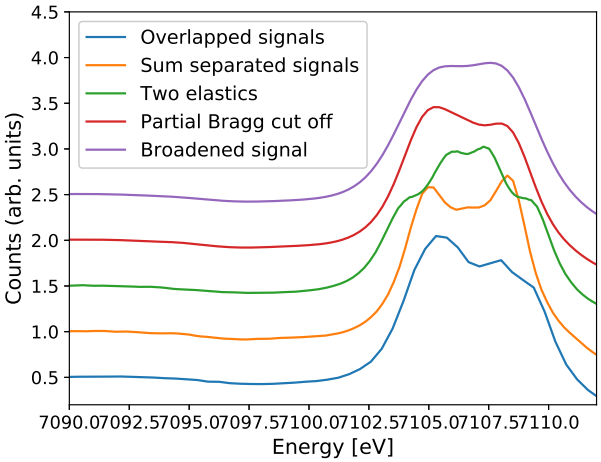

Figure 4.41: The vtc spectra of the overlapped (blue) and separated (orange) signal setup. The separated signal spectrum is in good agreement with the literature(Assefa) and we use it to reconstruct the overlapped spectrum. We broadened the spectrum by 2 eV (purple) and reconstructed a spectrum coming from two overlapped neighboring analyzer rows (green). We simulated the case where one of the overlapped crystal's Bragg range ended at 7107 eV (red).

recorded by the overlapped setup can not be reproduced by a broadening of the actual vtc spectrum according to the overlapped setup energy resolution. Additionally we reconstructed a vtc spectrum that arises from two groups of crystals with good energy resolution but different energy calibration, resembling a spectrum collected via two crystals arranged in neighboring rows on the spectrometer. To do so, we divided the actual vtc spectrum by 2 and shifted it by ± 1 eV before adding both resulting spectra again. However, this also can not reproduce the overlapped signal setup vtc spectrum. One possible explanation is that one of the crystal's Bragg range ended within the vtc spectrum, to simulate this case, we multiplied the actual vtc spectrum above 7107 eV by a factor of 0.875 and added a broadening. This seems to resemble the spectral shape of the overlapped signal setup vtc spectrum, despite some additional broadening. This suggests, that even though we aligned the separated crystal setup in a way that each crystal was able to record the full vtc spectrum, as can be seen in Figure 4.42, one of the crystals was not sufficiently aligned to record the full vtc in the overlapped signal setup.

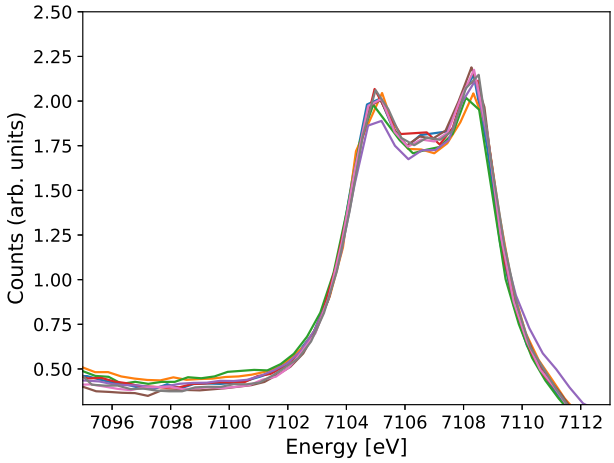

Figure 4.42: The vtc spectra for all eight crystals recorded in separated signal setup, they all show the same features at the same energies, indicating that the alignment was done properly and our background subtraction and energy calibration works well.

4.5 Spectroscopic Applications

The von Hámos spectrometer can be used for different spectroscopic techniques. Previously we presented measurements of the iron Kβ spectrum of 0.5 M $K_4Fe(CN)_6$ in aqueous solution. In this section, we present a selection of our measurements to demonstrate the capabilities of the von Hámos spectrometer to perform time-resolved non-resonant XES, RXES in combination with PFY-XAS and finally IXS probing valence-hole and core-hole excitations.

4.5.1 Non-Resonant XES

At Beamline P01 of PETRA III we measured the picosecond time-resolved altering of the spin state of 20 mM $[Fe(II)(bpy)_3]^{2+}$ in acetonitrile via optical pump, non-resonant XES probe. The sample was delivered by a 100 μm thick flat jet, onto which the optical laser and the X-ray beam were spatially overlapped, the time delay between pump and probe signal was set to 200 ps. We used the second harmonic of a Tangerine laser at 515 nm with a spot size of 50x50 μm^2, the output power was 1.8 W and the repetition rate 1.3 MHz. With PETRA III running in 40 bunch mode, corresponding to 5.2 MHz, we excited the sample every fourth X-ray pulse. The Si(111) DCM of P01 provided $6*10^{12}$ photons per second at 7500 eV incoming energy. The X-rays were focused down to 45x15 μm^2 (HxV) with a KB system. The von Hámos was equipped with eight Si(220) analyzers, mounted in two different rows. We used the Si(440) reflex with the crystals centered around 66° Bragg angle, in order to record the emission signal. Therefore, we overlapped the signals of all crystals on a Pilatus 100k detector at 7060 eV. After subtracting the not-pumped emission signal (LASER OFF) from the pumped signal (LASER ON), shown in Figure 4.43. With an excitation yield of 1/6, we receive a transient signal for $[Fe(II)(bpy)_3]^{2+}$ whose amplitude overlaps well with the literature difference data the between quintet high-spin and the singlet low-spin reference spectrum [114].

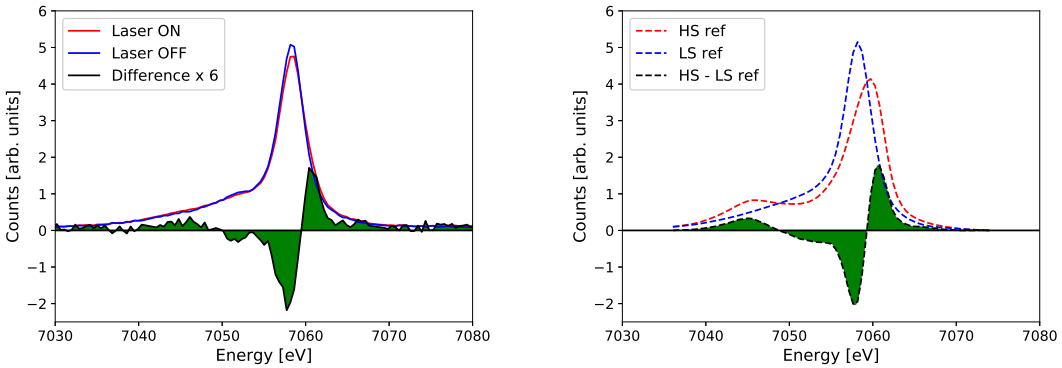

Figure 4.43: Left figure shows the transient signal of iron Kβ emission signal of 20 mM $[Fe(bpy)_3]^{2+}$ in acetonitrile, measured at beamline P01, PETRA III. Right figure shows reference data for the high-spin quintet and low-spin singlet state[114]. See text for experimental details.

Covering the full 1s emission of iron, we simultaneously measured the iron Kα and Kβ (including vtc) emssion spectrum of photoexcited 20 mM $[Fe(terpy)_2]^{2+}$ in aqueous solution (Figure 4.44). The Kα emission was captured with eight striped Si(333) crystals, overlapped on two different ROIs of the Pilatus 100k detector, while the Kβ emission was collected by eight Si(440) crystals. Using the huge solid angle of the spectrometer helped capture the weak vtc signal and enabled the first picosecond time-resolved measurement of iron vtc spectra, still it took 19 hours for data taking to produce the spectra. In addition, the dispersive nature of the von Hámos crystals delivered self-normalized spectra, required for laser-pumped liquid jet experiments prone to instabilities. The measurements have been published [73].

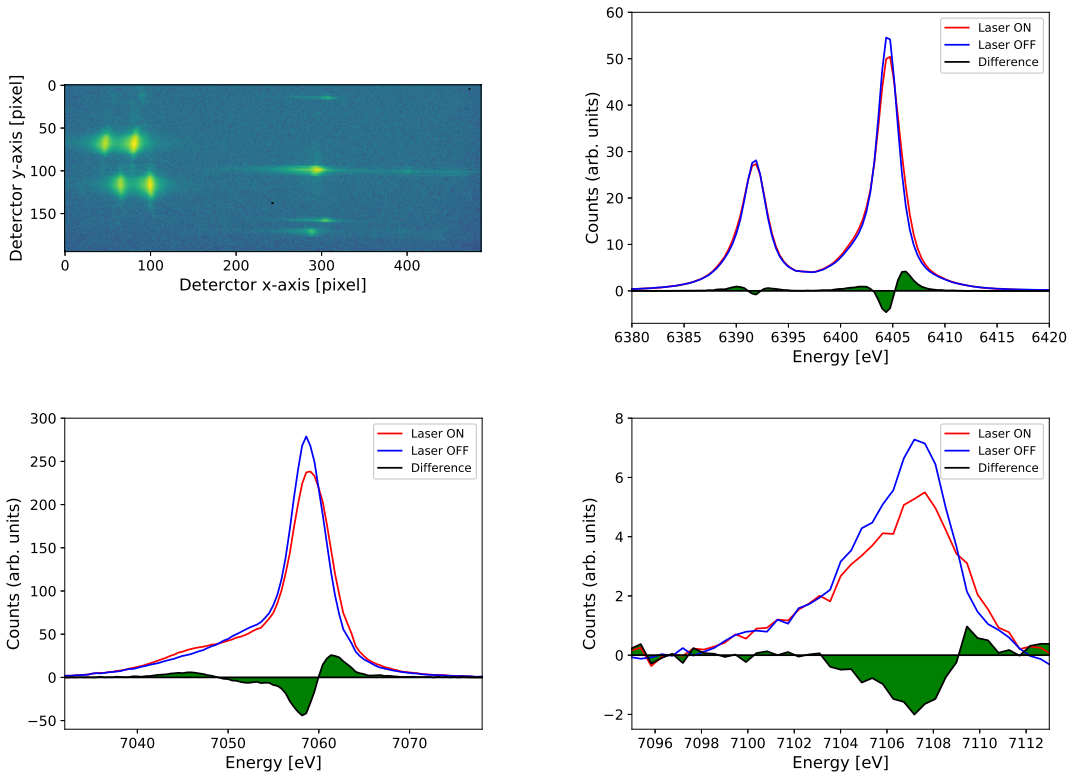

Figure 4.44: Transient iron Kα and Kβ emission experiment of 20 mM $[Fe(terpy)_2]$ in aqueous solution. Pilatus 100k raw data (upper left image): The two groups consisting of four Si(111) striped analyzers are giving Fe Kα emission signal to the left part of the detector. In the middle to right part (y = 100) one can see the Kβ emission signal collected by eight overlapped Si(220) crystals. There is some additional spatially separated emission in areas with y < 40 and y > 159, most likely stemming from windows that got contaminated with sample due to jet instabilities. Upper right image shows the Kα emission recorded 100 ps after excitation (red) and hundreds of ns after excitation (blue) as well as the difference (green area). Lower images show the K$\beta_{1,3}$ (left) and vtc emission with same notation.

4.5.2 Resonant XES and PFY(HERFD) XAS

To demonstrate the feasibility of recording PFY or HERFD XAS spectra with the von Hámos, we recorded the resonant iron K$\beta_{1,3}$ emission of 250 mM $[Fe(II)(CN)_6]^{4+}$ and 250 mM $[Fe(III)(CN)_6]^{3+}$ in aqueous solution. The spectra were recorded at PETRA III, beamline P01 with the same beamline and spectrometer parameters as described in subsection 4.5.1. We scanned the incoming photon energy and collected a spectrum for each energy. Here we show the collected spectra as RIXS maps (Figure 4.45). To our best

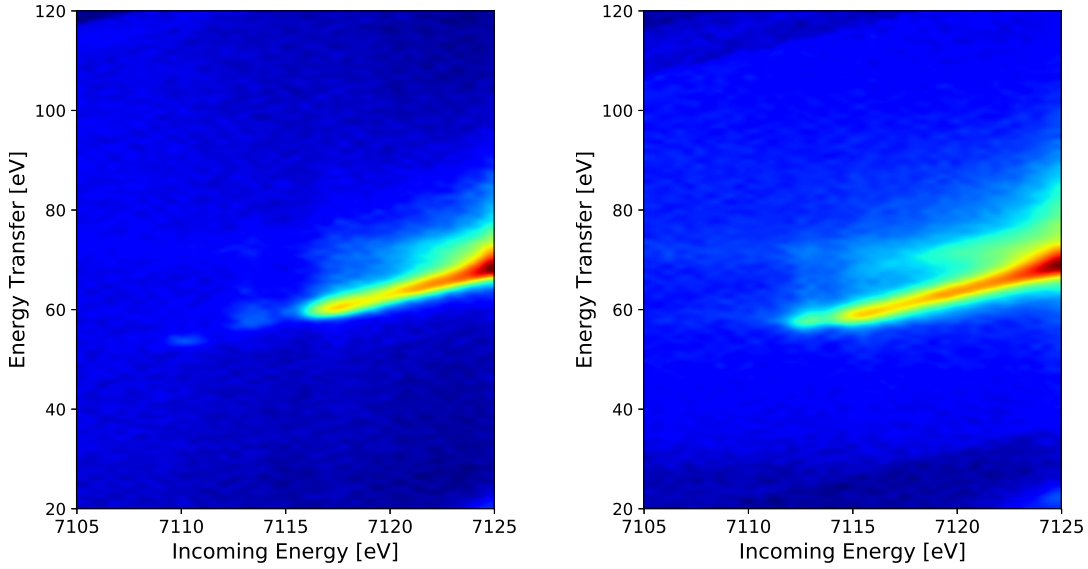

Figure 4.45: K$\beta_{1,3}$ RIXS maps of 250 mM $[Fe(III)(CN)_6]^{3+}$ (left figure) and 250 mM $[Fe(II)(CN)_6]^{4+}$ (right figure) in aqueous solution, measured at beamline P01, PETRA III. The energy transfer axis was obtained by subtracting the recorded energy from the incoming X-ray energy.

knowledge the iron K$\beta_{1,3}$ RIXS maps of $K_4Fe(CN)_6$ and $K_3Fe(CN)_6$ have not been published, yet. However, there have been resonant measurements on the Kα and vtc emission. [69][13][58]. By integration of the RIXS map, we receive a PFY XAS spectrum (Figure 4.46). We compare it with a reference spectrum measured using TFY at 7ID-D, APS. The reference measurement has been published [12]. There are some minor differences in the intensity of the pre-edge features, this can be the effect of HERFD. However, we do not expect a big change, since the incoming photon beam was delivered by the Si(111) DCM of P01, thus the energy resolution of the incoming beam was above 1 eV.

In another experiment, we compared the PFY spectrum recorded by the von Hámos with a simultaneously measured TFY spectrum collected with a PIN diode (Figure 4.47). The sample was 1 M $ZnBr_2$ in aqueous solution running in a 500 μm thick cylindrical jet. We used the (660) reflex of eight Si(220) analyzer crystals to record the Br Kα emission for PFY mode. On a Pilatus 100k detector, we overlapped the signals of the eight crystals,

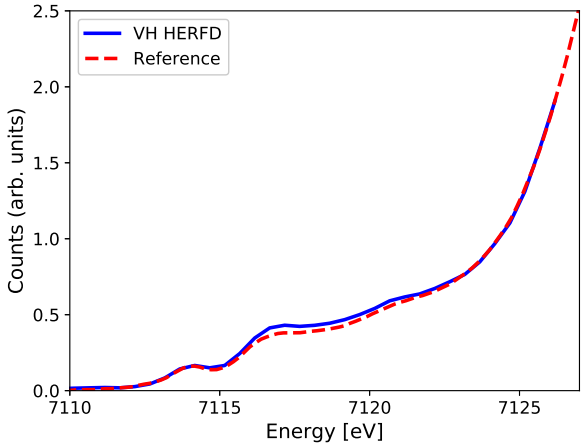

Figure 4.46: Pre-edge region of the iron K-edge XANES spectrum of 250 mM $[Fe(II)(CN)_6]^{4+}$ in aqueous solution (blue), obtained as HERFD spectrum by integrating the Kβ RIXS map shown in Figure 4.45. Reference spectrum (red dashed) was measured from 20 mM $[Fe(II)(CN)_6]^{4+}$ as TFY spectrum at beamline 7ID-D, APS.

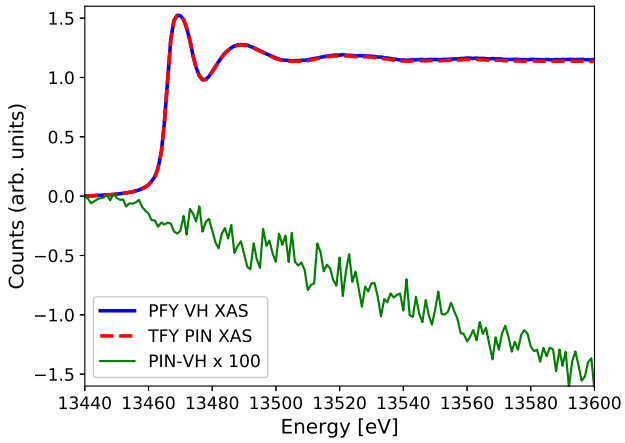

Figure 4.47: Bromide K-edge XANES simultaneously measured via TFY with a PIN diode (red) as well as HERFD XANES obtained from a Kα RXES measurement of 1 M $ZnBr_2$ in aqueous solution, using the von Hámos spectrometer (blue). The difference between the TFY and the HERFD signal is multiplied by 100 to show the subtle differences (green).

attached to two different rows in the spectrometer. The Si(111) DCM of P01 delivered 10^{13} photons per second with an energy resolution of about 2 eV. To show that the difference

between the TFY and PFY is not constant, it is multiplied by a factor of 100. The difference shows a linear trend, which can be explained by the different geometric positions of the von Hámos and the PIN diode with regard to the jet. This could have led to different intensities, resulting from the energy-dependent penetration depth of the incoming photons into the sample.

4.5.3 IXS

Valence hole and core hole excitations of light elements can be measured using inelastic X-ray spectroscopy. With its dispersive nature, the von Hámos spectrometer offers the possibility to measure such spectra in a static setup. We measured the dynamic structure factor S($\mathbf{q}$,ω) of a beryllium single crystal as well as the Be K-edge via X-ray Raman scattering. The experiment was performed at BL9, DELTA. The spectrometer was set up in the classic geometry, looking at the sample from the downstream side with an angle of 45° with regards to the X-ray beam direction. The height of the center of the spectrometer was set to 10.5 cm. Using the (660) reflex, we adjusted five separated Si(220) crystal analyzers to Bragg-reflect photons with the energy of 9900 eV to the center of a Pilatus 100k detector, which was set at a height of 21.1 cm above the sample. The vertical exit slit was set to 0.5 mm, defining the focus in the dispersive direction. The incoming energy was set to 9930 eV. Figure 4.48 shows the spectra of the different crystals with the calcu-

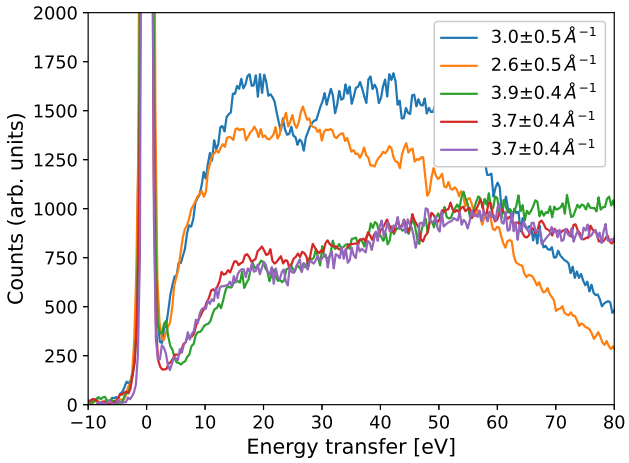

Figure 4.48: Dynamic structure factor S($\mathbf{q}$,ω) of beryllium at different momentum transfers measured at BL9, DELTA. Data was taken over 2 hours.

lated momentum transfer values. The elastic line widths indicate an energy resolution of about 1.4 eV. The spectrum for 2.6±0.5 Å^{-1} momentum transfer (orange, scattering angle 2θ = 30.4°) is similar to the dynamic structure factor for momentum transfer $\mathbf{q}$ parallel to the [100] direction with 2.6 Å^{-1}, as described in [96], while the 3.0±0.5 Å^{-1} is similar to $\mathbf{q}$ parallel to the [110] direction (around 2.6 - 3.2 Å^{-1}). For the higher momentum transfer values, above 3.5 Å^{-1} (e.g. red, scattering angle 2θ = 43°) there is no reference data.
For the same setup, we set the incoming energy to 10020 eV to record the Be K-edge spectrum with XRS (Figure 4.49). For all momentum transfers, the spectra look very similar. Comparing it with the literature [104] it seems like it can not be directly reproduced by the high q (=9 Å^{-1}) measurement, while our crystals sit at 2.6 up to 3.8±0.5 Å^{-1}. Our observations are in line with a Be-K-edge XRS spectrum for $\mathbf{q}$ approximately parallel to

[100] with momentum transfer between 1.2 and 9 $Å^{-1}$.

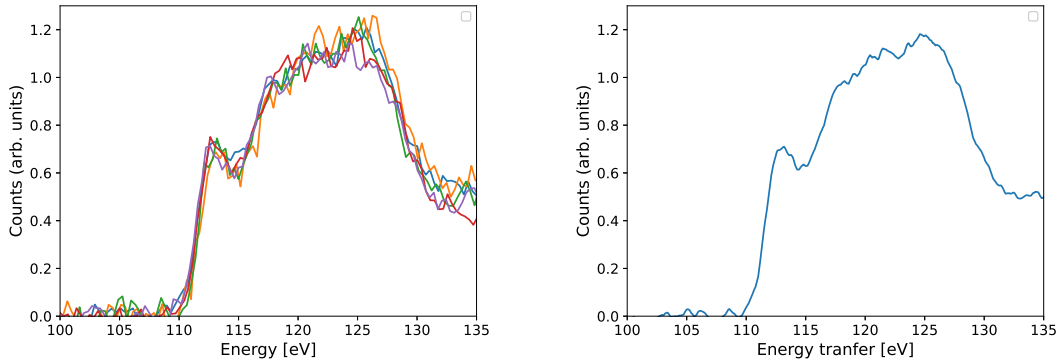

Figure 4.49: Beryllium K-edge spectrum, left figure shows the single spectra recorded by five crystals, right figure shows the sum of the spectra. Data was recorded for 10 hours at BL9 of DELTA.

With the same setting of beamline BL9 of DELTA, we overlapped the signals of eight crystals to two spots on the detector and increased the incoming photon energy to 10200 eV to match the energy transfer with the carbon K-edge to conduct XRS spectroscopy on HOPG (highly oriented pyrolytic graphite). We measured the sample for 2.5 hours and then rotated it by 90° and measured again for 3 hours (Figure 4.50). The resulting spectra

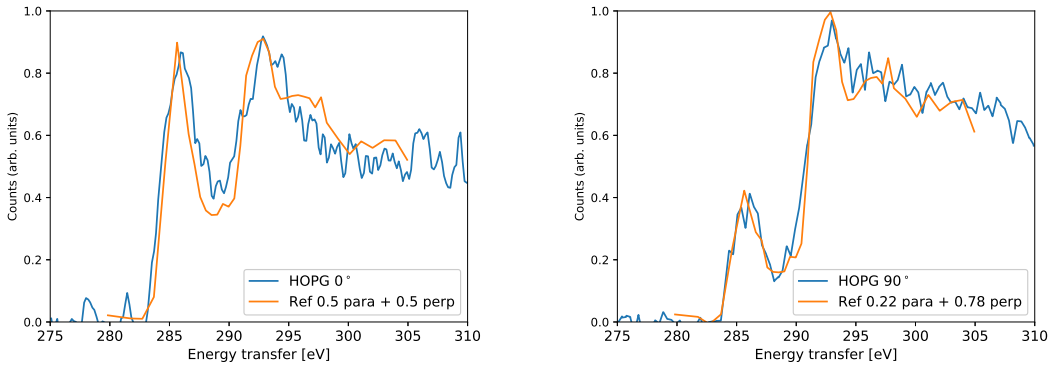

Figure 4.50: Blue spectra show the C K-edge spectrum of HOPG measured with X-ray Raman scattering spectroscopy in two different orientations at BL9, DELTA. Data was taken over 2.5 hours for 0° and 3 hours for 90°. The orange spectra show reconstructed spectra by using linear combinations of the reference spectra parallel (para) and perpendicular (perp) to the crystal orientation published in [83].

can be reproduced by linear combinations of reference spectra taken for HOPG probing parallel and perpendicular to the crystal orientation, in order to probe the π- and σ-states, represented by the peaks at 286 eV and 292 eV, respectively[83]. By turning the sample by 90°, we would expect a reversal of the parallel and perpendicular contribution. The mismatch indicates that either the sample was not well aligned with regards to the incoming beam or not moved by 90°.

To estimate the performance of the spectrometer for future experiments on water, we measured the oxygen K-edge of H_2O running in a 300 μm thick liquid flat jet. The measurements were performed at beamline P01, PETRA III. The experimental details are the same as for the overlapped crystal case described in section 4.4, where we set up the spectrometer to measure the iron Kβ spectrum around 7060 eV. To collect the photons yielding the oxygen K-edge information from 530 to 550 eV, the incoming photon energy was tuned to 7590 eV. To record the spectrum, we collected data for about 400 minutes.

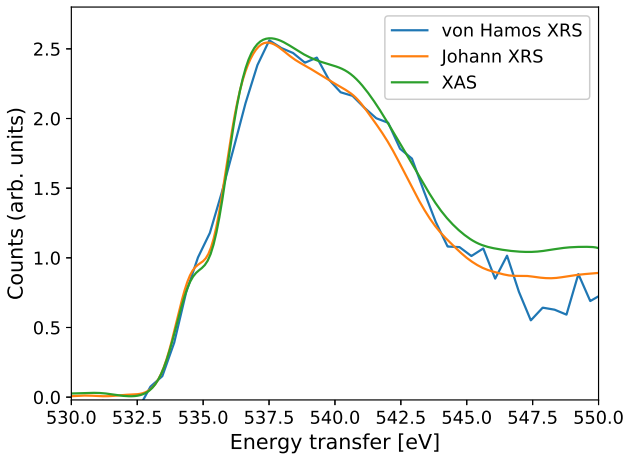

Figure 4.51: O K-edge spectrum of H_2O, measured with X-ray Raman scattering spectroscopy using the von Hámos and the Johann XRS spectrometer of beamline P01, PETRA III. Soft X-ray XAS measurements from[82]. Johann XRS and soft XAS data have been broadened to match the von Hámos energy resolution.

This long acquisition time was required because the spectrometer was optimized to measure iron emission signal and not XRS. This meant a non-ideal thickness of the sample, the positioning of the spectrometer at 90° with regards to the incoming beam to suppress elastic scattering and a rather small Bragg angle of about 66°, leading to a small solid angle per eV. Considering these settings, in a dedicated setup, the signal should be at least an order of magnitude stronger. Comparing it to the spectrum recorded over 40 minutes by the Johann-type XRS spectrometer of P01, it looks similar, but noisier, as to be expected (Figure 4.51). This suggests that to receive a better estimate, one has to repeat the experiment with the spectrometer set to ideal conditions. In addition, we show a soft X-ray spectrum recorded in transmission mode[82].

5 A Novel Method to Probe Coordination and Bond Distance

Knowledge of the local environment around an ion is important input used to describe the structure and function of crystalline or amorphous materials. Also in transition metal-complexes, the nearest neighbor bond distances and the coordination number around the central metal ion are characteristic attributes. Several definitions of coordination can be found in literature. In this chapter on GeO_2, the coordination number describes the number of neighboring oxygen atoms in closest proximity to germanium. These oxygen atoms form the first coordination shell. Directly related to the coordination is the germanium bond distance to its neighboring oxygens. In our case the term bond distance describes the mean bond distance of all oxygens in the first coordination shell. The usual techniques to measure the coordination number and bond distances in materials are X-ray diffraction (XRD) and extended X-ray absorption fine structure (EXAFS) but also neutron diffraction (ND)[94][14][65]. For GeO_2 solids, the Ge-O bond distance is directly related to its coordination number. So far, valence-to-core (vtc) X-ray emission has mostly been used to probe the spin state and to identify the type of ligands in different transition metal complexes[19]. We show that a relationship between coordination number and bond distance in amorphous GeO_2 can be extracted by exploiting vtc X-ray emission spectroscopy. Recording the emission by using the von Hámos spectrometer, we track the structural transition in amorphous and crystalline GeO_2 between 0 and 30 GPa, in order to introduce this new method to probe coordination number and bond distance. The compaction mechanism of amorphous GeO_2 up to 30 GPa has already been measured in several X-ray diffraction and EXAFS studies[35][65][14][77][53][52]. In this chapter we show that the present results are in agreement with these XRD and EXAFS measurements, therefore validating our approach. In addition, we support our measurements by spectral Bethe-Salpeter calculations. Finally, we point out scientific cases, where vtc X-ray emission can reveal information that is currently beyond the sensitivity of XRD and EXAFS.

5.1 The Model System: GeO_2 Polymorphs

Due to its structural similarity to SiO_2, GeO_2 is of interest for current geochemical and geophysical research. It is also used in technical glasses. It can be found in different polymorphs, here we investigated amorphous (a-GeO_2), poly-crystalline four-fold coordinated quartz-like (q-GeO_2, space group $P3_221$) and six-fold coordinated rutile-like (r-

GeO_2, space group $P4_2/mnm$)[24]. Figure 5.1 shows the elementary structures of q-GeO_2

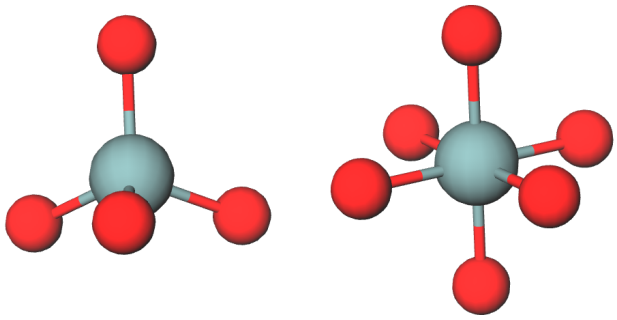

Figure 5.1: Ge environment of quartz-like (left) and rutile-like GeO_2 (right). The central Ge atom is surrounded by either four or six neighboring oxygen atoms, defining the germanium coordination.

and r-GeO_2, the GeO_4 tetrahedron and the GeO_6 octahedron respectively (rendered with Molview[21]. Depending on the coordination, the bond distances change: Under ambient conditions these are 1.74 Å for q-GeO_2 and 1.88 Å for r-GeO_2.

5.1.1 Calculations of GeO_2 valence-to-core spectra

Valence electrons are very sensitive to the local environment of the absorbing atom and thus can be used to study small changes to coordination and bond lengths. By numerical solutions of the Bethe-Salpeter equation, as implemented in OCEAN[40], we calculated valence-to-core spectra of GeO_2 polymorphs. Using the local density approximation for the exchange-correlation functional, the ground state electronic structure was obtained by density functional theory implemented in quantum ESPRESSO[22]. The calculated spectra were shifted in energy to match the energy of the Kβ_5 energy of the measured spectra. The Kβ_5 served as a constant internal energy calibration, as explained in section 5.3. The vtc spectrum of germanium in GeO_2 exhibits three separated peaks (Figure 5.2). The Kβ_5 feature around 11073 eV arises from the forbidden Ge 3s $\rightarrow$ 1s transition and the Kβ_2 peak around 11095 eV originates from the mixed Ge 4p, 4s $\rightarrow$ 1s transition. Around 11080 eV to 11082 eV the Kβ'' feature arises from transitions from mixed oxygen 2s with Ge 4p orbitals, for which the oxygen 2s binding energy becomes visible in the Ge 1s emission spectrum. The amplitude or intensity of the Kβ'' peak is connected to the cation ligand hybridization and is directly sensitive to changes in the distance between the Ge and O atoms.

[21] https://molview.org
[22] https://www.quantum-espresso.org

5.1.2 Compression of Amorphous GeO_2

Under ambient conditions, a-GeO_2 displays tetrahedral coordination, like q-GeO_2. Applying pressure up to 5 GPa change the inter-tetrahedral angle which allows compaction. Higher pressures from 5 GPa up to 20 GPa changes the structure from a four-fold to a six-fold coordination[65][14][52][94]. This coordination number change is accompanied by an increase of Ge-O bond distance. As long as the coordination number is preserved, the mean bond distance in GeO_2 decreases with increasing pressure. The coordination of GeO_2 for pressures above 40 GPa is still unchartered territory. A recent study interpreted their data as due to an increase in towards a 7-fold coordinated Ge ion, while an ab-initio MD study suggests a coordination change beyond six-fold only for pressures above 80 GPa[65][35].

5.2 Experimental Setup

The experiments were performed at beamline P01 of PETRA III. We used the primary fixed-exit DCM Si(111) monochromator at 12.5 keV incoming energy, and about 10^{13} photons per second incident on the sample. The beam was focused via KB-optics down to 7x15 VxH μm^2 size at the sample position. The vtc X-ray emission was measured by the von Hámos spectrometer placed at 90° with regard to the incoming X-ray beam. We used 8 Si(660) crystals in two columns, set at a mean Bragg angle of about 61.6°, thus covering an energy range of about 260 eV (10930 to 11190 eV),and recorded with a Pilatus 100k detector. The signal from each crystal was separated onto an 8 individual ROI to increase the energy resolution. The detector threshold was set to 5000 eV. With the pixel size of the detector being 172 micron, we yield an energy range of 700 meV per pixel. The elastic lines were recorded at the Si(880) reflection, in average the width of each elastic line was 2.5 eV. Accounting for the energy resolution of the incoming beam, we estimate the resolution of the spectrometer to be around 1 eV at 12.5 keV. Summing up, the signals from all 8 crystals reduced the collection time to 20 minutes per spectrum.

Three samples were measured: a-GeO_2, q-GeO_2 and r-GeO_2. We used panoramic diamond anvil cells with a radial opening at 90°, with regards to the incoming beam. In order to reduce the size of the indentation wall on the gasket material, for each cell the diamonds we used culets with two different sizes, 400 and 300 μm. By reducing the indentation wall, the emission signal, which was collected from the side opening, could be collected over a larger solid angle. The sample chamber between the diamonds was fully filled with sample powder. The pressure inside the cell was measured via ruby fluorescence[71]. We estimate the error on the pressure measurement to be around 1 GPa.

In addition, we measured crystalline Ge(0) at ambient conditions.

5.3 Valence-to-core XES of Crystalline GeO_2

We measured the valence-to-core spectrum of Germanium of crystalline GeO_2 in rutile structure (i.e. octahedrally coordinated) as well as in quartz structure (tetrahedrally coordinated). The spectra are shown in Figure 5.2 together with that of solid Ge for comparison. For both types of GeO_2, the measured spectra show equal energy for the lowest

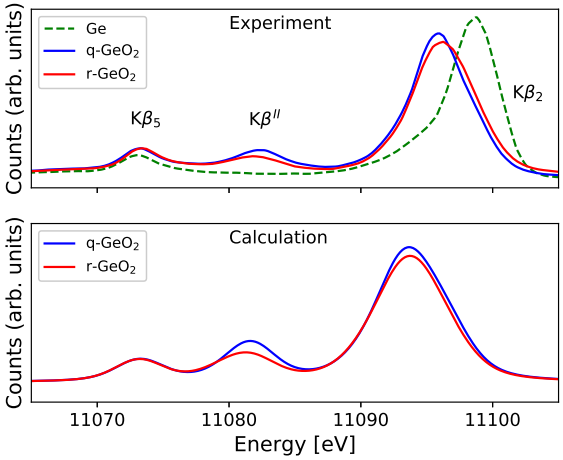

Figure 5.2: Valence-to-core emission spectrum of q-GeO_2, r-GeO_2 as well as crystalline Ge(0).

energy Kβ_5 emission line, shifted by less than 0.1 eV compared to crystalline Ge(0). This can be explained by the stronger localization of the 3d bond to Ge. Due to its constant intensity and energy, we use Kβ_5 for intensity normalization and express the changes of the Kβ'' emission line relative to it. We use two parameters ΔE and R_I to describe the observed changes in Kβ''. ΔE is defined as the splitting energy

$$\Delta E = E(K\beta'') - E(K\beta_5),$$

and is thus a measure of the energetic shift of the energy of the Kβ'' emission line. R_I is defined as the ratio of the intensities I of both peaks

$$R_I = \frac{I(K\beta'')}{I(K\beta_5)},$$

and is a measure of the Kβ'') intensity. Uncompressed crystalline samples already show a significant change in the Kβ'' for the two different coordination types. Here, also the different bond distances affect the Kβ'') intensity for both systems. To unravel the in-

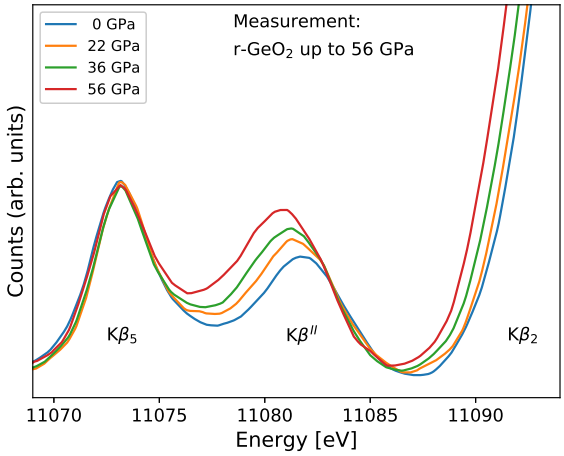

Figure 5.3: Valence-to-core X-ray emission spectrum of r-GeO_2 at ambient conditions and compressed up to 56 GPa. While increasing pressure, the Kβ'' shifts towards lower energy, while gaining intensity.

fluence of each parameter, coordination number and bond distance, we compressed the crystalline samples (Figure 5.3). Both R_I and ΔE follow a linear trend, as shown in Figure 5.4 and Figure 5.5. Only data points up to 5 GPa are available for q-GeO_2, since it is not stable at higher pressures. In order to extend the range to higher pressures, we simulated the behavior of q-GeO_2 at above 5 GPa. With this data for crystalline q-GeO_2 and

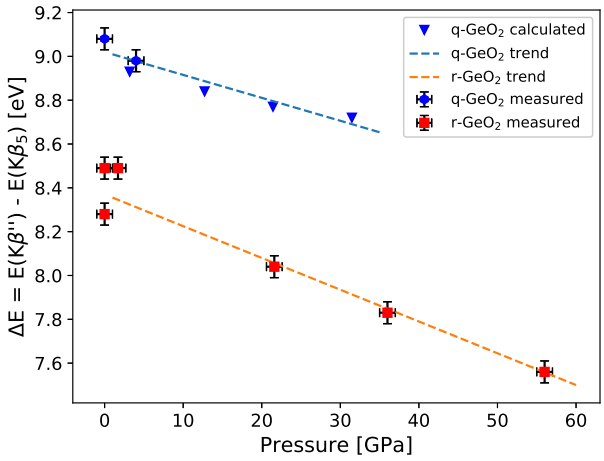

Figure 5.4: Energetic shift of the Kβ'' emission line relative to Kβ_5, expressed as ΔE, plotted as a function of pressure for four- and six-fold coordination. Overall the four-fold coordination of q-GeO_2 leads to a bigger shift in energy for all pressures. Both coordinations show well-distinguishable linear trends.

r-GeO_2 at different pressures (Figure 5.4), we extract a clearly separated linear behavior for ΔE as function of the applied pressure for four and six-fold coordination, which is displayed in Figure 5.4. From the same data, we obtain the behavior of R_I as a function

of the pressure for four and six-fold coordinated GeO_2. In the crystalline reference structures the relation between bond distance and pressure is known. The result is shown in

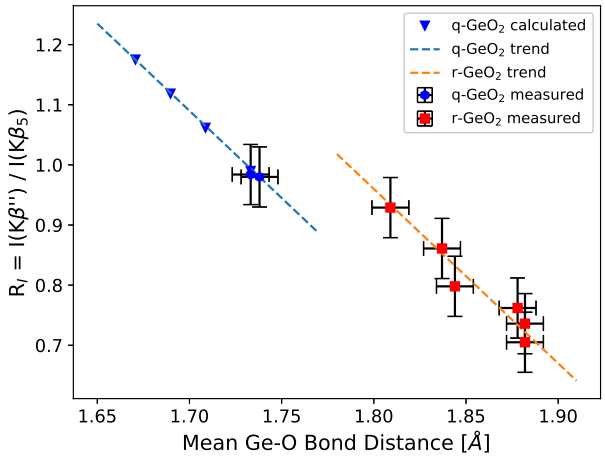

Figure 5.5: Intensity change of the Kβ'' emission line, expressed as R_I, plotted as a function of bond distance for four- and six-fold coordination, both show well-distinguishable linear trends.

Figure 5.5, where R_I is plotted in dependence on the bond distance.

5.4 Valence-to-Core XES of Amorphous GeO_2

We compressed a-GeO_2 up to 40 GPa in order to track the behavior of the Kβ'' emission line in a system that undergoes a coordination change from four to six-fold (Figure 5.6). From the measurements, we extract the energy shifts ΔE and add the data to the plot of the crystalline measurements, shown in Figure 5.4 and the result is shown in Figure 5.7. At pressures below 5 GPa, a-GeO_2 is close to the four-fold trend deduced from q-GeO_2 measurements. Increasing the pressure of a-GeO_2 up to 20 GPa, ΔE of a-GeO_2 approaches the trendline of six-fold coordinated r-GeO_2, and starts to match with it for pressures higher than 20 GPa.
Together with the trends from four and six-fold crystalline samples, we can assign a coordination number to each pressure point. The result is shown in Figure 5.8. The extracted intensity ratio R_I was plotted together with the crystalline measurements in Figure 5.9. The transition from four to six-fold coordination was fitted to the data points.

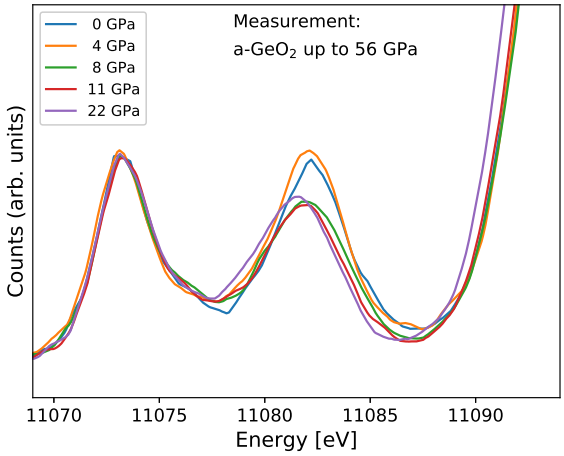

Figure 5.6: Valence-to-core emission spectrum of a-GeO_2 pressurized up to 40 GPa. The intensity of Kβ'' drops significantly between 4 and 8 GPA, indicating a structural transition.

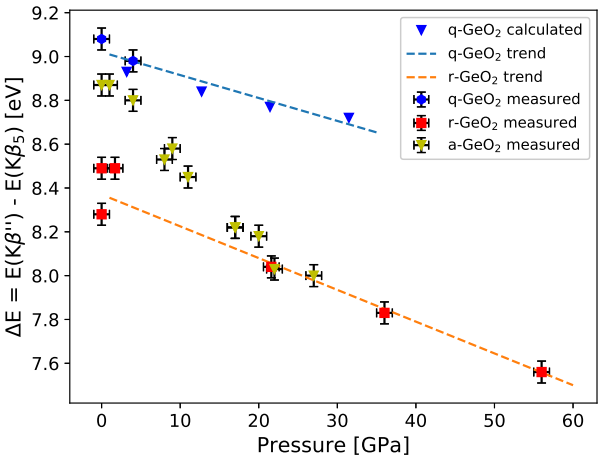

Figure 5.7: Energetic shift of the Kβ'' emission line relative to Kβ_5, extracted from a-GeO_2, plotted with the crystalline data and trends introduced in Figure 5.4, in order to show the sensitivity of valence-to-core XES to the structural transition from four- to six-fold.

5.5 Conclusion

By showing that valence-to-core emission is sensitive to changes in coordination and bond distance, we found a novel approach to investigate these quantities in amorphous material. For GeO_2 up to 40 GPa, our results are in agreement with the currently used techniques, XRD and EXAFS. Even though it requires more photons than XRD and EXAFS, there are cases when these techniques can not be used. For example, in strongly diluted or multicomponent samples the information gained by XRD or XDS may not

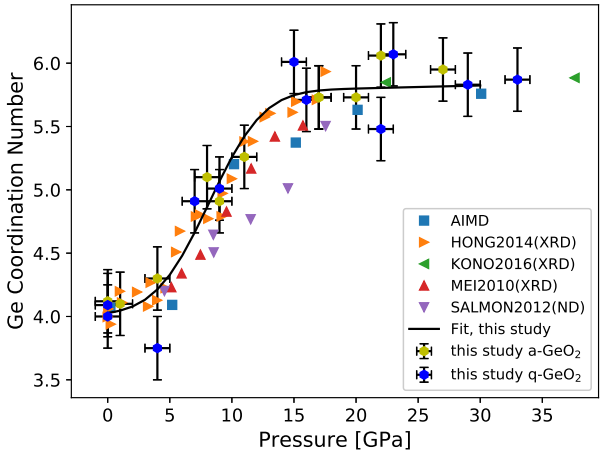

Figure 5.8: Showing measured and literature data for the coordination number as a function of pressure in compressed a-GeO_2. Coordination was refined by the values of ΔE and measurement of crystalline samples[65][94][52][77][35].

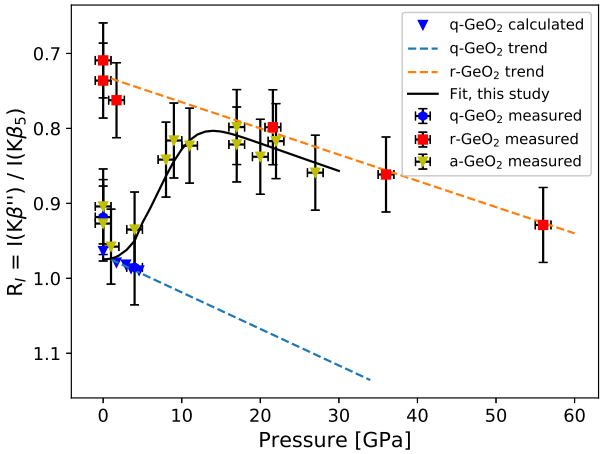

Figure 5.9: R_I as function of pressure, calculated for crystalline references (top), and measured (bottom) for crystalline references and a-GeO_2. One can see a-GeO_2 following the trend for q-GeO_2 at low pressures, then slowly changing towards r-GeO_2 trend when increasing the pressure. Beyond 20 Gpa it follows the r-GeO_2 trends.

give sufficient information. EXAFS requires scanning the incoming energy, for most lab sources this is not possible. To promote the capabilities of valence-to-core spectroscopy, future studies that test this technique for other elements are highly recommended. In addition, this effect should be investigated in liquids and the influence of the second coordination sphere should be determined. In a study with geophysical focus[102], we already applied this technique to track the coordination of a-GeO_2 up to about 100 GPa and found evidence that its structure remains six-fold coordinated, contrary to a recent study[65] that suggested seven-fold coordination.

6 Time-Resolved XANES of Weakly Absorbing Cobalt Samples

In this chapter, we present two case studies, where we used a newly developed setup to extend the capabilities of picosecond time-resolved hard X-ray absorption spectroscopy. These two cases describe the investigation of the optical excitations of weakly absorbing cobalt complexes, these measurements were enabled by using a digitizer, which is able to count up to 1000 times more photons than the regular setups using single photon counting APDs[29]. Producing solar fuels with photoexcited molecular assemblies of low-Z transition metal complexes (TMC) is a promising avenue, which is being intensively investigated. In particular, cobalt-based TMC constitute a growing family of catalysts capable of driving fundamental chemical reactions when combined with other photosensitizers [89][81]. The limited turnover numbers demonstrated by such homogeneous mixtures have been ascribed to the rapid degradation of both units. This difficulty could be largely circumvented if Co-TMC could act simultaneously as photosensitizers and catalysts. However, only few studies have been reported, where photosensitizing Co-TMC could be used in electron transfer (ET) reactions. This is due to the fact that their photophysics are insufficiently understood: The weak and featureless transient optical signals of the short-lived excited species observed in the UV-visible region are difficult to detect and to interpret. We measured the dynamics after optical excitation (which we will explain shortly in the coming section) of $[Co(III)(CN)_6]^{3-}$ and $[Co(III)(en)_3]^{3+}$ in aqueous solution. We did static optical spectroscopy and compare it to published optical measurements to identify the possible excitations and excited state dynamics. By performing XANES measurements of the cobalt K-edge around 7.7 keV, we track the changes element-specifically. The picosecond time-resolved measurements were done at PETRA III, beamline P01 and APS, beamline 7ID-D. In addition to the literature we also compare both complexes with iso-electronic iron complexes, $[Fe(II)(CN)_6]^{4-}$ and $[Fe(II)(bpy)_3]^{2+}$, which have been studied before[12][27][114]. The measured XANES spectra are used to reconstruct the spectra of the excited states.

6.1 Electronic Structure and Photo-Physics of 3d-Transition Metal Complexes

Ligand field theory (LFT) provides the theoretical background which is required to understand 3d-complexes, which in our case consist of one core metal surrounded by the

organic ligands[17]. LFT describes the interaction of the core metal electrons with the ligand electrons. The most important effect on the electronic structure of the core metal of a 3d-complex system is the broken degeneracy of the 3d-orbitals. The term broken degeneracy describes the energetic splitting of orbitals. As suggested by the crystal field theory, the different factors having an impact on the broken degeneracy are the metallic oxidation state and its coordination number, the arrangement of the atoms or molecules surrounding the 3d-metal. The ligand field theory extends the crystal field theory by molecular orbital theory and can for example describe overlapping orbitals, e.g. covalent bonding in complexes, which crystal field theory can not.

6.1.1 Optical Electronic Excitations of 3d-Complexes

Next to the typical inner-atomic electronic transitions, in complexes there are additional valence electronic excitations possible, leading to different electronic configurations. Figure 6.1 shows relevant electronic configurations occurring in the 3d orbitals of our samples. Possible valence electronic excitations are dd-excitations as well as ligand-to-metal charge transfer(LMCT) and metal-to-ligand charge transfer(MLCT). It is worth mentioning, that vibrations between the different bonds can change the probability of certain transitions. Additionally, temperature and in liquid samples the solvent, affect the probability of the excitation[48][31]. These excitations and their intensity can directly be probed with UV/Vis spectroscopy, a spectroscopic technique, where the sample's absorption of photons with 200-800 nm wavelength is measured[36]. Figure 6.2 shows the UV/Vis-spectrum of [Fe(II)(bpy)$_3$]$^{2+}$ in aqueous solution. In this section, we will explain the relevant excitations, the mechanics behind them and the relaxation processes.

dd Excitations, LMCT and MLCT

Excitations within the 3d-metallic orbitals (dd excitations) are forbidden in symmetric complexes including octahedral coordination[113]. However, due to small distortions, they can become possible, yet they are weak compared to other transitions or for dd excitations in tetrahedrally coordinated complexes[59]. MLCT is allowed due to an electron being excited from the metal 3s- or 4s-orbital to an empty ligand 2p-orbital. Vice versa, LMCT describes the effect when a ligand 2p-electron gets excited to a metal 3d-orbital.

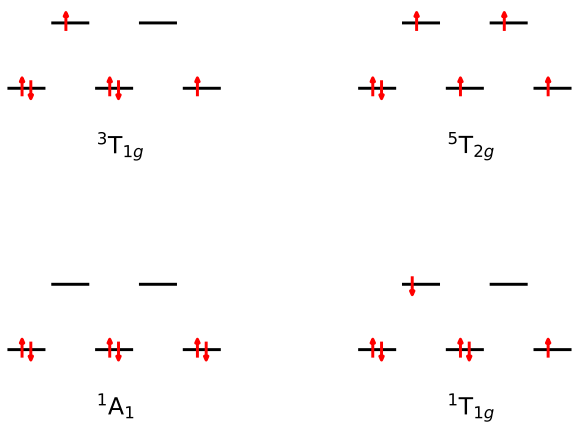

Figure 6.1: Overview of four possible electronic configurations of the d-orbitals in a 3d-complex. Each black bar represents one of the five 3-d orbitals stemming from the magnetic quantum number m. For our samples, the three lower-lying d_{xy}, d_{xz} and d_{yz} orbitals (also referred to as t_{2g}) are closer to the metal in octahedral symmetry and therefore lower in energy. The two d_{z^2} and $d_{x^2-y^2}$ orbitals (also referred to as e_g) are higher in energy. The red arrows indicate the electrons, obeying Pauli's principle. Due to the energetic splitting, Hund's rule is broken, leading to a low-spin $^1A_1$ being the ground state and the high-spin $^5T_{2g}$ state being highest in energy[34].

Vibrational States and Vibronic Coupling

In systems with more than one atom, vibration between the atoms occurs. These vibrational modes form a new sort of excited state. They are in general energetically lower than excited electronic states. A single photon can induce a combined vibrational and electronic excitation, this process is referred to as vibronic coupling. For vibronic coupling, the electronic transition takes place much faster than the change in vibration (Franck-Condon principle)[51]. Figure 6.3 shows the general Franck-Condon diagram, which shows that only certain vibrational levels can be excited. The probability of an electronic transition happening is much higher when the wave function of the vibrational modes overlap.

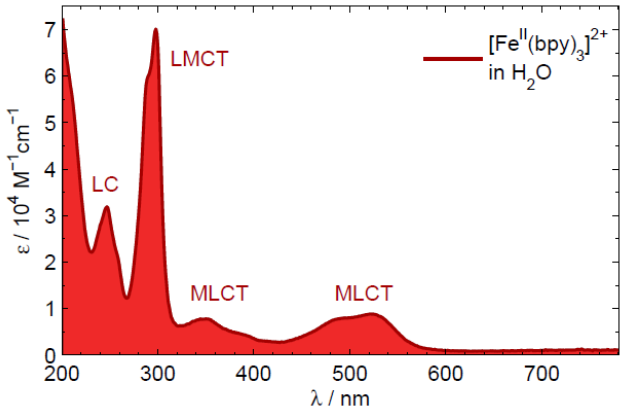

Figure 6.2: UV/Vis-spectrum of $[Fe(II)(bpy)_3]^{2+}$, showing different possible excitations in the optical regime[28].

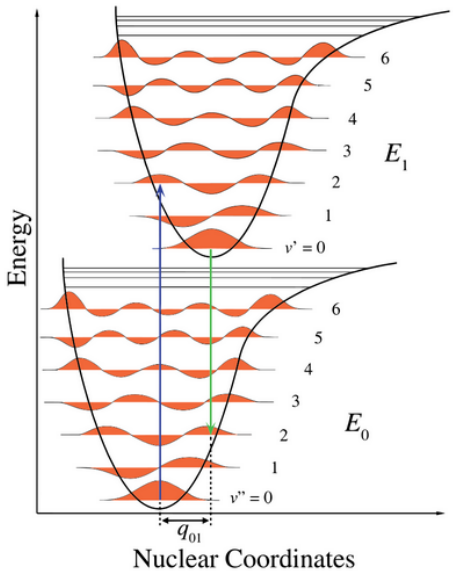

Figure 6.3: Franck-Condon energy diagram, with $v'' = 0$ ... $v'' = 6$ the vibrational states of the electronic ground state and $v' = 0$ ... $v' = 6$ the vibrational states of the electronic excited state. Suggesting that transitions between states are preferred by vibronic coupling, when the wave function of the vibrational modes overlap and suppressed when they do not overlap[7].

Relaxation Mechanisms

Following an excitation, there are different channels for the usually unstable excited state to relax into a stable state. These stable states do not necessarily have to be the initial ground state, but can also be new molecules. This can be the desired effect in photocatalytic reactions, but also undesired reactions like sample degradation and beam damage can occur. The relaxation pathway can include internal conversion, (delayed) fluorescence, non-radiative relaxation, intersystem crossing and phosphorescence, each happening at an individual time scale, down to sub-femtosecond[95][107].

6.2 Co(III)(en)$_3$

We measured octahedrally coordinated Co(III)(en)$_3$ in aqueous solution. (en) stands for ethylenediaminem, $C_2H_4(NH_2)_2$, an organic compound. This complex has been studied before using [Co(III)(en)$_3$](ClO$_4$)$_3$ in aqueous solution[76]. Its ground state is a low-spin $^1A_1$ state. Based on iso-electronic Fe(II) references it was proposed that the metastable state following photo-excitation to be the $^5T_{2g}$ quintet high-spin state. However no clear proof was given in the reference. The goal of this section is to establish unambiguously for the first time the exact nature of the metastable state created upon photo-excitation in the visible range.

The sample was bought from Sigma-Aldrich as tris(ethylenediamine)cobalt(III) chloride dihydrate, an orange powder. For the measurements, a 20 mM aqueous solution was prepared by solving the powder in Milli-Q[23] water. The solution has a yellow color. Figure 6.4 shows the structure of [Co(III)(en)$_3$]$^{3+}$ (rendered with Molview[24]). First, we

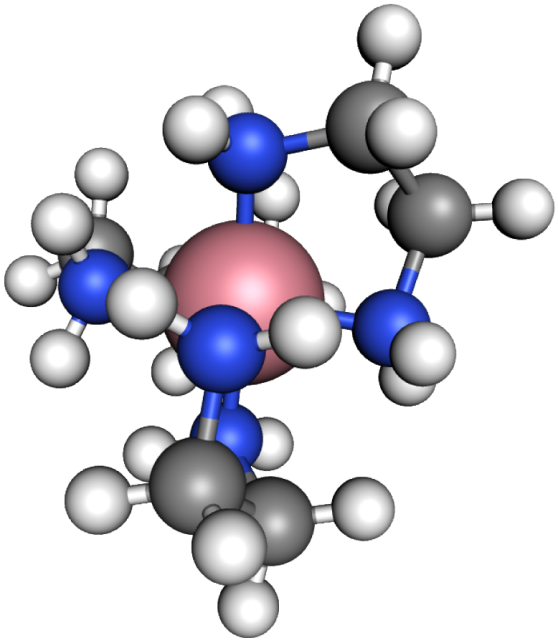

Figure 6.4: Structure of [Co(III)(en)$_3$]$^{3+}$, a complex in octahedral coordination. The central Co atom is surrounded by three (ethylenediaminem) molecules.

performed ultraviolet and visible spectroscopy (UV/Vis) to record the optical excitations. In addition, we used UV/Vis spectroscopy before and after the measurements to ensure that the sample did not degrade during the experiment. In the second step, we performed time-resolved picosecond optical pump X-ray probe XANES around the cobalt K-edge at 7710 eV. The K-edge XANES spectra yield information about the electronic states follow-

[23] https://www.merckmillipore.com/DE/de/products/water-purification/type-1/5cSb.qB.89EAAAFAJqxkiQpx,nav

[24] https://molview.org

Table 6.1: Experimental details of our Co(III)$(en)_3$ experiment.

Synchrotron / experimental station	Beamline P01, PETRA III		
X-ray flux on sample per second	10^{13}	10^{13}	10^{13}
Energy range in eV	7700-7750	7700-7750	7700-7780
X-ray focus size (HxV) in μm^2	10x10	10x10	10x10
Monochromator	Si(111)	Si(111)	Si(111)
Energy resolution in eV	1.2	1.2	1.2
Electron bunches in ring	40	40	40
X-ray repetition rate in MHz	5.2	5.2	5.2
Sample	Co(III)$(en)_3Cl_3$ in aqueous solution		
Sample concentration in mM	20	20	20
Sample amount in ml	50	50	50
Sample thickness in μm	140	140	140
Jet speed in m/s	5	5	5
Laser system	Tangerine		
Laser wavelength in nm	257	343	515
Laser focus size (HxV) in μm^2	24x18	25x25	35x30
Laser power in mW	40	140	650
Repetition rate in kHz	131	131	131
Energy per pulse in nJ	300	1050	4880
Pulse width in ps	0.35	0.35	0.35
Exctinction coeff. in cm^{-1}M^{-1}	300	91	28
ESF (estimated) in %	9.4	9.8	12.8

ing photo-excitation, which are attributed to the electronic and geometric changes of the sample. For the conclusion, we compare our results with similar time-resolved XANES measurements of the isoelectronic compound [Fe(II)$(bpy)_3]^{2+}$, taken under same conditions. These measurements were presented shortly in chapter 2 and chapter 3.

Table 6.1 shows the experimental parameters of our measurements. To calculate the excited state fraction (ESF), we first calculate the fraction of absorbed optical photons A at a certain wavelength λ via:

$$A(\lambda) = 1 - 10^{-dc\epsilon(\lambda)},$$

with d the jet thickness, c the molar concentration and $\epsilon(\lambda)$ the extinction coefficient at wavelength λ, which was measured via UV/Vis spectroscopy, shown in the next section. Combined with the energy per laser pulse E_{pulse} and the optical photon energy E_γ, we

can calculate the amount of photons used for excitation $N_{\gamma,exc}$ by

$$N_{\gamma,exc} = A * \frac{E_{pulse}}{E_{\gamma}}.$$

The total amount of sample molecules N_{sample} in the laser spot can be calculated via:

$$N_{sample} = N_A c_i k d,$$

with k the laser focus spot size, N_A = 6.022*10^{23} mol^{-1} the Avogadro constant, c_i the molar concentration and d the jet thickness. Finally we, receive an estimate for the excited state fraction (ESF) in the laser spot by dividing the absorbed photons used for excitation $N_{\gamma,exc}$ by the total number of sample molecules in the laser spot N_{sample}:

$$ESF = \frac{N_{\gamma,exc}}{N_{sample}}.$$

Since the X-ray focus is smaller than the optical focus, the excited state fraction seen by the X-rays is assumed to be the same.

6.2.1 Optical Excitations and Excited State Dynamics

To identify possible excitations, we measured the optical spectrum of [Co(III)(en)$_3$]$^{3+}$ in aqueous solution, shown in Figure 6.5. The measured spectrum is in good agreement

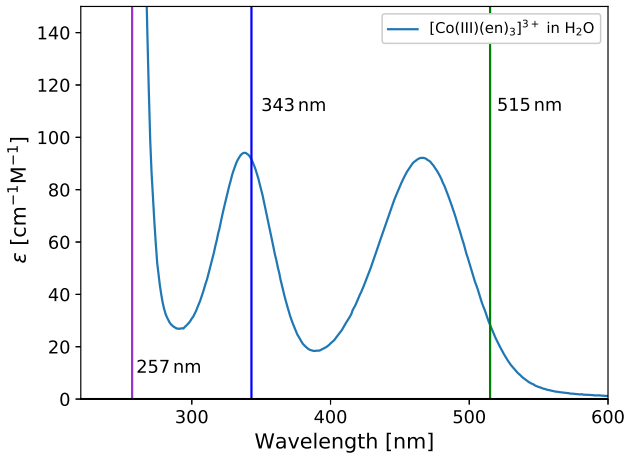

Figure 6.5: Optical spectrum of [Co(III)(en)$_3$]$^{3+}$. The vertical lines represent the excitation wavelengths of our laser system, which were used to access the optical excitations.

with [76]. The excitation peaks were assigned according to their conclusions. The absorption band at 466 nm is attributed to the $^1T_{1g} \leftarrow {}^1A_1$ transition, while the peak at

340 nm is attributed to the $^1T_{2g} \leftarrow {}^1A_1$ transition. The third band at 212 nm is assigned as ^{1}LMCT$\leftarrow {}^1A_1$. . Concluding from the peak assignment done with the UV/Vis, this means that after photo-excitation at 515 and 343 nm, the system undergoes vibrational transition from the $^1A_1$ ground state to the $^1T_{2g}$ and $^1T_{1g}$ ligand field state, respectively. Following photo-excitation at 257 nm, the system undergoes transition from the $^1A_1$ ground state to the ^{1}LMCT state. These states decay within τ = 1-2 ps non-radiatively into the lowest-lying excited state, which has been proposed to be the $^5T_{2g}$ state. Although this high-spin $^5T_{2g}$ has been proposed as plausible by analogy with related Co(III) complexes, a definite experimental proof is still lacking to date [76]. Therefore, the metastable was probed with XAS in order to extract its electronic and geometric structure. The lowest-lying excited state has a lifetime of about 450 $\pm$ 100 ps in aqueous solution, before it decays into the $^1A_1$ ground state, hence it is perfectly suited to be studied at a synchrotron radiation source with a time resolution of around 100 ps.

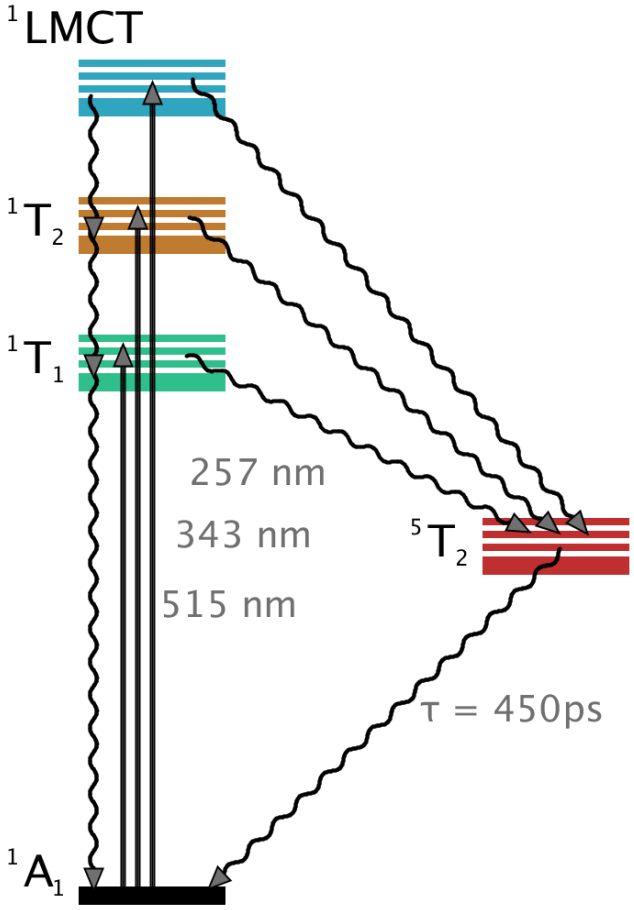

Figure 6.6: Excited state dynamics of $[Co(III)(en)_3]^{3+}$ after excitation at 257, 343 and 515 nm, as proposed by [76]. Detailed description can be found in the text.

Figure 6.6 shows the Jablonski-diagram displaying the proposed dynamics.

6.2.2 K-edge XANES

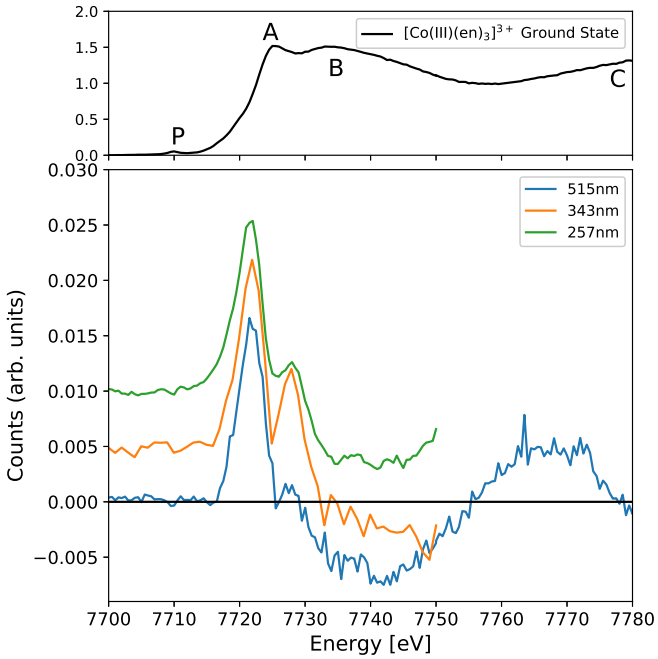

Figure 6.7: XANES spectrum of the [Co(III)(en)$_3$]$^{3+}$ ground state (top) as well as the transient about 100 ps after laser excitation at 257, 343 and 515 nm (bottom). Data was taken at BL P01, PETRA III.

The XANES measurements after excitation at 257 nm, 343 nm and 515 nm were performed at beamline P01 of PETRA III. The experimental details are described in Table 6.1, for a more detailed description of beamline P01 see chapter 3. Figure 6.7 shows the ground state spectrum and transient XANES spectra of [Co(III)(en)$_3$]$^{3+}$ at 257, 343 as well as 515 nm with a vertical offset. The shown ground state spectrum was recorded during the 515 nm measurements. In the ground state a small pre-edge feature (P) can be observed at 7710 eV, this feature is assigned to the 1s $\leftarrow$ 3d transition. The XANES region is characterized by an intense white line (A) and a multiple scattering feature (B) around 7735 eV. The EXAFS region is characterized by a broad oscillating feature (C) around 7770 eV. Considering the fact that Co(III) d^6 complexes are isoelectronic to Fe(II) d^6 complexes, these transients are compared with the one obtained for [Fe(II)(bpy)$_3$]$^{2+}$, as shown in Figure 1.5. For this comparison, in order to match the energy scale of cobalt, the energy of [Fe(II)(bpy)$_3$]$^{2+}$ was stretched with a factor of 7709/7112. This factor corresponds to the binding energies of the K 1s electrons of elemental iron and cobalt. The very close resemblance between the traces allows concluding that the metastable state is, as in the iron case, indeed the $^5T_{2g}$ state, with a Co-N bond length elongation[114][30][46]. Based on our calculations of the ESF presented in Table 6.1, we can reconstruct the XANES spectrum of the $^5T_{2g}$ excited state (ES) using the ground state spectrum (OFF)

and the spectrum measured after excitation (ON) via the following formula:

$$ES = \frac{ON - (OFF(1 - ESF))}{ESF}$$

Due to the X-ray beam probing the sample about 100 ps after excitation, the estimated ESF shown in Table 6.1 have been lowered by 20% before being used for the reconstruction. The new ESF are 7.5% for 257 nm, 7.8% for 343 nm as well as 10.2% for 515 nm. The reconstructed spectra for the different wavelengths are shown in Figure 6.9.

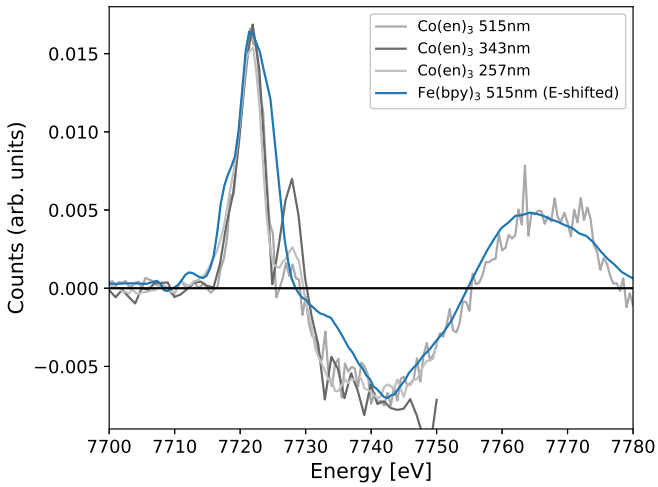

Figure 6.8: XANES spectrum of $[Co(III)(en)_3]^{3+}$ and $[Fe(II)(bpy)_3]^{2+}$ done at BL P01, PETRA III.

6.2.3 Conclusion and Outlook

Time-resolved XANES on the 100 ps time scale at beamline P01 of PETRA III has allowed establishing experimentally for the first time that the metastable state populated upon photoexcitation is a high-spin $^5T_{2g}$ state. Using our data, we reconstructed a XANES spectrum of the excited state. Future experiments at XFEL sources will investigate the electronic cascade that leads to the $^5T_{2g}$ formation, taking place over the first few ps upon excitation.

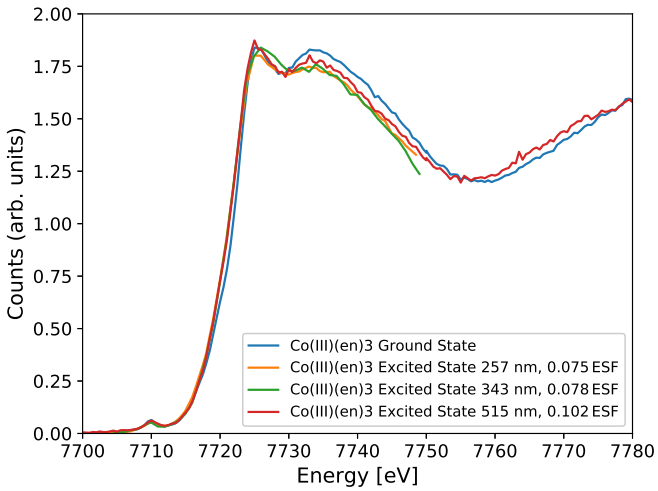

Figure 6.9: XANES spectrum of [Co(III)(en)$_3$]$^{3+}$ ground state and reconstructed $^5T_{2g}$ excited state, reconstructed with data obtained 100 ps after 257, 343 and 515 nm photo-excitation.

6.3 Co(III)$(CN)_6$

We measured octahedrally coordinated Co(III)$(CN)_6$ in aqueous solution in the course of two independent experiments. The solutions were prepared by solving $K_3Co(CN)_6$, ordered from Sigma-Aldrich, in Milli-Q water. An overview of the experimental details is shown in Table 6.2.

Table 6.2: Experimental details Co(III)$(CN)_6$

Synchrotron / experimental station	PETRA III / P01	APS / 7ID-D
X-ray flux on sample per second	10^{13}	10^{12}
Energy range in eV	7700-7800	7700-7750
X-ray focus size (HxV) in μm^2	20x10	20x10
Monochromator	Si(111)	Diamond(111)
Energy resolution in eV	1.2	0.4
Electron bunches in ring	40	24
X-ray repetition rate in MHz	5.2	6.5
Sample	$K_3Co(CN)_6$ in H_2O	
Sample concentration in mM	50	100
Sample amount in ml	200	200
Sample thickness in μm	140	140
Jet speed in m/s	5	5
Laser system	Tangerine	Duetto
Laser wavelength in nm	343	266
Laser focus size (HxV) in μm^2	20x20	25x25
Laser power in mW	40	560
Repetition rate in kHz	131	133
Energy per pulse in nJ	150	3750
Pulse width in ps	0.35	10
Exctinction coeff. in $cm^{-1}M^{-1}$	75	35
ESF (estimated) in %	9.4	63.8

Figure 6.10 shows the structure of $[Co(III)(CN)_6]^{3-}$, it also represents the $[Fe(II)(CN)6]^{4-}$ structure[25].

[25] Rendered https://molview.org

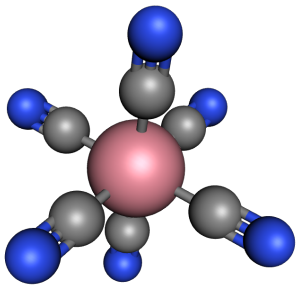

Figure 6.10: Structure of [Co(III)(CN)$_6$]$^{3-}$, a complex in octahedral coordination, the central Co atom is surrounded by six (CN)$^-$ molecules. It also represents the structure of [Fe(II)(CN)6]$^{4-}$.

6.3.1 Optical Excitations and Excited State Dynamics

We measured the optical spectrum of [Co(III)(CN)$_6$]$^{3-}$

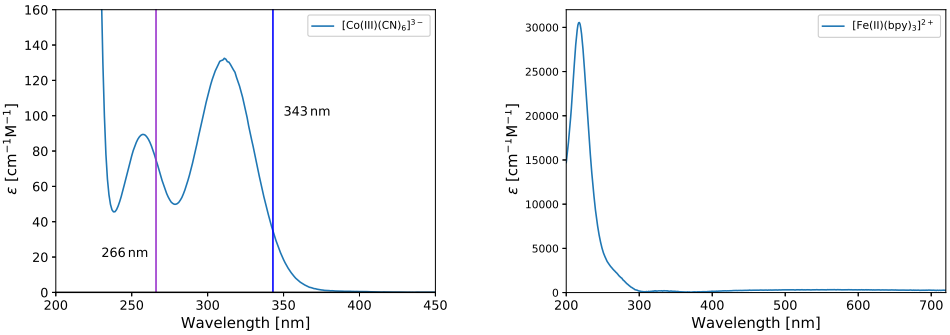

Figure 6.11: Optical spectrum of [Co(III)(CN)$_6$]$^{3-}$ and [Fe(II)(CN)6]$^{4-}$. The vertical lines represent the excitation wavelengths of our laser system, which were used to access the optical excitations.

Figure 6.11 shows the UV/Vis spectrum of [Co(III)(CN)$_6$]$^{3-}$, the excitation peaks and dynamics were assigned according to [78]. The absorption band at 313 nm is attributed to the $^1T_{1g} \leftarrow {}^1A_1$ transition, while the peak at 267 nm is attributed to the $^1T_{2g} \leftarrow {}^1A_1$ transition. We assigned the following intermediate states for the dynamics following the photo-excitation for [Co(III)(CN)$_6$]$^{3-}$. After photo-excitation at 267 or 343 nm, the system undergoes transition from the $^1A_1$ ground state to the $^1T_{2g}$ or $^1T_{1g}$ state, respectively. Both decay non-radiatively into the lowest-lying excited state, which has been identified as the $^3T_{1g}$ state. The $^3T_{1g}$ has a lifetime of 2.7 ns in aqueous solution[31]. It decays either

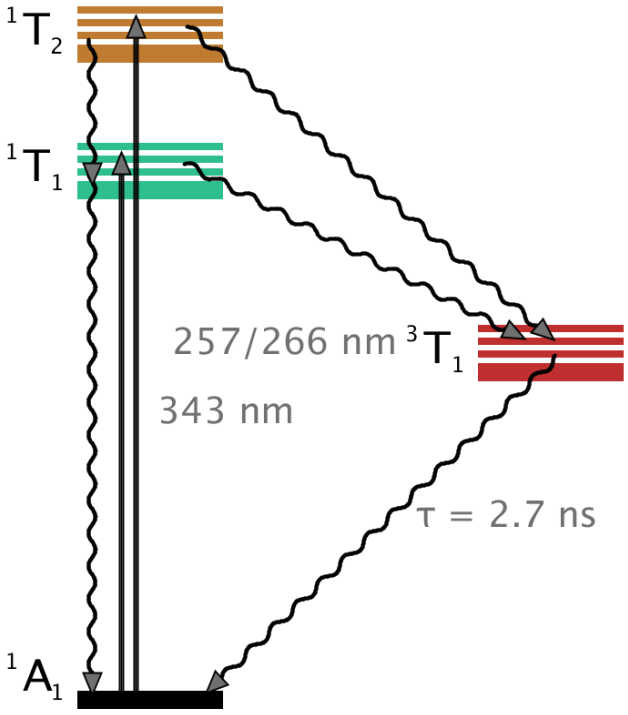

Figure 6.12: Excited state dynamics of $[Co(III)(CN)_6]^{3-}$ after 267 and 343 nm excitation. Detailed description can be found in the text.

directly into the $^1A_1$ ground state or can form the photoaquated $[Co(III)(CN)_5(H_2O)]^{2-}$ complex. The photoaquation yield is 0.31 for both excitation wavelengths[80][84]. We chose the iso-electronic reference $[Fe(II)(CN)6]^{4-}$, which has been well studied, allowing us to assign the excitations and dynamics[12]. $[Fe(II)(CN)_6]^{4-}$ has the same coordination and structure as $[Co(III)(CN)_6]^{3-}$. Figure 6.11 shows the UV/Vis spectrum of $[Fe(II)(CN)_6]^{4-}$ compound. The absorption band at 322 nm is attributed to the $^1T_{1g} \leftarrow {}^1A_1$ transition, while the peak at 270 nm is attributed to the $^1T_{2g} \leftarrow {}^1A_1$ transition. In addition, there is a $^1T_{1u} \leftarrow {}^1A_1$ MLCT transition. According to literature the important dynamics after photo-excitation for $[Fe(II)(CN)6]^{4-}$ are as follows. After photo-excitation at 267 or 355 nm, the system undergoes transition from the $^1A_1$ ground state to the $^1T_{2g}$ or $^1T_{1g}$ state, respectively. They both decay non-radiatively into the lowest-lying excited state, which has been identified as the $^3T_{1g}$ state. The $^3T_{1g}$ has a lifetime of 16 ps in aqueous solution. It decays either directly into the $^1A_1$ ground state or can form the photoaquated $[Fe(II)(CN)_5(H_2O)]^{2-}$ complex. The photoaquation yield is 0.31 for excitation at 355 nm. At 266 nm there is an additional excitation possible, the $^1T_{1u} \leftarrow {}^1A_1$ MLCT transition. This charge transfer results in the formation of $[Fe(III)(CN)6]^{3-}$. This additional photo-reaction lowers the photoaquation yield of 266 nm excitation to either 0.14 or 0.19.

6.3.2 K-edge XANES

Figure 6.13 shows the Co K-edge XANES spectrum of the $[Co(III)(CN)_6]^{3-}$ measured at 7ID-D and P01. Both spectra show the same features at the same energy, thus we expect the sample to be in the same condition at both measurements.

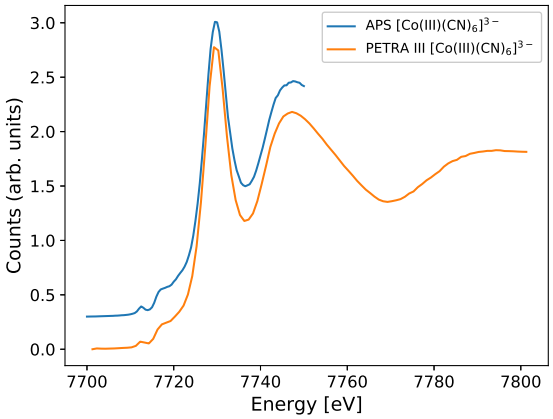

Figure 6.13: Ground state XANES of $[Co(III)(CN)_6]^{3-}$ measured at APS 7ID-D (blue, with offset) and PETRA III P01 (orange).

Measurements at 266 nm

The time-resolved XANES measurements of 266 nm were done at beamline 7ID-D of APS at low repetition rate, i.e. 133 kHz. The jet flow rate was about 5 m/s, so between two laser pulses the sample was completely refreshed. Figure 6.14 shows transient XANES spectra of $[Co(III)(CN)_6]^{3-}$ after 266 nm excitation. The second sample was prepared independently to check for degradation of the sample. The orange line shows the transient 100 ps after excitation, the green line shows the transient signal averaged over 10 bunches, starting from 153 ns to over 1.53 μs after the initial laser excitation. In general, all the transient signals indicate a red shift of the excited state XANES with regards to the ground state XANES. The delayed transient taken hundreds of ns after excitation shows two features in the pre-edge region. The transient taken 100 ps after excitation seems to reproduce the features in the pre-edge region, however, these features are weaker and almost buried in the statistical noise. The peak at the onset of the white line around 7725 eV is more pronounced in the 100 ps transient compared to the delayed transient.

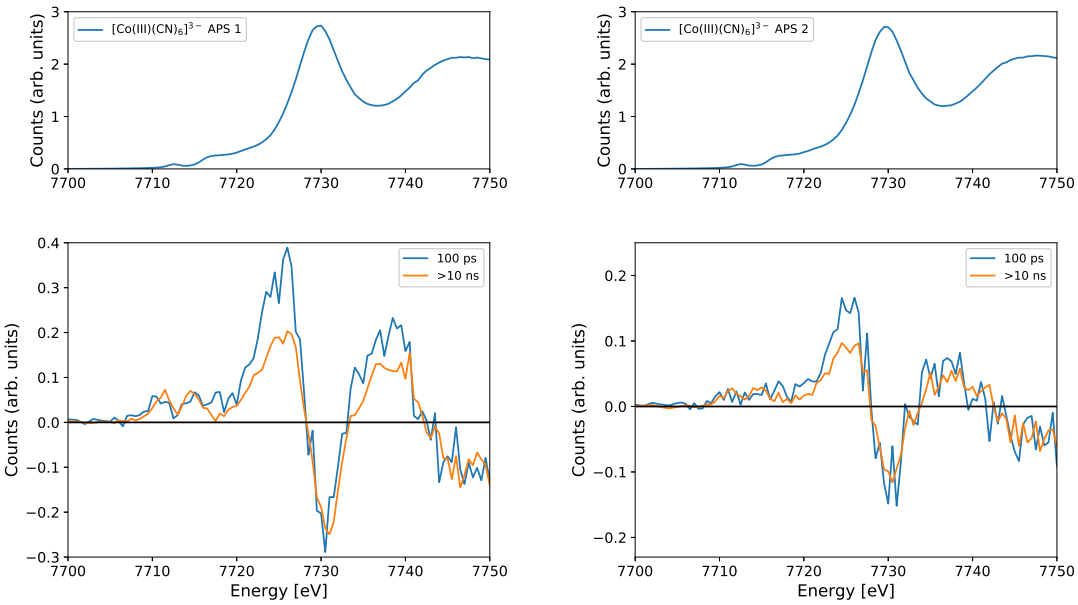

Figure 6.14: Transient XANES spectra of two independently prepared 100 mM solutions of $[Co(III)(CN)_6]^{3-}$ after photo-excitation at 266 nm. The spectra were measured at BL 7ID-D, APS.

Measurements at 343 nm

The 343 nm measurements were performed at beamline P01 of PETRA III with a laser repetition rate of 131 kHz. The jet flow rate of 5 m/s was fast enough to refresh the sample completely between two laser pulses.

Figure 6.15 shows the transient XANES spectrum of $[Co(III)(CN)_6]^{3-}$ after 343 nm excitation. There seems to be no feature in the pre-edge region and the peak around the onset of the white line is more pronounced compared to the 266 nm measurements.

Figure 6.16 shows a delay scan at 7725 eV to show the decay of the transient signal after 343 nm optical excitation of $[Co(III)(CN)_6]^{3-}$. The fit reproduces the lifetime of 2.6 ns of the $^3T_{1g}$ state.

Interpretation of XANES Data

The transient signals of the hexacyanocobaltate(III) in aqueous solution were measured at 266 nm and 343 nm show several differences. However, based on the literature and also regarding the equal photoaquation yields for 266 and 343 nm excitation, we do not expect a difference in the dynamics of the excited state for 266 and 343 nm within the 100 ps time resolution of our XANES measurements. However, there were two major differences in

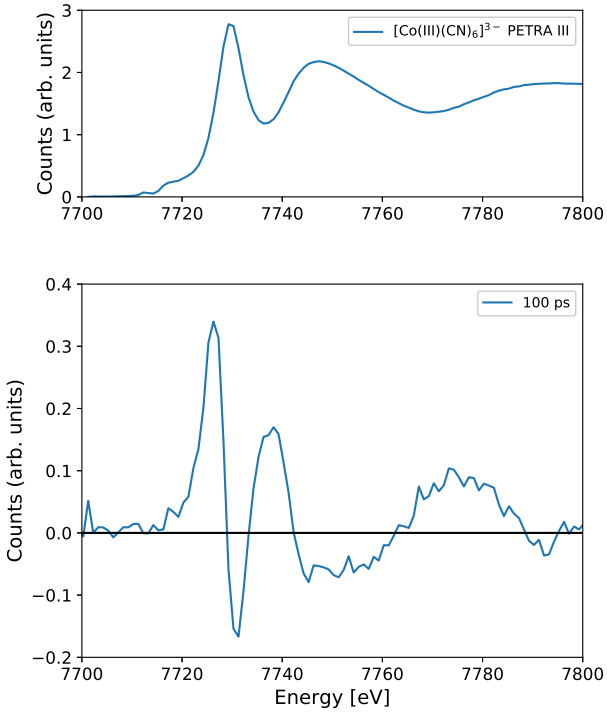

Figure 6.15: Ground state and transient XANES spectrum of [Co(III)(CN)$_6$]$^{3-}$ at Co K-edge after 343 nm excitation. Done at BL P01, PETRA III.

the setup of the experiments. First, the Duetto laser system used at APS has a much longer pulse length of 10 ps and in addition, the Duetto power was most likely chosen too high for a linear experiment. The interpretation of the 343 nm measurements performed at beamline P01 of PETRA seems to be straightforward. The laser excites about 1.7% of the cobalt molecules in the X-ray spot to the $^3T_{1g}$ lowest-lying excited state. At the time the X-ray beam probes the sample, about 100 ps after laser excitation, roughly 3% of the ex- cited molecules decayed back to the ground state and about 1% undergo photoaquation. This leads to a ratio of 82:1 between $^3T_{1g}$ and photoaquated molecules. This difference in concentration should be high enough to attribute the transient signal measured to be the $^3T_{1g}$ state. Thus, we should be able to reconstruct the XANES spectrum of this excited state. In the case of 266 nm measurements, the assignment seems to be more complicated. For [Fe(II)(CN)6]$^{4-}$, the two pre-edge features A and B of the transient have been assigned to be features of the photoaquated and the excited photoaquated complex[12]. If we adopt this assignment and assume hexacyanocobaltate(III) to behave similarly to hexacyanoferrate(II), this would mean we created both a photoaquated and the excited photoaquated complex within the 10 ps pulse. Another interpretation would be, that both peaks arise from the photoaquated complex. Considering the 2.6 ns lifetime of the $^3T_{1g}$ state, the spectrum taken hundreds of nanoseconds after photoexcitation, should consist of either pure photoaquated or a mixture of photoaquated and excited photoaquated complex. For the 100 ps transient at 266 nm, the possible occurrence of the A and B features indicates the formation of photoaquated complex and possibly its

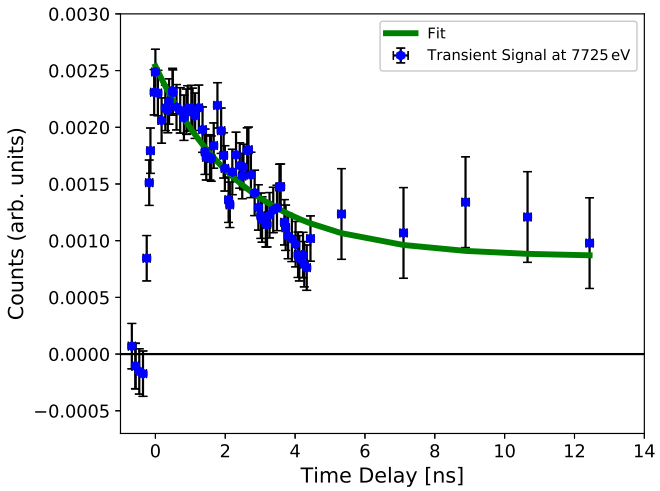

Figure 6.16: Delay scan of $[Co(III)(CN)_6]^{3-}$ at 7725 eV using 343 nm optical excitation. Measurements done at BL P01, PETRA III. The fit suggests a lifetime of 2.6 ns.

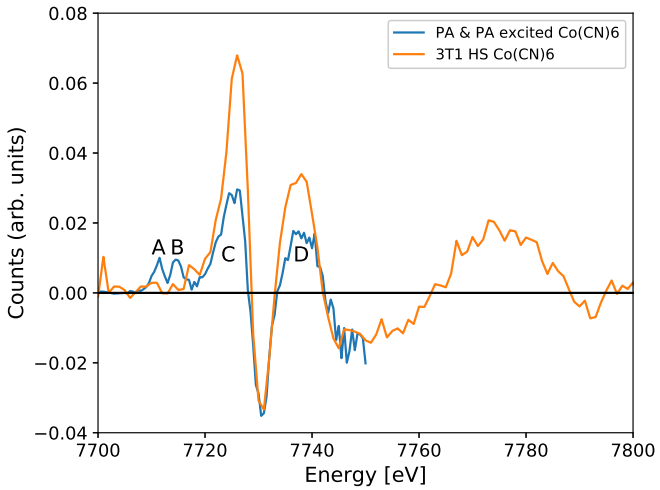

Figure 6.17: Transient XANES spectrum of $[Fe(II)(CN)6]^{4-}$ after 266 nm excitation, done at BL 7ID-D, APS.

excited state in addition to the $^3T_{1g}$ state. This is supported by the C and D features being less pronounced compared to in the 343 nm measurements, but still showing higher intensity compared to the delayed signal.

6.3.3 Conclusion

Photoexcitation of $[Co(III)(CN)_6]^{3-}$ in aqueous solution at 266 and 343 nm allowed time-resolved XANES measurements in the picosecond regime. With the measurements at 343 nm, we believe we found a transient signal that can be attributed to the $^3T_{1g}$ state. While the transients at 266 nm seem to be a mixture of different states, we could still

use them to identify the features of the photoaquated complex. The appearance of the peaks attributed to the photoaquated complex in the 266 nm measurements support that the transient measured at 343 nm can be fully attributed to the $^3T_{1g}$ lowest-lying excited state. As a final step, we used our data to reconstruct the XANES spectrum of the $^3T_{1g}$ state of [Co(III)(CN)$_6$]$^{3-}$, shown in Figure 6.18. In order to proceed with the investigation

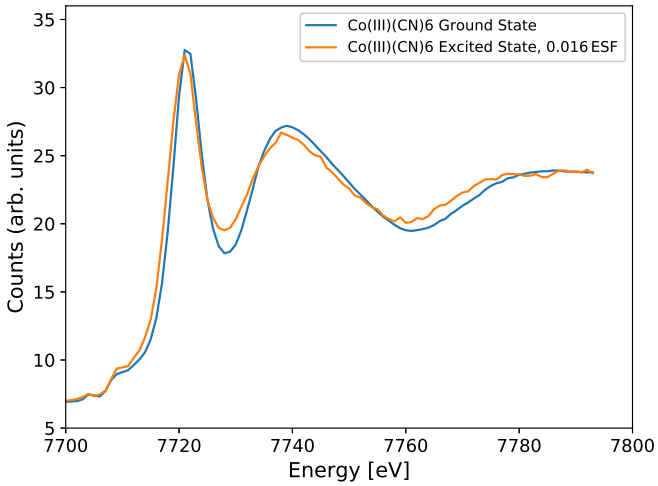

Figure 6.18: Ground state Co K-edge XANES spectrum of [Co(III)(CN)$_6$]$^{3-}$ and the corresponding reconstructed XANES spectrum of the excited state after 343 nm optical excitation, assuming an excited state fraction of 9.4%.

of the short-lived states below 100 ps, we would need the time resolution which an XFEL provides. Further investigation of the photoaquated complex can help resolve to what extent the excited photoaquated complex contributes to the changes in the pre-edge.

7 Conclusion and Outlook

A major part of this thesis is dedicated to the setup and measurements carried out with a sixteen-crystal large solid angle von Hámos X-Ray spectrometer, now in place at its final destination at the FXE end station of European XFEL. We give a detailed description of possible setups and crystal arrangements and how to extract and process the data collected with 2D-detectors. We present our commissioning measurements and the first results obtained with this simple to use, yet powerful secondary spectrometer. We introduced a set of formulas that describe the energy dispersion on the detector for single-crystal spectrometer configuration. These formulas are extended to the multi-crystal spectrometer configuration, where one can record the signals as separated spectra or overlap them into one spectrum. Using these formulas, we characterized the limits to the energy resolution when overlapping multiple crystals for background reduction. Additionally, we showed that a second-order polynomial fit reproduces the relation between detector position and energy with an accuracy of just a few meV.
The von Hámos spectrometer has successfully been employed to conduct measurements using a diverse set of X-ray spectroscopy techniques. We present measurements of the iron Kβ spectrum of $K_4Fe(CN)_6$ in 0.5 M aqueous solution, as a test case for overlapping and separated crystal setups, to further verify our methods for data extraction as well background treatment. Subsequently, we demonstrate the capabilities of the von Hámos spectrometer. Recording the iron Kβ emission of $Fe(bpy)_3$, we tracked the optically induced altering of the spin state on the picosecond scale. Using Si(220) and Si(111) crystals we were able to simultaneously measure Fe Kα, Kβ and vtc spectra of $Fe(terpy)_2$ with picosecond time resolution. Making use of the spectrometer's large solid angle, we achieved the first recording of picosecond time-resolved iron vtc spectra. We recorded RIXS maps around the iron K pre-edge region of $K_4Fe(CN)_6$ and $K_3Fe(CN)_6$ and present a PFY spectrum for these compounds. We recorded a RIXS map of 1 M $ZnBr_2$ Kα in aqueous solution, while simultaneously recording a TFY XAS spectrum. From the RIXS map, we extracted a PFY spectrum and compared it to the spectrum taken via TFY detection. We show the spectrometer's potential to perform IXS spectroscopy. We tested the spectrometer's ability to investigate valence-hole excitations by measuring the dynamic structure factor S(q,ω) of beryllium at low energy transfer. The large solid angle of the spectrometer allowed us to record spectra at different momentum transfers simultaneously. We investigated core-hole excitations by recording XRS spectra of beryllium at the Be K-edge and the carbon K-edge XRS of highly oriented pyrolytic graphite (HOPG), where we probed different orbitals by altering the sample orientation and making use of the polarization of the incoming X-rays. To gain an insight into the performance of the spectrometer for future experiments, we recorded the oxygen K-edge spectrum via XRS spectroscopy with the von Hámos spectrometer and compared it to spectra taken with

an XRS-spectrometer in Johann geometry as well as soft X-ray XAS data. These IXS tests give first insights into the needed setups and required data-acquisition times to perform time-resolved IXS experiments at storage rings and XFEL sources. These efforts would heavily be supported by detectors that can operate very close to the sample, to increase the solid angle per eV.

Concluding, the versatileness and simplicity of the spectrometer are perfectly suited to take on the challenges that arise when measuring at XFELs, especially since the von Hámos spectrometer can be set up to simultaneously accumulate data while measuring with other techniques, for example XRD, XDS or IXS[110][10]. This paves the way for new approaches with multi-messenger spectroscopic techniques. The next step is to extend the crystals available for the spectrometer to different materials with high Z elements to enable high resolution measurements with sufficient intensity at high X-ray energies. In addition, a greater variety of crystals emphasizes the simultaneous measurement of different elements.

Utilizing the von Hámos spectrometer to record Kβ emission, we tracked pressure-induced coordination and bond length changes for the first time using valence-to-core emission spectroscopy. We demonstrate this for the case of amorphous GeO_2, a compound with a well-understood coordination transition in the region below 20 GPa. As an element-specific spectroscopy method, recording the germanium Kβ emission allowed us to study the germanium and its first coordination shell. Confining the sample in a diamond anvil cell, we turned the pressure up to 40 GPa in several steps. This induced an increase from four- to six-fold coordination. Before the coordination change, the bond lengths between the germanium and its neighboring oxygens decreased with pressure. The transition of coordination was combined with a simultaneous bond elongation. Increasing the pressure even more again led to decreased bond lengths. Each step of these structural changes led to a direct, easy-to-detect and systematic response in the intensity and energy of the Kβ''-peak. Our findings are supported by theoretical calculation and backed up by previous studies performed on GeO_2 with X-ray diffraction and neutron scattering in the same pressure range. As a result, we established valence-to-core spectroscopy as a novel tool to probe coordination and bond length. In a study with geophysical background, which investigated the structural behavior of amorphous GeO_2 with pressures up to about 100 GPa[102]. Our findings provide valuable insight for the discussion about sevenfold coordinated germanium in amorphus GeO_2 at high pressure, initially observed by an XRD study[65]. This technique yields strong potential to study multi-compound samples, which are hard to investigate with XRD. In addition, a dispersive setup, like the von Hámos spectrometer, can effortlessly be applied at XFELs to study dilute samples in time-resolved studies.

Installing a multi-MHz digitizer with a high dynamic range at beamline P01 of PETRA III, we were able to record picosecond time-resolved XANES spectra and gain insight into the dynamics induced by photoexcitation of two weakly absorbing cobalt com-

plexes, a great step toward integrating XAS as standard technique at XFEL. The first sample, $[Co(III)(en)_3]^{3+}$ in aqueous solution was excited at 257, 343 and 515 nm. Based on the very close resemblance with a reference transient XANES spectrum of the iso-electronic iron complex $[Fe(II)(bpy)_3]^{2+}$, we conclude that the metastable lowest-lying excited state populated upon photoexcitation is a high-spin $^5T_2$ state. With an estimate of the excited state fraction, we reconstructed the XANES spectrum of this metastable state. Our second cobalt sample was $[Co(III)(CN)_6]^{3-}$ in aqueous solution, in which we measured the dynamics induced by 343 nm laser light. Additional single photon counting XANES measurements at 7ID-D, APS, performed with 266 nm photoexcitation showed signatures of the photoaquated $[Co(III)(CN)_5(H_2O)]^{2-}$ complex in the transient XANES spectrum. However, the strong contrast of this spoiled signal (indicated by the rise of two peaks in the pre-edge region) suggests, that the measurements carried out at P01 show the signature of the pure metastable state. This is backed up by comparing it to the iso-electronic reference $[Fe(II)(CN)_6]^{4-}$ which has been extensively studied[12]. Based on the transient XANES spectrum obtained at P01 and an estimate of the excited state fraction, we reconstructed the XANES spectrum of the metastable $^3T_{1g}$ lowest-lying excited state.

For both cobalt samples, to proceed with the investigation of the short-lived states, which happen in the first 100 ps, we would require the time resolution provided by an XFEL. To clarify the contribution of the photoaquated $[Co(III)(CN)_5(H_2O)]^{2-}$ complex and its excited state to the changes in the pre-edge, which is still an open question even for the iron case, further investigation of the photoaquated complex would be required. This could be done by probing the excited sample a few nanoseconds after photoexcitation at low repetition rate and would give valuable insights into the formation of photoaquated complex during the absence of the excited photoaquated complex.

Eidesstattliche Versicherung / Declaration on oath

Hiermit versichere ich an Eides statt, die vorliegende Dissertationsschrift selbst verfasst und keine anderen als die angegebenen Hilfsmittel und Quellen benutzt zu haben.

Sofern im Zuge der Erstellung der vorliegenden Dissertationsschrift generative Künstliche Intelligenz (gKI) basierte elektronische Hilfsmittel verwendet wurden, versichere ich, dass meine eigene Leistung im Vordergrund stand und dass eine vollständige Dokumentation aller verwendeten Hilfsmittel gemäß der Guten wissenschaftlichen Praxis vorliegt. Ich trage die Verantwortung für eventuell durch die gKI generierte fehlerhafte oder verzerrte Inhalte, fehlerhafte Referenzen, Verstöße gegen das Datenschutz- und Urheberrecht oder Plagiate.

Hamburg, den 16.01.2025 Unterschrift

Acknowledgments

I cannot thank enough everyone who accompanied me during my Ph.D. and many other research projects. First and foremost, I want to thank my supervisor Christian Bressler for his continuous support, valuable input and many scientific discussions throughout my thesis and the opportunity to work on this topic. A special thank goes to Nils Huse for co-supervising my thesis. I want to express my gratitude to Michael Thorwart, Georg Spiekermann and Michael Martins who agreed to evaluate this Ph.D. thesis and the upcoming Ph.D. defense.
I thank all the people who work or have worked at beamline P01, especially Hasan Yavas, who introduced me to the X-ray spectroscopy business. Didem Keteoglu who suffered with me during many nights at P01. Georg Spiekermann for many scientific and non-scientific discussions. Mehran Taherkhani, Frank-Uwe Dill, Martin Sundermann, Pavel Alexeev and Hans-Christian Wille. I would like to extend my thanks to the people who work or have worked at FXE, especially Christina Bömer, Alexander Britz, Tadesse Assefa, Michael Diez, Andreas Galler, Wojciech Gawelda, Sebastian Schulz, Dmitry Khakhulin and Peter Zalden.
I want to thank the people that work at beamline 7ID-D at APS and beamline ID20 at ESRF and enabled this research. Especially Christoph Sahle, who significantly helped me evolving my python skills. A special thanks to Christian Sternemann and Sophie Canton for their invaluable suggestions, support and feedback during many discussions.
I would like to thank Zhong Yin for involving me in many research projects. I appreciate all the work done by the teams of FS-EC and FS-BT, especially André Rothkirch who sacrificially takes care of all experiments at PETRA III, day and night.
I thank TU Dortmund and the BMBF (Project No. 05K13PE2) as well as DESY, the Helmholtz Association and PHGS for funding me and enabling my research during my thesis.
My deepest thanks go out to my friends, especially Sönke Häseler, Daniel Ostach who initially got me into this project and Holger Müller for accompanying me since our time at university. Again I would like to thank Georg, Christina, Didem and Zhong, who became close friends during our joint work on many projects.
Finally, I would like to express my gratitude to my parents and siblings for their support and love.

P.S. Christina Bömer and Dietrich Krebs for their past last-minute emergency support during the submission day.

Bibliography

[1] Beamline 9 DELTA TU - Dortmund. https://www.delta.tu-dortmund.de/cms/de/Forschung/Strahllinien/Beamline_9/index.html. [Online; accessed 25-February-2023].

[2] Beamline layout and parameters. https://photon-science.desy.de/facilities/petra_iii/beamlines/p01_dynamics/beamline_layout/index_eng.html. [Online; accessed 24-February-2023].

[3] Beschleuniger DELTA TU - Dortmund. https://www.delta.tu-dortmund.de/cms/de/Beschleuniger/index.html. [Online; accessed 24-February-2023].

[4] CXRO X-Ray Interactions With Matter. https://henke.lbl.gov/optical_constants/. [Online; accessed 25-February-2023].

[5] Proposed APS-U Technical Parameters. https://www.aps.anl.gov/Beamline-Selection/Technical-Information/Storage-Ring-Parameters. [Online; accessed 24-February-2023].

[6] Sector 7-ID Techniques-and-Facilities. https://www.aps.anl.gov/Sector-7/7-ID/Techniques-and-Facilities/7ID-D. [Online; accessed 14-September-2015].

[7] The Franck-Condon Principle . https://chem.libretexts.org/Courses/Knox_College/Chem_322%3A_Physical_Chemisty_II/07%3A_Molecular_Spectroscopy/7.07%3A_The_Franck-Condon_Principle. [Online; accessed 24-September-2023].

[8] XCOM: Photon Cross Sections Database. https://physics.nist.gov/PhysRefData/Xcom/html/xcom1.html. [Online; accessed 24-February-2023].

[9] I. Agapov, R. Bacher, M. Bieler, R. Bospflug, R. Brinkmann, Y.-C. Chae, H. Chao, H. Duhme, M. Ebert, H.-J. Eckoldt, H. Ehrlichmann, X. GavaldÃ , M. Hüning, U. Hurdelbrink, J. Keil, J. Klute, M. Körfer, B. Krause, G. Kube, W. Leemans, L. Lilje, F. Obier, A. Petrov, N. Plambeck, J. Prenting, G. Sahoo, H. Schlarb, M. Schlösser, F. Schmidt-Föhre, M. Schmitz, C. Schroer, T. Tempel, M. Thede, M. Tis-

cher, R. Wanzenberg, E. Weckert, T. Wilksen, K. Wittenburg, and J. Zhang. Status of the petra iv project. 2019.

[10] R. Alonso-Mori, J. F. Kern, D. Sokaras, T.-C. Weng, D. Nordlund, R. Tran, P. A. Montanez, J. T. Delor, V. K. Yachandra, J. Yano, and U. Bergmann. A multi-crystal wavelength dispersive x-ray spectrometer. *The Review of scientific instruments*, 83 7:073114, 2012.

[11] J. A. Als-Nielsen and D. F. McMorrow. Elements of modern x-ray physics. 2001.

[12] T. A. Assefa. *Tracking Chemical Reactions with Ultrafast X-ray Spectroscopic techniques*. Dissertation, Universität Hamburg, 2017.

[13] M. L. Baker, M. W. Mara, J. J. Yan, K. O. Hodgson, B. Hedman, and E. I. Solomon. K- and l-edge x-ray absorption spectroscopy (xas) and resonant inelastic x-ray scattering (rixs) determination of differential orbital covalency (doc) of transition metal sites. *Coordination chemistry reviews*, 345:182–208, 2017.

[14] M. Baldini, G. Aquilanti, H. kwang Mao, W. Yang, G. Shen, S. Pascarelli, and W. L. Mao. High-pressure exafs study of vitreous geo 2 up to 44 gpa. *Physical Review B*, 81:024201, 2010.

[15] A. Balerna and S. Mobilio. Introduction to synchrotron radiation. 2015.

[16] K. Balewski, W. Decking, W. Brefeld, R. Röhlsberger, H. Franz, and E. Weckert. Petra iii: A low emittance synchrotron radiation source (technical design report). 2004.

[17] C. J. Ballhausen and M. A. Weiner. Introduction to ligand field theory. 1962.

[18] A. Q. Baron. Introduction to high-resolution inelastic x-ray scattering. *arXiv: Materials Science*, 2015.

[19] M. Bauer. Herfd-xas and valence-to-core-xes: new tools to push the limits in research with hard x-rays? *Physical chemistry chemical physics : PCCP*, 16 27:13827–37, 2014.

[20] Beer. Bestimmung der absorption des rothen lichts in farbigen flüssigkeiten. *Annalen der Physik*, 1852.

[21] U. Berges and K. Wille. Status of the delta synchrotron light-monitoring-system. 1999.

[22] U. Bergmann and P. Glatzel. X-ray emission spectroscopy. *Photosynthesis Research*, 102:255–266, 2009.

[23] U. Bergmann, P. Glatzel, and S. P. Cramer. Bulk-sensitive xas characterization of light elements: from x-ray raman scattering to x-ray raman spectroscopy. *Microchemical Journal*, 71:221–230, 2002.

[24] L. Bertini, P. Ghigna, M. Scavini, and F. Cargnoni. Germanium k edge in geo2 polymorphs. correlation between local coordination and electronic structure of germanium. *Physical Chemistry Chemical Physics*, 5:1451–1456, 2003.

[25] J. A. Bokhoven and C. Lamberti. X-ray absorption and x-ray emission spectroscopy: Theory and applications. 2016.

[26] J. A. Bradley, K. T. Moore, G. Laan, J. P. Bradley, and R. A. Gordon. Core and shallow-core d - to f -shell excitations in rare-earth metals. *Physical Review B*, 84, 2011.

[27] C. Bressler, W. Gawelda, A. Galler, M. M. Nielsen, V. Sundström, G. Doumy, A. M. March, S. H. Southworth, L. Young, and G. Vankó. Solvation dynamics monitored by combined x-ray spectroscopies and scattering: photoinduced spin transition in aqueous [fe(bpy)3](2+). *Faraday discussions*, 171:169–78, 2014.

[28] A. Britz. *Ultrafast X-ray Spectroscopies of Transition Metal Complexes Relevant for Catalysis*. Dissertation, Universität Hamburg, 2017.

[29] A. Britz, T. A. Assefa, A. Galler, W. Gawelda, M. Diez, P. Zalden, D. Khakhulin, B. Fernandes, P. Geßler, H. S. Namin, A. Beckmann, M. Harder, H. Yavas, and C. Bressler. A multi-mhz single-shot data acquisition scheme with high dynamic range: pump-probe x-ray experiments at synchrotrons. *Journal of synchrotron radiation*, 23 Pt 6:1409–1423, 2016.

[30] M. C. Carey, S. L. Adelman, and J. K. McCusker. Insights into the excited state dynamics of fe(ii) polypyridyl complexes from variable-temperature ultrafast spectroscopy. *Chemical Science*, 10:134 – 144, 2018.

[31] C. Conti, F. Castelli, and L. S. Forster. Photophysics of hexakis(cyano)chromate(3-)

and hexakis(cyano)cobaltate(3-) in polyalcohol-water solutions at room temperature. *The Journal of Physical Chemistry*, 83:2371–2376, 1979.

[32] F. de Groot and A. Kotani. Core level spectroscopy of solids. CRC Press, 2008.

[33] F. M. F. de Groot. High-resolution x-ray emission and x-ray absorption spectroscopy. *Chemical reviews*, 101 6:1779–808, 2001.

[34] W. Demtröder. Experimentalphysik 3: Atome, moleküle und festkörper. 2005.

[35] X.-W. Du and J. S. Tse. Oxygen packing fraction and the structure of silicon and germanium oxide glasses. *The journal of physical chemistry. B*, 121 47:10726–10732, 2017.

[36] P. em. Dr. Heinz-Helmut Perkampus. Uv-vis spectroscopy and its applications. In *Springer Lab Manuals*, 1992.

[37] J. Evans. X-ray absorption spectroscopy for the chemical and materials sciences. 2018.

[38] A. Galler, W. Gawelda, M. Biednov, C. Bomer, A. Britz, S. Brockhauser, T.-K. Choi, M. Diez, P. Frankenberger, M. J. French, D. Görries, M. Hart, S. Hauf, D. Khakhulin, M. Knoll, T. Korsch, K. Kubicek, M. Kuster, P. M. Lang, F. A. Lima, F. Otte, S. A. Schulz, P. Zalden, and C. Bressler. Scientific instrument femtosecond x-ray experiments (fxe): instrumentation and baseline experimental capabilities1. *Journal of Synchrotron Radiation*, 26:1432 – 1447, 2019.

[39] E. Gallo and P. Glatzel. Valence to core x-ray emission spectroscopy. *Advanced Materials*, 26, 2014.

[40] K. Gilmore, J. Vinson, E. L. Shirley, D. Prendergast, C. D. Pemmaraju, J. J. Kas, F. D. Vila, and J. J. Rehr. Efficient implementation of core-excitation bethe-salpeter equation calculations. *Comput. Phys. Commun.*, 197:109–117, 2015.

[41] P. Glatzel and U. Bergmann. High resolution 1s core hole x-ray spectroscopy in 3d transition metal complexes-electronic and structural information. *Coordination Chemistry Reviews*, 249:65–95, 2005.

[42] P. Glatzel, F. de Groot, O. V. Manoilova, D. Grandjean, B. M. Weckhuysen, U. Bergmann, and R. Barrea. Range-extended exafs at the l edge of rare earths

using high-energy-resolution fluorescence detection : A study of la in laocl. *Physical Review B*, 72, 2005.

[43] P. Glatzel, A. Harris, P. Marion, M. Sikora, T.-C. Weng, C. Guilloud, S. Lafuerza, M. Rovezzi, B. Detlefs, and L. Ducotté. The five-analyzer point-to-point scanning crystal spectrometer at esrf id26. *Journal of synchrotron radiation*, 28 Pt 1:362–371, 2021.

[44] P. Glatzel, M. Sikora, and M. Fernández-García. Resonant x-ray spectroscopy to study k absorption pre-edges in 3d transition metal compounds. *The European Physical Journal Special Topics*, 169:207–214, 2009.

[45] H. Gretarsson, D. Ketenoglu, M. Harder, S. Mayer, F.-U. Dill, M. Spiwek, H. Schulte-schrepping, M. Tischer, H. C. Wille, B. Keimer, and H. Yavas. Irixs: a resonant inelastic x-ray scattering instrument dedicated to x-rays in the intermediate energy range. *Journal of Synchrotron Radiation*, 27:538 – 544, 2020.

[46] P. Gütlich, H. A. Goodwin, Y. Garcia, M. L. Boillot, and K. Boukheddaden. Spin crossover in transition metal compounds ii. 2004.

[47] K. Hämäläinen and S. Manninen. Resonant and non-resonant inelastic x-ray scattering. *Journal of Physics: Condensed Matter*, 13:7539–7555, 2001.

[48] A. W. Hauser, C. Enachescu, M. L. Daku, A. Vargas, and N. Amstutz. Low-temperature lifetimes of metastable high-spin states in spin-crossover and in low-spin iron(ii) compounds: The rule and exceptions to the rule. *Coordination Chemistry Reviews*, 250:1642–1652, 2006.

[49] G. S. Henderson, F. de Groot, and B. J. A. Moulton. X-ray absorption near-edge structure (xanes) spectroscopy. *Reviews in Mineralogy & Geochemistry*, 78:75–138, 2014.

[50] B. L. Henke, E. M. Gullikson, and J. C. Davis. X-ray interactions: Photoabsorption, scattering, transmission, and reflection at e = 50-30,000 ev, z = 1-92. *Atomic Data and Nuclear Data Tables*, 54:181–342, 1993.

[51] G. Herzberg and J. W. T. Spinks. Molecular spectra and molecular structure. 1992.

[52] X. Hong, L. Ehm, and T. S. Duffy. Polyhedral units and network connectivity in

geo2 glass at high pressure: An x-ray total scattering investigation. *Applied Physics Letters*, 105:081904, 2014.

[53] X. Hong, M. Newville, T. S. Duffy, S. Sutton, and M. L. Rivers. X-ray absorption spectroscopy of geo2 glass to 64 gpa. *Journal of Physics: Condensed Matter*, 26, 2013.

[54] S. Huotari, C. J. Sahle, C. Henriquet, A. Al-Zein, K. Martel, L. Simonelli, R. Verbeni, H. Gonzalez, M. C. Lagier, C. Ponchut, M. M. Sala, M. Krisch, and G. Monaco. A large-solid-angle x-ray raman scattering spectrometer at id20 of the european synchrotron radiation facility. *Journal of synchrotron radiation*, 24 Pt 2:521–530, 2017.

[55] K. je Kim. Synchrotron radiation and free-electron lasers. 2002.

[56] H. Johann. Die erzeugung lichtstarker röntgenspektren mit hilfe von konkavkristallen. *Zeitschrift für Physik*, 69:185–206, 1931.

[57] A. Kalinko, W. A. Caliebe, R. Schoch, and M. Bauer. A von hamos-type hard x-ray spectrometer at the petra iii beamline p64. *Journal of Synchrotron Radiation*, 27:31 – 36, 2020.

[58] E. Källman, M. Guo, M. G. Delcey, D. A. Meyer, K. J. Gaffney, R. Lindh, and M. Lundberg. Simulations of valence excited states in coordination complexes reached through hard x-ray scattering. *Physical chemistry chemical physics : PCCP*, 2020.

[59] G. B. Kauffman. Inorganic chemistry, 2nd ed. by gary l. miessler and donald a. tarr. volume 4, page 200, 1999.

[60] D. Ketenoglu, M. Harder, K. Klementiev, M. H. Upton, M. Taherkhani, M. Spiwek, F.-U. Dill, H. C. Wille, and H. Yavas. Resonant inelastic x-ray scattering spectrometer with 25 mev resolution at the cu k-edge. *Journal of Synchrotron Radiation*, 22:961 – 967, 2014.

[61] D. Ketenoglu, G. Spiekermann, M. Harder, E. Oz, C. Koz, M. C. Yagci, E. Yilmaz, Z. Yin, C. J. Sahle, B. Detlefs, and H. Yavas. X-ray raman spectroscopy of lithium-ion battery electrolyte solutions in a flow cell. *Journal of synchrotron radiation*, 25 Pt 2:537–542, 2018.

[62] K. Klementiev. Gallery of plots and scripts 2. X-ray optics - xrt 1.5.0 documentation. `https://xrt.readthedocs.io/gallery2.html`, 2014.

[63] K. Klementiev and R. V. Chernikov. Powerful scriptable ray tracing package xrt. In *Optics & Photonics - Optical Engineering + Applications*, 2014.

[64] D. D. Koningsberger and R. Prins. X-ray absorption : principles, applications, techniques of exafs, sexafs and xanes. *Chemia Analityczna*, 92, 1988.

[65] Y. Kono, C. Kenney-Benson, D. Ikuta, Y. Shibazaki, Y. Wang, and G. Shen. Ultrahigh-pressure polyamorphism in geo2 glass with coordination number >6. *Proceedings of the National Academy of Sciences*, 113:3436 – 3441, 2016.

[66] A. Kotani. Theory of resonant x-ray emission spectroscopy. *Journal of synchrotron radiation*, 8 Pt 2:110–4, 2001.

[67] A. Kotani and S. Shin. Resonant inelastic x-ray scattering spectra for electrons in solids. *Reviews of Modern Physics*, 73:203–246, 2001.

[68] H. A. Kramers and W. Heisenberg. Über die streuung von strahlung durch atome. *Zeitschrift für Physik*, 31:681–708, 1925.

[69] K. Kunnus, W. Zhang, M. G. Delcey, R. V. Pinjari, P. S. Miedema, S. Schreck, W. Quevedo, H. Schröder, A. Föhlisch, K. J. Gaffney, M. Lundberg, M. Odelius, and P. Wernet. Viewing the valence electronic structure of ferric and ferrous hexacyanide in solution from the fe and cyanide perspectives. *The journal of physical chemistry. B*, 120 29:7182–94, 2016.

[70] R. Kurian, K. Kunnus, P. Wernet, S. M. Butorin, P. Glatzel, and F. M. F. de Groot. Intrinsic deviations in fluorescence yield detected x-ray absorption spectroscopy: the case of the transition metal l2,3 edges. *Journal of Physics: Condensed Matter*, 24 45:2201, 2012.

[71] H. kwang Mao, J. A. Xu, and P. M. Bell. Calibration of the ruby pressure gauge to 800 kbar under quasi-hydrostatic conditions. *Journal of Geophysical Research*, 91:4673–4676, 1986.

[72] H. G. Manyar, R. Morgan, K. Morgan, B. Yang, P. Hu, J. Szlachetko, J. Sá, and C. Hardacre. High energy resolution fluorescence detection xanes - an in situ method to study the interaction of adsorbed molecules with metal catalysts in the liquid phase. *Catalysis Science & Technology*, 3:1497–1500, 2013.

[73] A. M. March, T. A. Assefa, C. Boemer, C. Bressler, A. Britz, M. Diez, G. Doumy,

A. Galler, M. Harder, D. Khakhulin, Z. Németh, M. Pápai, S. A. Schulz, S. H. Southworth, H. Yavas, L. Young, W. Gawelda, and G. Vankó. Probing transient valence orbital changes with picosecond valence-to-core x-ray emission spectroscopy. *The Journal of Physical Chemistry. C, Nanomaterials and Interfaces*, 121:2620 – 2626, 2017.

[74] A. M. March, T. A. Assefa, C. Bressler, G. Doumy, A. Galler, W. Gawelda, E. P. Kanter, Z. Németh, M. Pápai, S. H. Southworth, L. Young, and G. Vankó. Feasibility of valence-to-core x-ray emission spectroscopy for tracking transient species. *The Journal of Physical Chemistry. C, Nanomaterials and Interfaces*, 119:14571 – 14578, 2015.

[75] G. Margaritondo. Synchrotron light in a nutshell. *Surface Review and Letters*, 7:379–387, 2000.

[76] J. K. McCusker, K. N. Walda, D. Magde, and D. N. Hendrickson. Picosecond excited-state dynamics in octahedral cobalt(iii) complexes : intersystem crossing versus internal conversion. *Inorganic Chemistry*, 32:394–399, 1993.

[77] Q. Mei, S. Sinogeikin, G. Shen, S. A. Amin, C. J. Benmore, and K. Ding. High-pressure x-ray diffraction measurements on vitreous geo 2 under hydrostatic conditions. *Physical Review B*, 81:174113, 2010.

[78] S. J. Milder, H. B. Gray, and V. M. Miskowski. Photochemistry of hexacyanocobaltate(iii) in haloalkanes. *Journal of the American Chemical Society*, 106:3764–3767, 1984.

[79] Y. Mizuno and Y. Ohmura. Theory of x-ray raman scattering. *Journal of the Physical Society of Japan*, 22:445–449, 1967.

[80] L. Moggi, F. Bolletta, V. Balzani, and F. Scandola. Photochemistry of coordination compounds-xv: Cyanide complexes. *Journal of Inorganic and Nuclear Chemistry*, 28:2589–2597, 1966.

[81] K. L. Mulfort and L. M. Utschig. Modular homogeneous chromophore-catalyst assemblies. *Accounts of chemical research*, 49 5:835–43, 2016.

[82] M. Nagasaka, H. Yuzawa, T. Horigome, and N. Kosugi. Reliable absorbance measurement of liquid samples in soft x-ray absorption spectroscopy in transmission mode. *Journal of Electron Spectroscopy and Related Phenomena*, 224:93–99, 2018.

[83] H. Nagasawa, S. Mourikis, and W. Schülke. X-ray raman spectrum of li, be and

graphite in a high-resolution inelastic synchrotron x-ray scattering experiment. *Journal of the Physical Society of Japan*, 58(2):710–717, 1989.

[84] M. Nishazawa and P. C. Ford. Correction. long-wavelength excitation of hexacyanocobaltate(iii), co(cn), in aqueous solution. questions regarding intersystem-crossing efficiencies. *Inorganic Chemistry*, 20:1944–1944, 1981.

[85] H. Onuki and P. Elleaume. Undulators, wigglers and their applications. 2002.

[86] J. E. Penner-Hahn. 2 . 13 x-ray absorption spectroscopy. 2003.

[87] S. Petitgirard, G. Spiekermann, C. Weis, C. J. Sahle, C. Sternemann, and M. Wilke. Miniature diamond anvils for x-ray raman scattering spectroscopy experiments at high pressure. *Journal of synchrotron radiation*, 24 Pt 1:276–282, 2017.

[88] D. Popmintchev, B. R. Galloway, M.-C. Chen, F. J. Dollar, C. A. Mancuso, A. Hankla, L. Miaja-Avila, G. C. O'Neil, J. M. Shaw, G. Fan, S. Alisauskas, G. Andriukaitis, T. Balciunas, O. . Mücke, A. Pugzlys, A. Baltuska, H. C. Kapteyn, T. Popmintchev, and M. M. Murnane. Near- and extended-edge x-ray-absorption fine-structure spectroscopy using ultrafast coherent high-order harmonic supercontinua. *Physical review letters*, 120 9:093002, 2018.

[89] N. Queyriaux, R. T. Jane, J. Massin, V. Artero, and M. Chavarot-Kerlidou. Recent developments in hydrogen evolving molecular cobalt(ii)-polypyridyl catalysts. *Coordination chemistry reviews*, 304-305:3 – 19, 2015.

[90] W. C. Röntgen. Ueber eine neue art von strahlen. *Annalen der Physik*, 1895 volume=300, pages=1-11.

[91] J. P. Rueff and A. Shukla. Inelastic x-ray scattering by electronic excitations under high pressure. *Reviews of Modern Physics*, 82:847–896, 2010.

[92] C. J. Sahle, F. Gerbon, C. Henriquet, R. Verbeni, B. Detlefs, A. Longo, A. Mirone, M. C. Lagier, F. Otte, G. Spiekermann, and S. Petitgirard. A compact von hámos spectrometer for parallel x-ray raman scattering and x-ray emission spectroscopy at id20 of the european synchrotron radiation facility. *Journal of Synchrotron Radiation*, 30:251 – 257, 2023.

[93] C. J. Sahle, A. Mirone, J. Niskanen, J. Inkinen, M. Krisch, and S. Huotari. Plan-

ning, performing and analyzing x-ray raman scattering experiments. *Journal of Synchrotron Radiation*, 22:400 – 409, 2015.

[94] P. S. Salmon, J. W. E. Drewitt, D. A. J. Whittaker, A. Zeidler, K. Wezka, C. L. Bull, M. G. Tucker, M. C. Wilding, M. Guthrie, and D. Marrocchelli. Density-driven structural transformations in network forming glasses: a high-pressure neutron diffraction study of geo2 glass up to 17.5 gpa. *Journal of Physics: Condensed Matter*, 24, 2012.

[95] E. W. Schlag, S. Schneider, and S. F. Fischer. Lifetimes in excited states. *Annual Review of Physical Chemistry*, 22:465–526, 1971.

[96] Schülke, Nagasawa, Mourikis, and Kaprolat. Dynamic structure of electrons in be metal by inelastic x-ray scattering spectroscopy. *Physical review. B, Condensed matter*, 40 18:12215–12228, 1989.

[97] W. Schülke. Electron dynamics by inelastic x-ray scattering. Oxford Univ. Press, 2007.

[98] S. Serkez, G. Geloni, S. Tomin, G. Feng, E. V. Gryzlova, A. N. Grum-Grzhimailo, and M. Meyer. Overview of options for generating high-brightness attosecond x-ray pulses at free-electron lasers and applications at the european xfel. *Journal of Optics*, 20, 2018.

[99] T. Shaftan. Synchrotron Radiation. `https://www.bnl.gov/nsls2/userguide/lectures/lecture-2-shaftan.pdf`. [Online; accessed 24-February-2023].

[100] G. Shen and H. kwang Mao. High-pressure studies with x-rays using diamond anvil cells. *Reports on Progress in Physics*, 80, 2017.

[101] D. Sokaras, T.-C. Weng, D. Nordlund, R. Alonso-Mori, P. Velikov, D. F. Wenger, A. Garachtchenko, M. George, V. Borzenets, B. Johnson, T. Rabedeau, and U. Bergmann. A seven-crystal johann-type hard x-ray spectrometer at the stanford synchrotron radiation lightsource. *The Review of scientific instruments*, 84 5:053102, 2013.

[102] G. Spiekermann, M. Harder, K. Gilmore, P. Zalden, C. J. Sahle, S. Petitgirard, M. Wilke, N. Biedermann, C. Weis, W. Morgenroth, J. S. Tse, E. Kulik, N. Nishiyama, H. Yavas, and C. Sternemann. Persistent octahedral coordination

in amorphous geo2 up to 100 gpa by kβ" x-ray emission spectroscopy. *Physical Review X*, 2019.

[103] G. Spiekermann, C. J. Sahle, J. Niskanen, K. Gilmore, S. Petitgirard, C. Sternemann, J. S. Tse, and M. Murakami. Sensitivity of the kβ" x-ray emission line to coordination changes in geo2 and tio2. *The Journal of Physical Chemistry Letters*, 14:1848 – 1853, 2023.

[104] C. Sternemann, M. Volmer, J. A. Soininen, H. Nagasawa, M. Paulus, H. Enkisch, G. Schmidt, M. Tolan, and W. Schülke. Momentum-transfer dependence of x-ray raman scattering at the be k-edge. *Physical Review B*, 68:035111, 2003.

[105] H. O. Sternemann, C. Sternemann, G. T. Seidler, T. T. Fister, A. Sakko, and M. Tolan. An extraction algorithm for core-level excitations in non-resonant inelastic x-ray scattering spectra. *Journal of synchrotron radiation*, 15 Pt 2:162–9, 2008.

[106] M. Sundermann. *f-electron charge densities probed using core level non-resonant inelastic x-ray scattering*. Dissertation, TU Dresden year=2019.

[107] B. Valeur and M. N. Berberan-Santos. Molecular fluorescence: Principles and applications. 2001.

[108] L. von Hámos. Röntgenspektroskopie und abbildung mittels gekrümmter kristallreflektoren. i. geometrisch-optische betrachtungen. *Annalen der Physik*, 409:716–724, 1933.

[109] L. von Hámos. Röntgenspektroskopie und abbildung mittels gekrümmter kristallreflektoren ii. beschreibung eines fokussierenden spektrographen mit punktgetreuer spaltabbildung. *Annalen der Physik*, 411:252–260, 1934.

[110] C. Weis, G. Spiekermann, C. Sternemann, M. Harder, G. Vankó, V. Cerantola, C. J. Sahle, Y. Forov, R. Sakrowski, I. Kupenko, S. Petitgirard, H. Yavas, C. Bressler, W. Gawelda, M. Tolan, and M. Wilke. Combining x-ray kβ1,3, valence-to-core, and x-ray raman spectroscopy for studying earth materials at high pressure and temperature: the case of siderite. *Journal of Analytical Atomic Spectrometry*, 2019.

[111] H.-C. Wille, H. Franz, R. Röhlsberger, W. A. Caliebe, and F.-U. Dill. Nuclear resonant scattering at petra iii : Brillant opportunities for nano - and extreme condition science. *Journal of Physics: Conference Series*, 217:012008, 2010.

[112] P. R. Willmott. An introduction to synchrotron radiation. 2011.

[113] J. S. Wood. Ligand field theory. *Nature*, 226:1067–1068, 1970.

[114] W. Zhang, R. Alonso-Mori, U. Bergmann, C. Bressler, M. Chollet, A. Galler, W. Gawelda, R. G. Hadt, R. W. Hartsock, T. Kroll, K. S. Kjær, K. Kubicek, H. T. Lemke, H. W. Liang, D. A. Meyer, M. M. Nielsen, C. M. Purser, J. S. Robinson, E. I. Solomon, Z. Sun, D. Sokaras, T. B. van Driel, G. Vankó, T. chien Weng, D. Zhu, and K. J. Gaffney. Tracking excited-state charge and spin dynamics in iron coordination complexes. *Nature*, 509:345–348, 2014.

[115] P. Zimmermann, S. Peredkov, P. M. Abdala, S. DeBeer, M. Tromp, C. R. Müller, and J. A. Bokhoven. Modern x-ray spectroscopy: Xas and xes in the laboratory. *Coordination Chemistry Reviews*, 423:213466, 2020.